The Pennsylvania State University

The Graduate School

Department of Aerospace Engineering

AERODYNAMIC TIP DESENSITIZATION IN AXIAL FLOW TURBINES

A Thesis in

Aerospace Engineering

by

Debashis Dey

Submitted in Partial Fulfillment
of the Requirements
for the Degree of

Doctor of Philosophy

December 2001

We approve the thesis of Debashis Dey.

Date of Signature

Cengiz Camci Professor of Aerospace Engineering Thesis Adviser Chair of Committee	
Dennis K. McLaughlin Professor of Aerospace Engineering Chairman, Department of Aerospace Engineering	
Savash Yavuzkurt Professor of Mechanical Engineering	
Timothy F. Miller Research Scientist	

Abstract

The leakage flow near the tip of unshrouded rotor blades in axial turbines imposes significant thermal loads on the blade. It is also responsible for up to a third of aerodynamic losses in a turbine stage. The leakage flow, mainly induced by the pressure differential across the rotor tip section, usually rolls into a stream-wise vortical structure near the suction side of the blade tip. The current study uses several concepts to reduce the severity of losses introduced by the leakage vortex. Three tip desensitization techniques, both active and passive, are examined. Coolant flow from a tip trench is used to counter the momentum of the leakage jet. Next, a very short winglet obtained by slightly extending the tip platform in the tangential direction is investigated. Lastly, variations of the widely used concept of squealer tip are studied. The current investigation is performed in the Axial Flow Turbine Research Facility (AFTRF) of the Pennsylvania State University. Rotating frame five hole probe measurements as well as stationary frame phase averaged total pressure measurements downstream of a single stage turbine facility are taken. A method of studying the heat transfer coefficient on the blade tip is also developed. The study enables one to draw conclusions about the nature of the flowfield in the rotor tip region. It also shows that significant efficiency gains might be possible by using some of these techniques.

Table of Contents

List of Tables

List of Figures

Chapter 1

Introduction

1.1 Nature of the Problem

Gas turbines are designed to convert flow total enthalpy to rotational work. The efficiency of this conversion depends on the flow irreversibilities that accompany the conversion process. It has been observed that these ireversibilities remain localized, giving rise to hot spots of high entropy generation in the flow. The most prominent such hot spot is a flow structure, known as the leakage vortex, that occurs universally near the tips of unshrouded rotor blades.

The tips of axial turbine blades rotate in close proximity to stationary peripheral casing. Clearance gap between the rotating blades and the stationary casing are typically less than one percent of the blade height for larger engines, and up to 1.5% for smaller engines with low aspect ratio blading. The pressure difference between the pressure and the suction sides of the blade drives flow through through the clearance gap. The mainstream flow is turned into the gap near the pressure side of the blade. When the flow emerges near the suction side of the gap, it is normally visualized as rolling into a vortex as it meets the oncoming passage flow. The leakage flow has significant effect both on the stage aerodynamic performance and the structural durability of the blade. The surface area of the blade tip, which stays in contact with hot gas, is an area of high convective heat transfer and thermal loading on the blade, which must be removed by internal cooling flow of the blade. The cooling flow, which is supplied by the HP stage of the engine compressor, imposes a thermodynamic penalty on the engine performance, and thus

blade tip heat transfer tends to degrade engine performance further. The high temperature also causes oxidation of the blade tip, especially in ground based engines which are operated for long periods without shutdown. Additionally, the tip often rubs against the casing in airplane power plants, where the clearance gap varies during the operational cycle. So, leakage flow poses an aerothermal problem, in terms of pressure losses and reduction of stage efficiency on one hand, and structural degradation of blade tip on the other.

The term desensitization is used to describe efforts to reduce the potential damage of leakage flows. Tip treatments tend to be manufacturer specific, and not many get discussed in open literature. A few designs implement shrouded blade rows, exchanging leakage problem with others. The present work proposes three tip desensitization schemes, and discusses the aerothermal fields associated with them.

The tip leakage problem occurs in the broader context of passage secondary flow. The important features in the turbomachinery flowfield needs to known in order to address the tip leakage problem.

1.2 Passage Secondary Flow

1.2.1 Secondary Flow Mechanism

Secondary flow is a phenomena related to flow turning, and it occurs in a variety of engineering applications including turning guide vanes, curved inlet passages, compressor and turbine rotor and nozzle passages. When fluid is turned inside a curved passage, it maintains a two dimensional velocity field far from the two endwalls. Flow near the endwalls, on the other hand, shows clear three dimensionality. The boundary layer near the entry of the passage

contains gradients of velocity. When this gradient is turned in a curved passage, transverse velocities across the passage are produced. The two dimensional flow away from the endwalls is termed primary flow while the three dimensional flow near the end-walls is termed secondary flow. Transverse velocities induced by secondary flow could be significant, especially when the degree of turning is large.

Secondary flow is produced by a mechanism illustrated in Figure 1.1. The mainstream or the primary flow sets up a pressure gradient across the blade passage, from suction surface to the pressure surface. The value of this gradient depends on the mean value of the primary velocity.

$$\frac{\partial p}{\partial R} = \frac{\rho V^2}{R}$$

Here R is the radius of curvature of the primary flow streamline, as shown in the figure. The slower moving fluid in the boundary layer is subjected to the same pressure gradient as the primary flow. If V is the mean velocity of the primary flow and v is the mean velocity in the boundary layer, then $v < V$ and

$$\frac{\partial p}{\partial R} = \frac{\rho V^2}{R} = \frac{\rho v^2}{r}$$

Consequently, slower moving fluid has a smaller radius of curvature. So the flow in the end-wall is directed from the pressure surface to the suction surface. To preserve continuity, there is back flow further away from the end-wall, from the suction surface towards the pressure surface, leading to vortical flow at the passage exit.

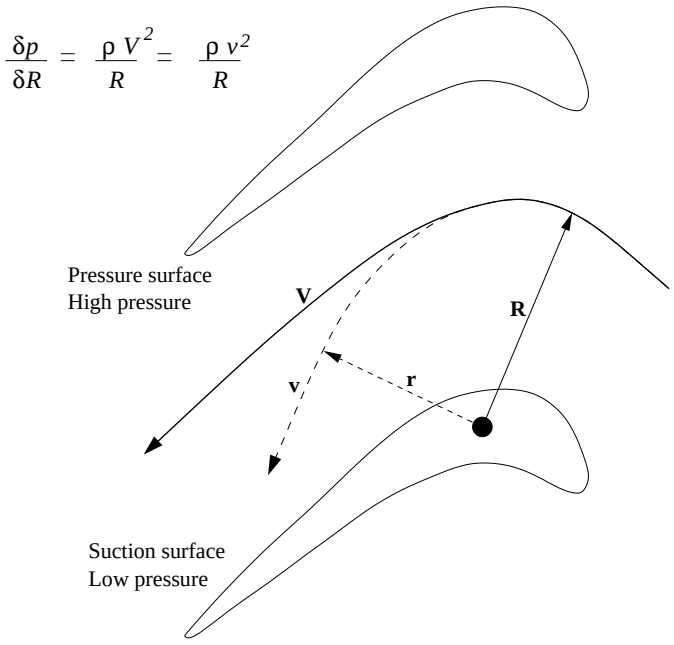

Fig. 1.1. Turning of endwall boundary layer

It follows that the magnitude of streamwise vorticity depends both on the magnitude of flow deflection in the cascade, and on the velocity gradient at the endwalls near the inlet. Hence, secondary flows are much stronger in turbine passages compared to compressor rows, where the turning is much less. On the other hand, rotor or nozzle inlet boundary layers in a turbine tend to be thinner compared to those in a compressor, leading to weaker secondary flows in a turbine.

Secondary flows are important in turbomachinery mainly for two reasons. Firstly, secondary flow causes pressure loss in a stage. Secondly, it makes the stage exit flow non uniform, which could cause increased pressure losses in a downstream row. Secondary flow in turbomachinery is complicated by the presence of other flow structures, which are described in the following sections.

1.2.2 Flow Near Inner Endwall

The endwall boundary layer experiences a strong adverse pressure gradient as it approaches the junction of the blade leading edge and the endwall. The adverse pressure gradient leads to boundary layer separation just ahead of the blade leading edge, and the flow forms a horseshoe vortex which wraps around the blade leading edge and extends to both sides of the blade. Once the flow enters the passage, it sees a pressure gradient from the pressure to the suction side, which drives the low momentum boundary layer near the inner endwall towards the suction side. The low momentum fluid wraps up into a vortex near the suction side corner. This is commonly referred to as a passage vortex, which dominates secondary flow in the latter half of the blade passage. Sometimes the passage vortex and the suction side leg of the horseshoe vortex merges together to form a single vortex system. High levels of turbulence have been measured in the core of the passage vortex ([12], [36]). High values of turbulence intensity at the suction

surface corner has also been observed. Measurement of turbulence intensities inside the passage is important from a computational perspective, since accurate turbulence models need to be built to successfully predict the flow field.

The boundary layer on the passage endwall is turbulent. The turbulent endwall boundary layer is swept up by the secondary flow mechanism to form a loss core of the passage vortex. The new boundary layer that forms is usually laminar ([26], [13]).

1.2.3 Flow Near Outer Endwall

Flow near the outer endwall is in general more complicated than the flow near the inner endwall. A passage vortex forms by a mechanism similar to that near the inner endwall. However, the entire outer endwall region is dominated by the presence of the leakage vortex. The pressure differences between the suction and pressure sides could be high enough to choke the flow across the tip gap. In general, the flow that exits on the suction side has a high velocity and an oblique angle relative to the passage flow. The resulting interaction with the passage flow causes the leakage flow to roll up into a vortical structure called the leakage vortex.

The majority of information available about the outer endwall flow comes from studies performed in linear cascades. It would be important to remember that cascade endwall flows are significantly different from flows in rotating rigs, especially near the outer endwall. The major flow characteristics of leakage flow in cascades have been comprehensively described in literature ([33], [11], [18]). Figure 1.3 shows a steady snapshot of the local flow near the tip gap observed in a linear cascade. The figure represents a slice through the blade almost normal to the camber line, as shown in Figure 1.2. It must be remembered that leakage flow in inherently three dimensional, and the two dimensional snapshot presented in 1.3 and similar schematics

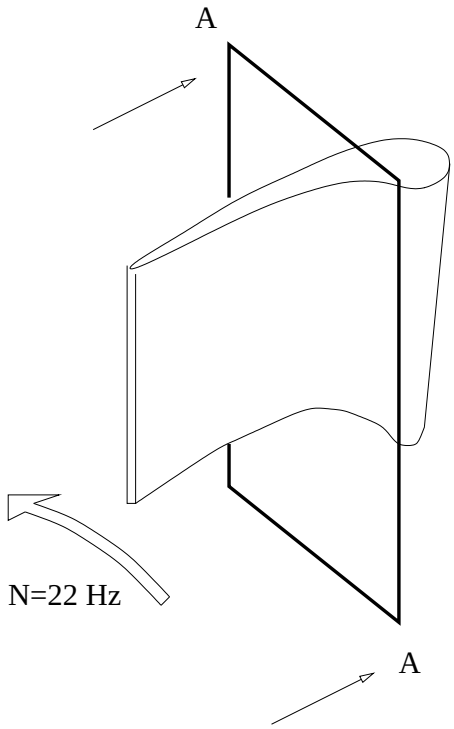

Fig. 1.2. Blade slicing plane location

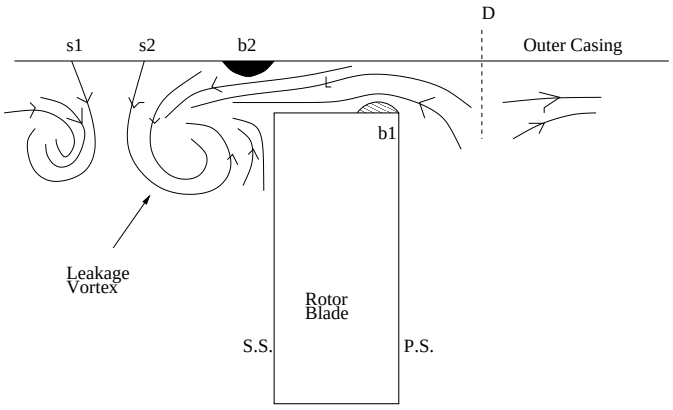

Fig. 1.3. Schematic of leakage flowfield in a linear cascade

in later sections is a part of a larger three dimensional mechanism. Although incomplete, two dimensional schematics like Figure 1.3 help highlight some important aspects of the flow field that are lost in the complexity of the full three dimensional picture. A dividing streamline is established in cascade flows, as shown by the dotted line D in Figure 1.3. This line divides the flow from the pressure side that leaked across the gap and the flow that is accelerated towards the suction side of the passage. The latter flow corresponds to the cross passage flow, similar to the cross passage flow which produced the passage vortex near the inner endwall. The passage vortex locates itself near the suction surface in case of inner endwall flow, but here in the outer endwall, it is blocked by the leakage flow, with which it interacts intensely. The separation bubble $b1$ usually forms on tips with sharp corners. Often there is a second recirculation zone $b2$ near the outer casing, formed as the leakage flow progresses towards the suction side. A leakage jet core could be observed between the outer casing and the blade tip in this stationary cascade arrangement. The separation bubbles located at $b1$ and $b2$ modifies the leakage jet orientation between the outer casing and the tip surface. This scenario is typical of blades with maximum thickness of $4t$ or more ([8]) which is the case with the present study. The bubble $b1$ never re-attaches for thinner blades ([15]). Either way, the mean kinetic energy trapped in the leakage vortex dissipates as loss.

The scenario is more complicated in an actual turbine rotor when the shearing effect of the outer casing and Coriolis forces due to the relative motion contribute to flow physics. Figure 1.4 shows possible flow processes taking place in the tip gap region, as observed in a rotating frame. The no slip condition on the rotor tip and the constant velocity relative motion of the outer casing in a direction opposite to the relative leakage flow direction creates a complex tip gap viscous flow picture. The outer casing velocity U_{casing} shears the outer edge of the

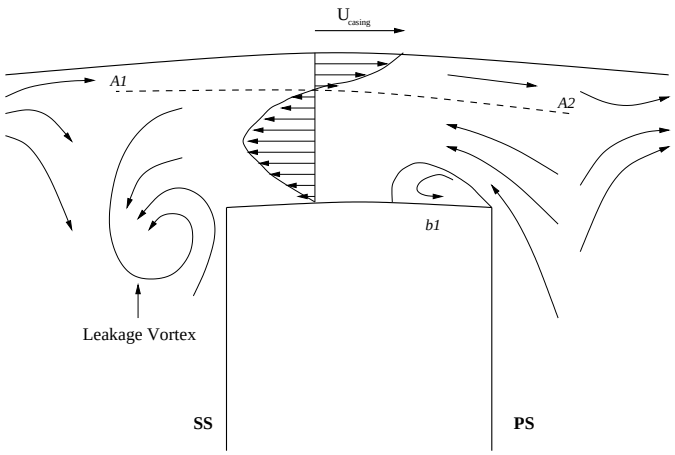

Fig. 1.4. Schematic of leakage flowfield in a turbine rotor

tip leakage jet in the gap. It follows that there must be a stagnation line $A1 - A2$ on which the velocity is zero. The gap velocity profile presented in Figure 1.4 shows a typical jet flow between the blade tip and the inflection point of the profile located near the outer casing. The relative flow with respect to the blade tip is reversed near the outer casing, above the inflection point. There is a re-circulatory flow zone at $b1$ but probably none on the outer casing surface as suggested by many stationary cascade based tip flow models. The existence of a separation bubble $b1$ near the pressure side corner may increase the overall discharge coefficient of the tip leakage flow system because of a rounded inlet geometry it creates. Higher discharge coefficients in tip gap flows result in elevated levels of aerodynamic losses for the stage. The presence of the outer casing is communicated to the leakage fluid via viscous and turbulent diffusion processes. Very near the outer casing, in the region where the mean velocity changes its direction, there is high production of turbulent kinetic energy. It would be interesting to note that the casing motion

may help in reducing the tip leakage mass flow rate and momentum by shearing it in its opposite direction. Because an outer casing relative motion does not exist in a stationary linear cascade, a linear cascade equivalent of a rotating tip clearance flow is supposed to have a stronger leakage flow. Measurements were taken inside the tip gap ([43]) in a cascade with a moving wall. It was observed that a large gap would lead to pressure driven flow with an inviscid jet while the flow would be highly sheared for smaller gap sizes.

The region of back flow induced by the moving outer endwall could be much smaller than what is shown in Figure 1.4. The leakage flow has considerable momentum near highly loaded rotor blade tips. The high momentum is likely to restrict the back flow to a very small region near the outer endwall, especially if the rotational speed of the machine (that is, the velocity of the wall) is relatively low.

1.2.4 Radial Effects in Passage Flows

The volume through which mass flows in an turbomachine is annular in geometry, and so a few peculiarities are presented by flow inside a rotational test facility which may not be observed in a planer cascade experiment. These flow features could have substantial effects on the leakage flow field.

A span-wise variation in loading could cause secondary flows even in the absence of inlet vorticity. If the exit flow is constant with radius, there would be stream-wise vorticity present in the flow. This is the reason why “free-vortex blades” are designed, in which the exit angle α is varied so that

$$\frac{d}{dr} r \tan \alpha = const$$

A much more important effect is that of the radial pressure gradient. Pressure in the hub is necessarily lower than that in the casing. This means that low energy fluid tends to migrate towards the hub. This migration takes place in the boundary layer on the blade surface, especially near the suction surface trailing edge where the boundary layer is the thickest. Migration might also occur in the blade wakes. This changes the loss distribution characteristic considerably, and greater losses occur near the hub and lesser losses occur near the casing. This is indeed seen in annular cascade measurements ([32]).

The boundary layer on the blade walls also experience a radially outward centrifugal force in a rotating blade, which is usually greater than the inward force due to the radial pressure gradient. Thus one might expect a flow of low energy fluid from the hub to the casing, and the losses near the casing is enhanced. This effect might well be masked by the leakage flowfield.

1.2.5 Vortex Interactions

Several investigators have studied the interactions between the leakage vortex and the secondary flow ([14], [39], [7]). There are many open questions on this issue, and a few conflicting observations. The interaction between the main vortical structures in the passage could be summarized as follows.

1. The passage and the leakage vortices counter-rotate, and interact intensely. The observation that the passage vortex moves towards the suction surface and below the tip vortex ([40]) is confirmed in the present tests.

2. The strength of the passage vortex is enhanced with rotation. This reduced the driving pressure difference and throttled the tip leakage flow ([27] and ([44]). However, the opposite effect was also observed ([9]) in a low Re setting, relative motion between the blade and the casing reduced leakage flow.

3. Very large tip vortices, occupying the entire passage width, have been observed, alongside a relatively small passage vortex ([7]). These tests were done with a very wide (5%) tip clearance. Most other observers have found the leakage vortex to be concentrated.

4. A leakage jet has been observed, instead of a leakage vortex ([2]). The same work did not find any passage vortex. The result was confirmed in a subsequent test in a one and half stage rotating rig ([28]).

5. The hub and tip passage vortices were not present at the same time ([42],[41]). These tests were done in a one and a half stage turbine. The outer passage vortex was weak at 0.5% clearance and disappeared at 1.9% clearance.

It could be seen from the list above that the leakage flow is not yet well understood. The main flow features have been documented, but the effects of various geometric and flow parameters on these features are largely unknown.

1.3 Effects of Secondary Flow on Loss Generation

1.3.1 Vortices and Loss Generation

As discussed in the first few sections, the main vortical structures found in a blade passage are the horseshoe vortex, the passage vortex and the leakage vortex. The first two normally

combine into one single structure by the end of the blade passage, and hence, behind a blade row, one finds an enlarged passage vortex and a leakage vortex. Each one of these is a source of pressure loss. The losses in turn affect the development of these vortices, as vorticity could be shown to depend on the total pressure gradient.

1.3.2 Loss Mechanism

Loss mechanisms in turbomachinery passages are rarely independent of each other. However, the terms “leakage loss”, “endwall loss” and “profile loss” continues to be used in literature. Profile loss corresponds to the classical airfoil wake losses. This arises mainly from the boundary layer on the blade surfaces. Losses from the boundary layers on the endwall are also included in this category, and so are the losses from the blade wake. Endwall loss is also known as secondary loss, and is related to the passage and the horseshoe vortices. Leakage losses are related to the leakage vortex that appears in an unshrouded rotors. As noted earlier, the interaction between leakage and secondary losses are strong, and it is not easy to distinguish between the two. The relative sizes of these losses depend on the design of the turbine, but they could be of equal magnitude, and then each one of them would amount to a third of the stage loss.

There are several ways to quantify losses. The loss coefficient, in its simplest form, could be defined in terms of pressures, which is easy to measure in a cascade setting (refer to Figure 1.5).

$$Y = \frac{p_{01} - p_{02}}{p_{02} - p_2}$$

Another measure of loss, in terms of enthalpy is

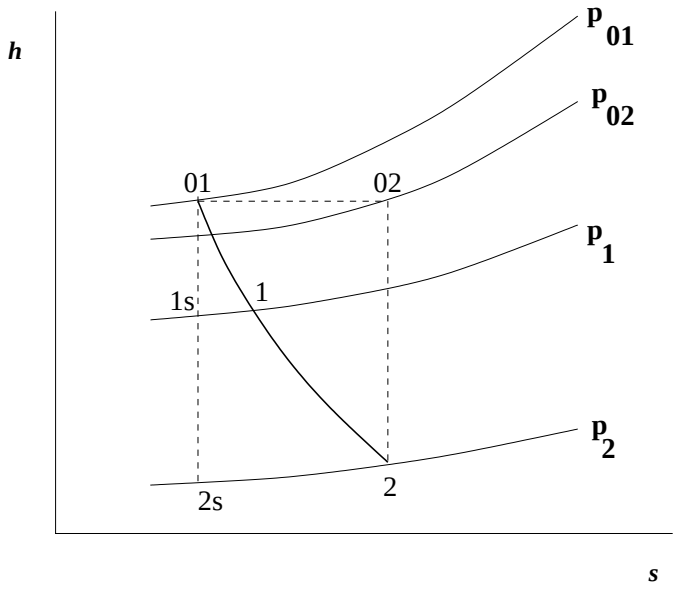

Fig. 1.5. Entropy-enthalpy diagram for a turbine cascade

$$\zeta = \frac{h_2 - h_{2s}}{h_{02} - h_2}$$

Here 1 and 2 are stations immediately upstream and downstream of a blade row. Denton ([8]) refers to these two as pressure loss coefficient and energy loss coefficient respectively.

None of these measures are applicable to a rotating machine since h_2 could change with radius, without having any loss incurred. The fundamental idea about losses in a rotating machine is the deviation from isentropic flow. Hence loss must be defined in terms of actual work to isentropic work. So, fundamentally, losses are related to entropy creation in a stage. However, entropy is an inconvenient quantity as it cannot be measured directly. For a perfect gas, change of entropy could be calculated from

$$S_2 - S_1 = C_p \log \frac{T_{02}}{T_{01}} - R \log \frac{p_{02}}{p_{01}} \tag{1.1}$$

For adiabatic flow through a stationary blade row, the total temperature is constant and the above reduces to

$$S_2 - S_1 = -R \log \frac{p_{02}}{p_{01}}$$

or,

$$S_2 - S_1 = -R \log \frac{p_{02}}{p_{01}} = -R \log(1 - \frac{\Delta p_0}{p_{01}}) = -R \frac{\Delta p_0}{p_{01}}$$

where $\Delta p_0 = p_{02} - p_{01}$ and p_{02}/p_{01} is small. This seems to suggest that $\Delta p_0/p_{01}$ or alternately p_{02}/p_{01} is a good measure of loss.

The discussion above pertains to flow in turbine cascades, where there is no work transfer from the fluid to the blades. Work done on the blade reduces the total temperature downstream of the stage in a rotating machine. So, the values of both the total temperature and the total pressure are required in order to evaluate entropy generation. This usually proves to be a difficult task, since the time response of temperature sensors is usually much smaller than the response of pressure sensors. So high frequency wake passing phenomena is difficult to resolve in sufficient detail using a temperature sensor. Alternatively, temperature could be measured in the relative frame. A temperature field could be mapped downstream of the rotor by a sensor moving with the rotor. This arrangement avoids the low time response problem typical of temperature sensors.

1.3.3 Entropy Creation Mechanisms

Entropy could be created from the following mechanisms.

1. Viscous effects or friction in boundary layer or in the free shear layer. Leakage flow is an example of a free shear layer.

2. Heat transfer across finite temperature differences. Heat transfer from mainstream to coolant flow is an example.

3. Very rapid expansions or explosions and shock waves.

The energy balance equation could be written in terms of entropy production in the following manner.

$$\rho T \frac{Ds}{Dt} = \Phi + \nabla.(\kappa \nabla T) + \frac{\partial Q}{\partial t} \tag{1.2}$$

or,

$$\frac{Ds}{Dt} = \frac{\Phi}{\rho T} + \frac{1}{\rho T}\nabla.(\kappa \nabla T) + \frac{1}{\rho T}\frac{\partial Q}{\partial t} \tag{1.3}$$

Radiative heat flux is ignored. Here Φ is the mechanical dissipation function, which depends on fluid viscosity μ and all nine velocity gradients; Q is the internal heat generation of the fluid element and κ is the thermal conductivity of the material.

It has been shown ([8]) that Equation 1.3 or any of its variants (including integral form) could be used to approximate the entropy generation in any given problem. Then Equation 1.1 could be used to calculate the change in stagnation pressure and stagnation temperature. The important point to be made here, then, is that viscous or heat transfer effects cause entropy generation; this generated entropy manifests itself in terms of lost stagnation quantities.

1.3.4 Leakage Related Losses

It is customary to divide leakage related losses in two parts: losses inside the tip gap and losses due to mixing once the flow leaves the gap. A lot of effort has gone into characterizing the two kind of losses and evaluating their relative importance.

Losses inside the gap are generated in the boundary layer at solid surfaces and through mixing that occurs in the gap between the shear layer at the edge of the separation bubble and the rest of the leakage flow. The mixing losses depend on the extant to which the mixing has been completed. Mixing gets completed for longer gaps, so the losses would depend on the ratio of the gap height to the maximum blade thickness.

Most of the loss occurs when the leakage flow emerges from the gap and mixes with the freestream. The mixing is turbulent. Kinetic energy is extracted from the mean flow by the work it does against Reynolds stresses. This work appears as the production term in the energy balance equation and represents transfer of energy from the mean flowfield to the turbulent flowfield. The turbulent energy is dissipated into internal energy through viscous effects.

1.4 Heat Transfer in Blade Passages

Heat transfer investigations in open literature is limited to cascades. One needs to consider heat transfers in the inner and the outer endwalls and heat transfer on the blade surface.

1.4.1 Endwall Heat Transfer

There are results available ([10]) for two different boundary layer thicknesses, which serves to highlight the role of secondary flow in heat transfer. The following are the major conclusions.

1. Very high levels of heat transfer (St 4.0×10^{-3}) are found on the endwall near the blade leading edge. This corresponds to the presence of horseshoe vortex. The region features high momentum transport and associated high shear stress. Results indicate that there is little difference in the heat transfer levels for thick and thin boundary layers. However, relatively larger areas are affected by the high Stanton number when the boundary layers are thicker.

2. The combined horseshoe-passage vortex system crosses the passage from the pressure side to the suction side. This vortex leaves its mark on the endwall by a trail of thin high heat transfer (St 3.5×10^{-3}) zone.

3. The region next to the pressure side has the lowest values of heat transfer (St 2.0×10^{-3}). This is the region where a new boundary layer develops, since the inlet boundary layer has been consumed by the horseshoe vortex system.

4. Another high heat transfer region (St 3.5×10^{-3}) occurs near the passage throat. This is possibly an effect of flow acceleration in this region.

5. The region corresponding to the wake shows the highest heat transfer (St 4.5×10^{-3}).

6. Stanton number remains relatively constant (St 4.0×10^{-3}) downstream of the trailing edge outside the wake region.

1.4.2 Blade Surface and Tip Heat Transfer

Results are available from a rotating rig ([3]). The same study also covered heat transfer on the endwalls and the results are very similar to the ones stated above. This would indicate that the endwall heat transfer characteristics stay largely the same in a rotating rig. The main results for tip heat transfer are as follows.

1. Pressure surface Stanton numbers are relatively uniform and low in magnitude. They vary from 0.8×10^{-3} near the leading edge to near zero near the trailing edge. There is a slight increase in the Stanton number near the tip region and this corresponds to the initiation of the tip leakage flow.

2. The Stanton number is lowest near the midspan on the suction side, and increases as one goes towards the hub or towards the tip.

3. Stanton numbers near the tip are almost double of that near the midspan. This increase is definitely related to the tip leakage flow.

4. The increased value of the transfer near the hub region could be traced to the passage vortex system.

There has been a few other experiments on tip heat transfer, not based on rotating rigs and cascades, but based on idealized geometries ([25], [31], [24], [21]) These studies show that the pressure side acts like a sink, it gives rise to high velocities and accelerations into the tip gap, resulting in localized regions of high heat transfer. Also, the suction side, which acts as a source, establishes higher heat transfers than the pressure side. Computational results ([1]) show that regions of high heat transfer are localized in the leading edges of the blade tip and along the edge of the suction side. The leading edge region could be explained by the fact that the fluid in this part retains the high temperature from upstream. There are high favorable pressure gradients on the suction side and this might explain high heat transfer as the fluid accelerates.

1.5 Turbine Tip Desensitization Efforts

Few desensitization efforts have been published in open literature. Most of the ideas are available in patents, and whether any of these ideas are implemented in a production turbine is open to question. The basic theme that runs through all these ideas is to reduce the amount of leakage mass, thereby reducing pressure losses and thermal loads on the blade tip. A short list of some of the desensitization ideas is given below.

rubstrip This is a special material that cover the tip and provides very little clearance. Clearance in turbines usually vary with operating conditions. During occasional rubs, the abrasive material is worn away without causing much damage to the turbine blade itself. However, rubbing of the tip complicates tip coolant injection, and rubstrips are mostly confined to low pressure stages where cooling is of lesser importance.

squealer tips This is an extension of either the pressure or the suction surface or both, radially outward from the blade tip. When both the surfaces are extended, a rim with a cavity forms at the blade tip. Coolant in injected into the cavity, and that helps to thermally isolate the blade tip from the hot leakage gases. The rim is usually very thin, and the risk from incidental rubs is also reduced. Various squealer designs have been suggested ([29], [20], [19]), trying to combine coolant injection and squealer aerodynamics to maximum advantage.

tip cooling The use of tip cooling has been suggested ([5]) to block the leakage mass from entering the clearance gap.

partial shroud Instead of having annular shrouds running in a ring around the blades, a partial shroud arrangement has been suggested ([14]). Here one finds winglet shaped devices extending both to the pressure and the suction sides, with grooves to facilitate coolant injection. Several other winglet configurations have also been investigated ([4]).

Chapter 2

Experimental Facility

2.1 Facility Description

2.1.1 Turbine Rig

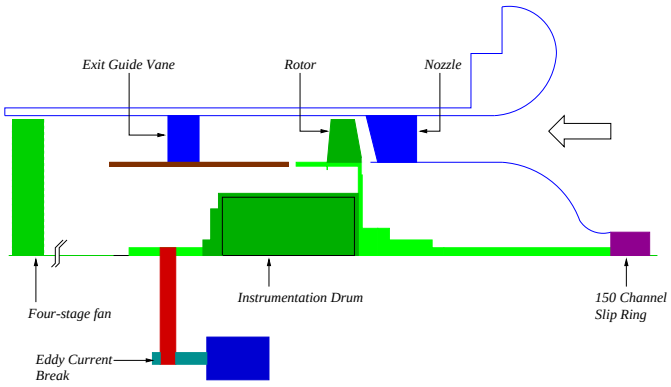

Fig. 2.1. Schematic of Penn State Axial Turbine Research Facility

The Penn State Axial Turbine Research Facility was completed in early nineties to provide facilities to take aerodynamic data in a rotating environment (Figure 2.1). This is a low speed, open circuit facility, in which a single turbine stage is driven by two adjustable pitch axial flow fans. A set of exit guide vanes direct the flow out of the rotor to a more axial direction. The power generated by the stage is absorbed by an eddy current brake which is also used to

control the rotational speed of the rotor. The brake is water cooled. Effects of variations in inlet temperature is corrected by operating the rig at the corrected speed, which depends on ambient temperature. This fact follows from the non-dimensional grouping of parameters for axial turbine performance([16]), which states that

$$\frac{p_{01}}{p_{03}} = f\left(\frac{\dot{m}\sqrt{RT_{01}}}{p_{01}D^2}, \frac{\Omega D}{\sqrt{\gamma RT_{01}}}\right)$$

where 01 and 03 are the turbine inlet and outlet stagnation states, D is the inlet diameter of the turbine, $\dot{m}$ is the mass flow through the turbine and Ω is the rotational speed. For a given pressure drop (which is fixed by the fans in AFTRF), one expects to keep the same mass flow by fixing the value of the second parameter, hence

$$\frac{\Omega}{\sqrt{T_{01}}} = \text{constant}$$

This constant in AFTRF is 1.276. Here Ω is in Hz and T_{01} in K.

The stage inlet and outlet total temperatures are monitored by a pair of thermocouples. There are provisions to measure mean inlet and exit speeds at blade midspan locations by pitot static probes. An optical sensor located on the main shaft reads the rig rotational speed. Ambient pressure and temperature are always monitored during tests. A torque meter, connected to the main shaft by a belt system, measures the torque and the horsepower produced by the rotor. There are also provisions to monitor the rig vibration levels by linear accelerometers located on the front and the back bearings.

The total temperature difference between the upstream and the downstream thermocouple measurements is 5 K at the design rotational speed. The power produced by the turbine is 60.6 kW. Table 2.1 shows the geometric and performance characteristics of the turbine as a whole. Table 2.2 shows geometric parameters of the rotor and the nozzle.

Measurements in AFTRF are taken either in the stationary or in the rotational frame. Stationary frame measurements utilize a measurement window (240 mm by 530 mm) located by the side of the rig. Optical measurements (laser doppler velocimetry, image acquisition) utilize the same window. Rotational frame measurements utilize the instrumentation drum shown in Figure 2.1 that rotates with the rotor. An array of sensors are installed inside the drum, including hot wire anemometer bridges and multichannel pressure sensors. The data collected inside the instrumentation drum is transferred to the stationary frame using a 150 channel slip ring.

2.1.2 Turbine Blades

The blades for the rotor and the nozzle were designed by General Electric. Stage loading, reaction, aspect ratio and blade turning angles reflect current design practice for high pressure turbines.

Most of the current work concerns the tip section of the blade. Figure 2.2 shows the tip airfoil shape. Here the blade chord has been normalized to unity. Figure 2.3 gives the velocity triangle at the blade tip. A 3D isometric view of the stage is shown in Figure 2.4.

Details about static pressure distribution for the blades at various span locations are given in [37] and [38]. Data for nozzle and rotor design pressure and temperature distributions are given in [45] and [30]. Velocity and pressure measurements taken inside the AFTRF rotor passages are given in [38] and [22].

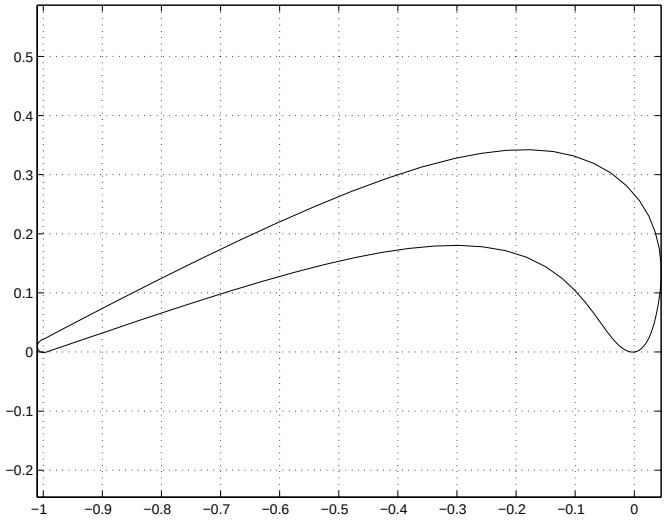

Fig. 2.2. Blade tip airfoil shape

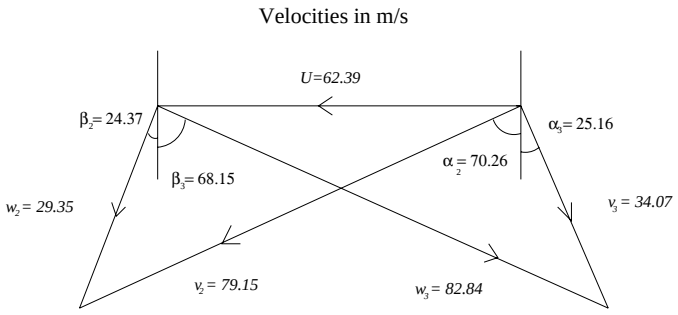

Fig. 2.3. Velocity triangle at the blade tip

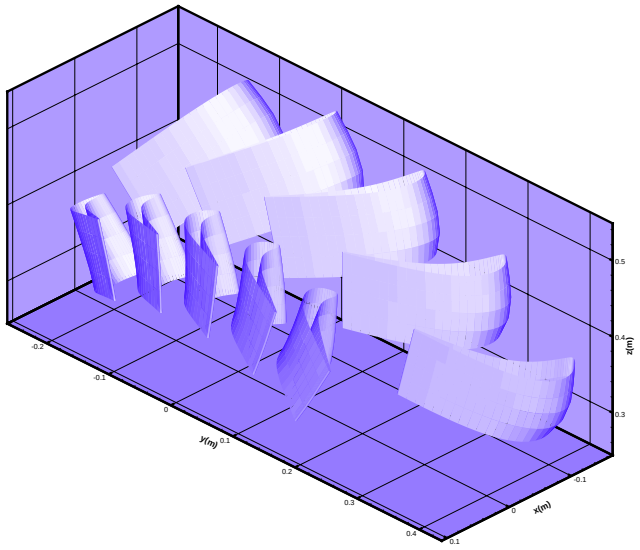

Fig. 2.4. Isometric view of a part of the AFTRF turbine stage

The clearance gap near the tip of the blades vary. Five blades are special, and their clearances could be adjusted by thermoplastic shims. The nominal clearance for the remaining 24 blades is 0.76 mm (0.030 in). The maximum clearance available in one of the five adjustable-clearance blades is 1.65 mm (0.065 in).

Further details of the AFTRF could be found in [45], [23] and [17].

2.2 Facility Modifications

The AFTRF had to be modified considerably for the present work to accommodate the various tip desensitization schemes that were designed, and this involved modifications of both the rig and the blades. Three desensitization schemes were tested during this study.

1. Coolant injection from the blade tip
2. Tip platform extension
3. Squealer tip designs

The first scheme needed modification of both the rig and blades, while changes were made to a single “test blade” for the last two schemes. In addition to these three, heat transfer measurement on the blade required modification of both the blades and the rig.

2.2.1 Rig Modifications for Coolant Injection Studies

Coolant injection from the rotating blades makes it necessary to have an air passage from a plenum outside the rig to injection holes on the blade surface. Hence an air transfer system was designed to transfer air from stationary plenum to the rotating blades. A schematic of the air transfer system is given in Figure 2.5. Two cylindrical drums were created, one stationary

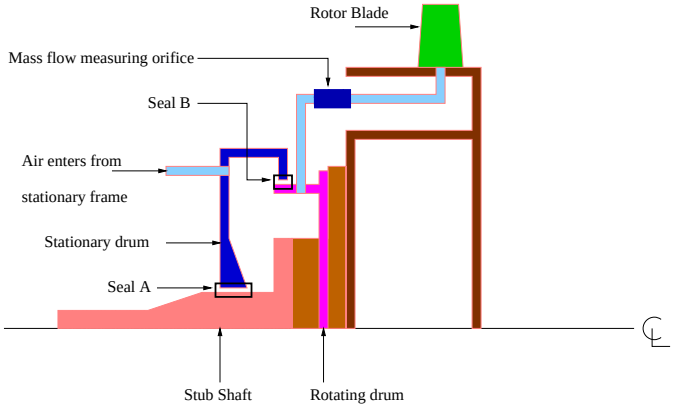

Fig. 2.5. Schematic of the air transfer system

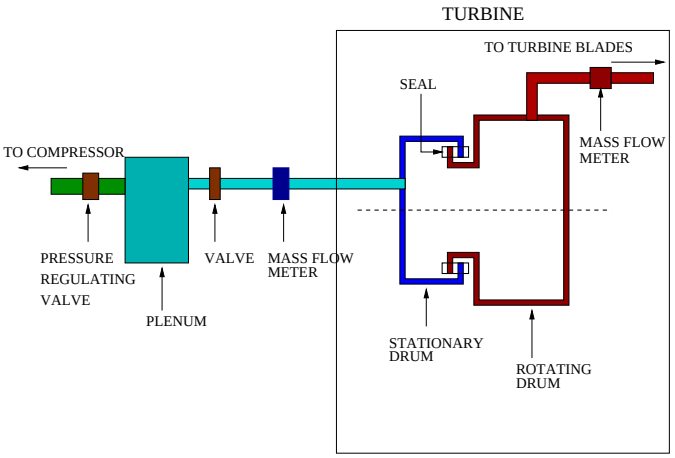

Fig. 2.6. Schematic of the plenum arrangement

(shown in blue) and the other rotating (shown in pink). Seal A, placed between the stationary drum and the rotating shaft, and seal B, placed between the two drums, ensured minimal coolant fluid leakage. A stagnation chamber was created by the combined volume of the stationary and the rotating drums. This stagnation chamber received regulated air from a plenum outside the rig (not shown in Figure 2.5) through high pressure PVC tubing. The air from the rotating stagnation chamber was then transfered to the blades through flexible PVC tubing. Orifice mass flow-meters were installed on the rotating tubing for measuring mass flow in the rotating frame. The flow-meters used pressure sensors inside the rotating drum. The external plenum available to the rig consisted of high pressure tank capable of storing air up to 20 bars, with blowing rates controlled by pressure regulators (Figure 2.6). Cooling air is available for approximately 3 hours of continuous operation. The plenum was held at 2.5 bars during the runs, which ensured that all the subsequent throats in the air passage were choked.

The nominal coolant mass flow in each of the blades was 1.1 g/s. Hence, had there been injection from all the 29 blades, the coolant mass flow would have been 0.3% of the total mass flow.

2.2.2 Blade Modifications for Coolant Injection Studies

Five of the twenty nine rotor blades were modified for coolant air injection. A schematic of the coolant passages in the blade is shown in Figure 2.7. There are four such cooling holes in each blade, arranged in a straight line. Three of them have a diameter of 0.5 mm and inject towards the pressure side, as shown in Figure 2.7. The one near the trailing edge is different from the rest. It injects radially, and has a diameter of 1.8 mm. The plenum chamber at the bottom of the blade supplies air for all the four holes. All the four holes were originally drilled

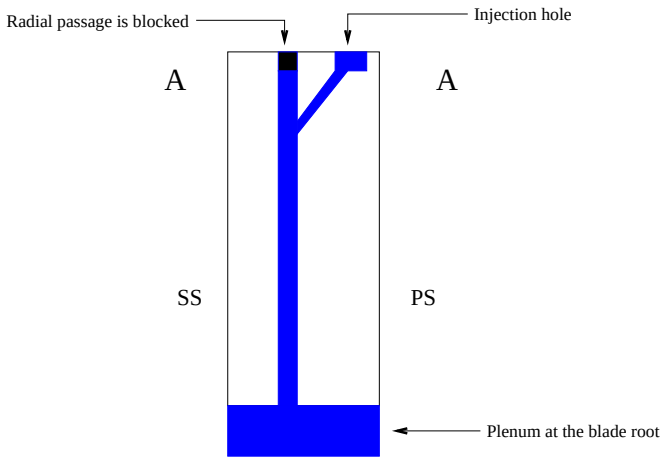

Fig. 2.7. Schematic of the cooling holes inside the turbine blade

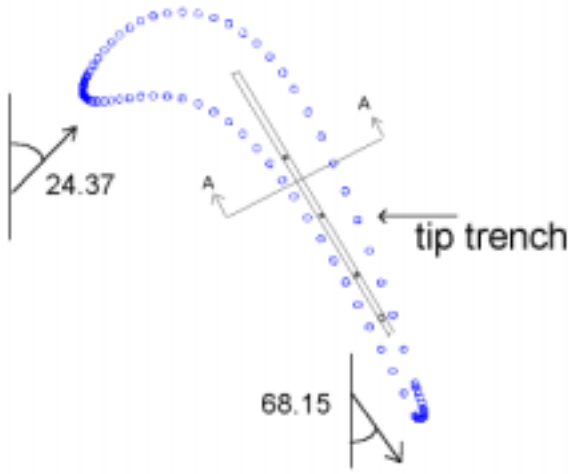

Fig. 2.8. Tip airfoil with cooling trench

straight down. Then, for the leading three holes, the straight passage was blocked, and an oblique passage was drilled in such a way as to meet the straight passage. The fourth and the largest hole does not have this oblique passage. All the four holes inject in a “trench”.

Figure 2.8 shows the tip airfoil with the cooling trench and the coolant holes.

2.2.3 Modifications for Tip Platform Extension Studies

Tip platform extension, also called winglet, was the second desensitization experiment that were conducted in the AFTRF. Conceptually, these are similar to the winglets used in some airplane wings. The winglets were made of thermoplastic shims, which were attached to the tip surface using 3M high shear resistance double-sided tape. Winglets extended either towards the pressure side of the blade or towards the suction side.

Figure 2.9 shows the geometry of the pressure side winglets. It was predicted that the extensions would be most effective at locations where the pressure gradients were strongest, which was near 60% axial chord for the AFTRF rotor blade, as shown in data previously taken at AFTFR ([37]). Hence all the pressure side winglet designs tested has a “bump” near 60% axial chord. The extension size is smoothly decreased from w at this point to zero near the leading and the trailing edges. Two values of w were tested. The case of $w = 4.76$ mm will be referred to as the narrow PS extension (or the PS-narrow case), while that of $w = 6.35$ mm will be called the wide PS extension (or the PS-wide case).

Figure 2.10 shows the geometry of the suction side winglets. Two configurations, henceforth called SS-1 and SS-2, were tested. SS-1 had an extension which narrowed down to zero near the trailing edge while SS-2 had a constant extension all the way to the trailing edge point. The geometry of the extensions near the leading edge for both SS-1 and SS-2 were identical.

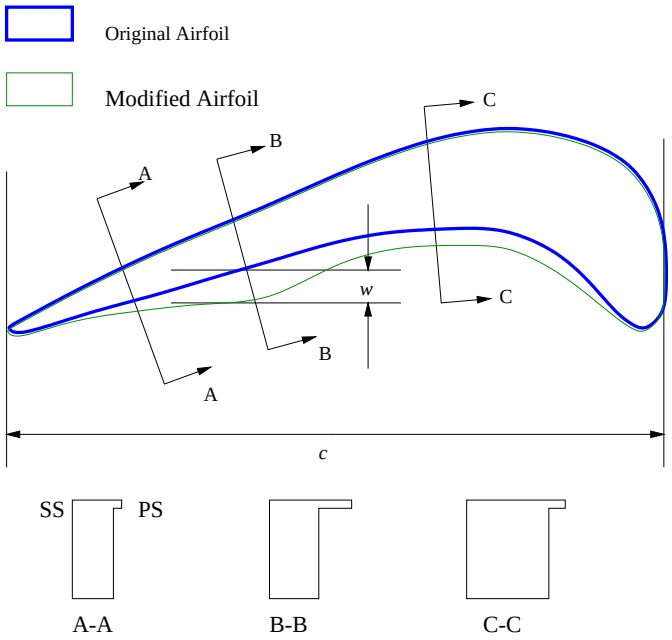

Fig. 2.9. Geometry of the pressure side extensions (PS)

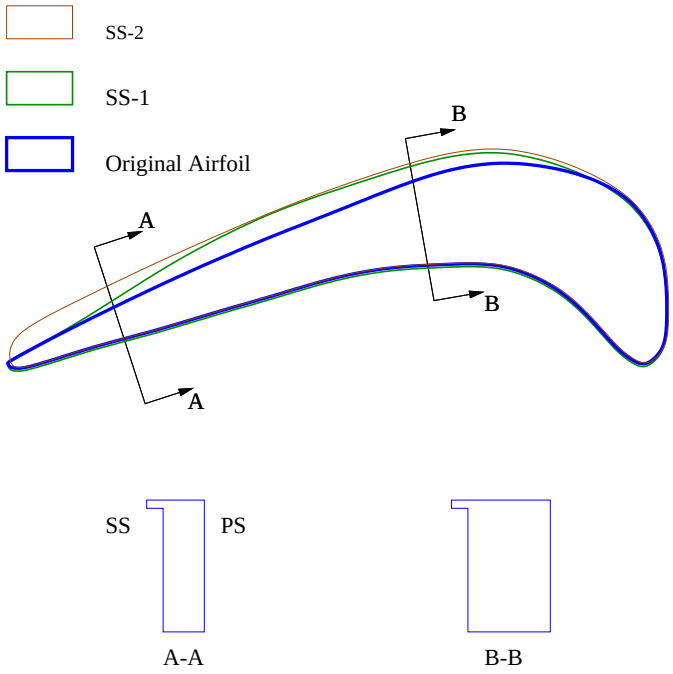

Fig. 2.10. Geometry of the suction side extensions (SS1 and SS2)

All of the configurations investigated are summarized in Table 2.3.

2.2.4 Modifications for Squealer Tip Studies

Squealer tips are currently used in production turbines as a tip desensitization strategy. A squealer tip is a blade tip treatment where the central part of the blade tip surface is recessed, leaving a thin rim which is much closer to the outer endwall than the center. Overall, a squealer tip resembles a cavity below a moving wall. The squealer tip geometries tested in AFTFR were a little different then production squealer tips. Two geometries were tested. The first one, shown in Figure 2.11, would be termed as Suction Side Squealer (SSSq). This featured an almost constant width rim extending from the trailing edge to different lengths along the suction side of the blade tip. The other one, shown in Figure 2.12, would be termed Squealer Channel (SqCh). This featured a channel formed by one of the suction side rim of SSSq configurations and a pressure side rim of varying length. Table 2.4 shows the test matrix of the squealer configurations tested.

Three configurations of SSSq were tried, as shown in Figure 2.11. The thickness w of the squealer rim was 4 mm for most of its length, shortening to 2.5 mm near the trailing edge. It should be recalled that the maximum blade thickness is 22 mm, the the rim was no more than 18% of the maximum blade thickness. The rim was made of thermoplastic shim, and was attached to the blade surface using double sided tape. Configuration SSSq-A was provided the shortest rim, extending from the trailing edge of the blade to 22% chord, SSSq-B extended from trailing edge to 4% chord, and SSSq-C extended almost all the way from the trailing edge to the leading edge.

Two configurations of SqCh was tried. Both featured SSSq-B on the suction side. On the pressure side, SqCh-A had a pressure side rim extending from 25% to 62% chord. SqCh-B

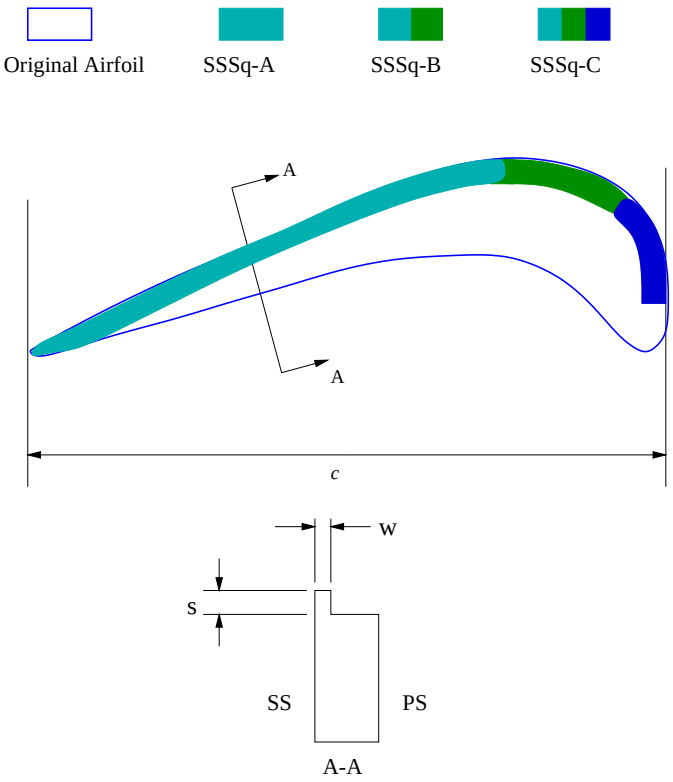

Fig. 2.11. Geometry of suction side squealer tip

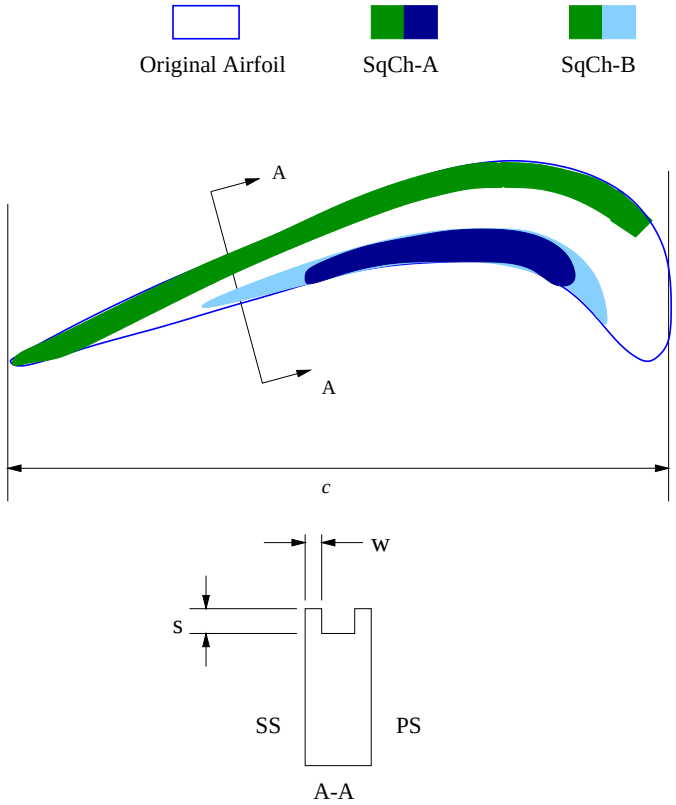

Fig. 2.12. Geometry of channel type squealer tip

had a longer rim, extending from 22% to 66% chord. The pressure side rim in both of these was slightly tapered in shape, and had a maximum thickness of 5 mm.

2.2.5 Modifications for Heat Transfer Studies

The AFTRF intakes air at ambient temperature. In order to conduct a heat transfer study, it is necessary to heat the blade in some fashion. The heat transfer coefficient h could be determined between the heated blade and the cold fluid, and this would be the same value as h between the heated fluid and the cold blade. Only the blade tip surface needs to be heated if the h values on the blade tip is desired. The blade tip could be heated by a heater foil surface with a relatively high resistance, and passing a large current through the foil would provide for adequate heating, $\dot{q}_{gen}$. The next step is to measure the surface temperature (T_s), which in the present case is done using liquid crystals. Assuming a reference temperature T_{ref} equal to inlet total temperature T_{in}, one obtains the heat transfer coefficient h from

$$\dot{q}_{gen} = h(T_s - T_{ref})$$

The objective is to install electrical connectors near the rotor blades to connect it to the power supply outside the rig. The slip ring unit is capable of handling currents up to 5 A, and so seven power lines are provided to seven connectors near the hub surface close to the five modified blades, as shown in Figure 2.14 The design of the connector screws is shown in Figure 2.13. A copper tube, shown here in pink, is electrically connected to the the power supply outside the rig through the slip ring. The heater foil could be connected to this using the screw, shown in brown.

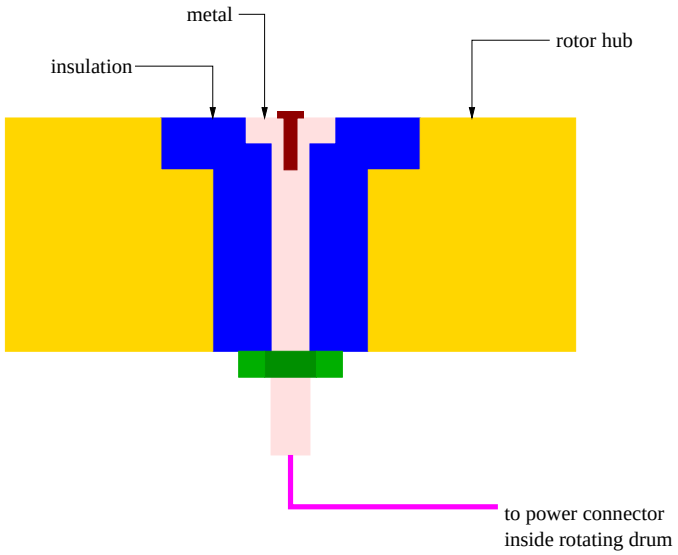

Fig. 2.13. Design of the screw terminal on the hub surface

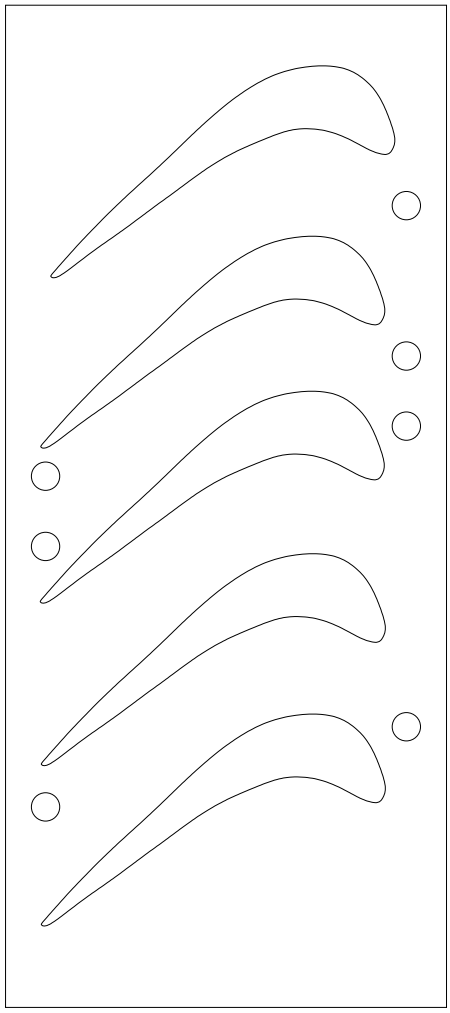

Fig. 2.14. Location of the screw terminals on the hub surface

A plastic insulation, shown in blue, surrounds the copper and separates the electricity line from the turbine metal, which is grounded.

2.3 Facility Instrumentation

2.3.1 Rotating Drum Instrumentation

The rotating drum of the AFTRF is designed to house a considerable amount of instrumentation. Some of the instrumentation was already available from previous research programs, while a few had to specifically designed and installed for the present project. The ones used in this study are described below. The instrumentation inside the drum is relevant for the rotating frame five hole probe measurements.

Transducer The principal sensor used for rotating frame pressure measurements is a 6.894 kPa (1 psi) differential pressure transducer from PSI Systems. The transducer has 32 channels, and there is a common reference channel available to all the sensing channels. The reference pressure is the static pressure inside the rotating drum. The transducer output is fed to terminals on stationary frame through the slip ring, without any conditioning in the rotating frame. The unit measures pressure at one channel at a time. Signal to select a desired channel is fed from the stationary frame through the slip ring. A built-in electronic unit performs the channel switch.

Absolute pressure transducer This is used to measure the absolute static pressure inside the rotating drum. This pressure is close, but not identical, to the mean static pressure in the flow. The transducer, made by Data Instruments, has a range of 1 bar. This transducer is mounted on a custom built circuit board, which also houses an amplifier and a power

supply for the transducer. The amplified output is passed through the slip ring to a screw terminal in the stationary frame.

Traversing arm An metallic arm to hold the pressure probe is fitted with two Syn-Sym stepper motors. The bigger stepper motor moves the arm circumferentially while the smaller motor moves the transducer radially in and out. The resolution of the motor provided 1000 steps per inch in the radial direction and 1150 steps per inch in the circumferential direction. There are two such arms 180 degrees apart to provide the necessary balance to the rotor. Power needed to energize the motors is fed through the slip ring.

A 150 channel brush type slip ring is used for rotating flow measurements. The slip ring is connected to a screw terminal outside the rig.

2.3.2 Five Hole Probe

A five hole probe is used to measure five flow quantities at a point (Figure 2.15). These are the 3 velocity components, the total and the static pressure. The probe operates by measuring five pressures at a location. The velocities and the pressures are obtained from these measurements by linear interpolation from a calibration chart. The procedure has been described in detail in literature ([35]).

The probes used for this study were fabricated locally. The five small tubes with approximately 0.75 mm OD were bundled together, silver soldered, cut at $45\,\mathrm{deg}$ angle and polished. The diameter of the probe head was 1.65 mm. Details regarding the calibration of the probe could be found in [23].

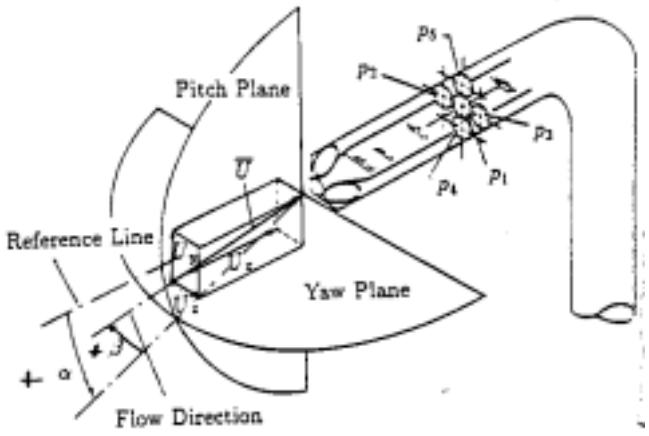

Fig. 2.15. Five hole probe

The rotor exit flow is mapped at two axial locations, at 38% and 46% of the chord length, downstream of the rotor. The axial positions are hereafter referred to as $d = 0.38c$ and $d = 0.48c$ measured from the leading edge plane of the rotor.

A test set consisted of a number of circumferential traverses at different radial positions. About 120% of a blade passage was traversed circumferentially for each radial position. The aim of the program was to document the secondary flow over the top half of the passage, and hence traverses were made between the radii of 50% and 96% span.

Four sets of tests were made. Baseline data at each of the two axial locations consisted of the dry (no cooling) case. Subsequently, another set of data was taken with cooling. The cooling flow was made to choke at the mass flow measuring orifices. This ensured that the coolant mass flow is solely a function of the stagnation pressure and stagnation temperature inside the rotating drum.

Typically, a five hole probe was used in the following fashion. Five channels of the PSI transducer were connected to the five hole probe using hard poly-ethylene pressure tubing. Signal was fed from a computer outside, selecting channel 1 in the PSI unit. Measurements from channel 1 were taken for a selected time. Then signal was fed to switch to channel 2. In the same way, measurements were taken for all the five channels. Then signal was fed to the circumferential motor to move certain number of steps. After a brief wait for the unsteadiness due to the motor movement to die down, five channels of data were taken again. The process repeated for a circumferential map, and then the radial motor was activated to move the probe to a different radial location and the process started all over. The absolute static pressure inside the drum was monitored in parallel.

A study was done to determine the necessary sampling time for the five-hole probe to ensure data repeatability. The idea was that a long enough averaging time would smoothen the unsteadiness of the data. It was found that 10 seconds of averaging was adequate, as the values of pressure for 10 seconds and for 15 seconds of averaging were identical. Details about this procedure could be found in [23].

The need to average the data at a given (r, θ) location for a relatively large time and the density of the mapping caused each test to take a relatively long time to complete. A map of the passage between 50% and 96% of the span typically took about three hours. Efforts were made to keep the rig inlet temperature within two degrees in this time period, although in certain tests, an inlet temperature increase of about 5 degrees was observed. Hence the two extreme points in a map were recorded at slightly different inlet temperatures and consequently different densities and rig mass flow. This was one of the sources of error in the measurements.

2.3.3 Kulite Probe

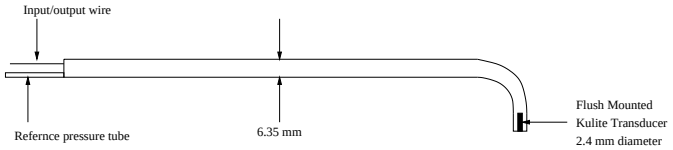

Fig. 2.16. Transducer and probe arrangement

Unsteady total pressure measurements were made using the XCS-062 transducer made by Kulite Semiconductors. The transducer had a range of 34.5 kPa (5 psi) and a frequency response of 150 kHz. It was flush mounted at the tip of the probe holder, as shown in Figure 2.16, for eliminating the time response canceling detrimental effects of a cavity with finite volume. The diameter of the transducer was 1.59 mm ($1/16^{th}$ inch). The transducer was differential, and had a tube connecting the diaphragm to the atmosphere.

Figure 2.17 shows the instrumentation setup. The probe was mounted on a traversing arm which was attached to the casing of the facility. A stepper motor attached to the traversing arm moved the probe horizontally, hence the radial position of the transducer with respect to the blades could be changed. The signal from the transducer was fed to an amplifier and a low pass filter. The conditioned signal was acquired at 40 kHz in a PC equipped with National Instruments PCI 6110-E multipurpose I/O board. This board also activated the stepper motor through a Herbach and Rademan motion control board. The acquisition of the analog voltage

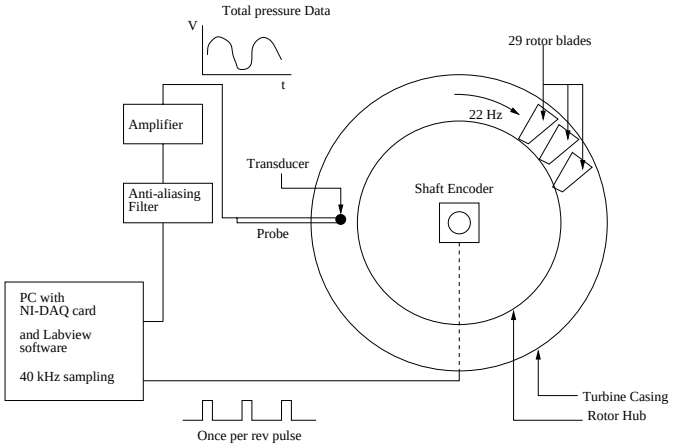

Fig. 2.17. Instrumentation for fast response probe

from the pressure transducer was triggered by an once per revolution pulse from an optical RPM sensor mounted on the turbine shaft. Labview software orchestrated the whole effort.

The unsteady total pressure measurement worked as follows. 2000 data points were acquired at 40 kHz, providing 50 ms of continuous data at a given radial position of the transducer. This was roughly the time for one revolution of the rotor (45.4 ms), which nominally spun at 22 Hz. Hence data from all 29 blades were taken. This data constituted an ensemble. 200 such ensembles were acquired and the ensemble average calculated, and then the transducer was moved to a different radial location. The ensemble averaged data was stored. Ensemble averaged total pressure from 63 radial locations formed a total pressure map. The radial position of the traverses were 1.587 mm ($1.29\%h$) from each other. Hence 81.3% of the passage was covered radially, from $r/h = 98.7\%$ to 17.4%. It must be remembered that the probe was mounted on the stationary frame, and any data close to the relatively moving inner endwall was bound to be

influenced by the wall motion. Also, the probe incidence was the design flow incidence near the tip to the blade (68.15°). Total pressure probes are usually accurate within $\pm 10^{\circ}$ of the head-on value. Since the flow angle from the inner to the outer endwall in the AFTFR changes by as much as 25°, probably the data in the top three quarters of the map was most accurate.

The transducer repeatability and hysteresis are within 0.1% full scale, that is, within 35 Pa (manufacturer values). The mean total pressure ratio at the rotor exit is $p_0/p_{in} = 0.94$ which is about 6 kPa or 17% full scale. The value of p_0/p_{in} varies between 0.935 and 0.945, which is a variation of the order of 1 kPa, or about 3% of full scale.

The calibrations used for this study are

$$p_0 = p_{in} - \delta p$$

$$\delta p = -7000(V_{in} - V_{offset})$$

where p_0 and δp are in Pa. The starting offset voltage V_{offset} is around -0.358 ± 0.001 V. The input voltage from the transducer V_{in} is of the order of -1.2V. The 1 mV uncertainty in V_{offset} translates to 7 Pa, which is smaller than the transducer resolution.

All the measurements taken by the five hole probe and the Kulite probe are done in a downstream plane, as shown in Figure 2.18. The distance d is $0.38c$ and $0.48c$ for five hole probe measurements and $0.3c$ for Kulite probe measurements.

As mentioned earlier, the Kulite transducer and probe are used in both the tip platform extension and the squealer desensitization studies.

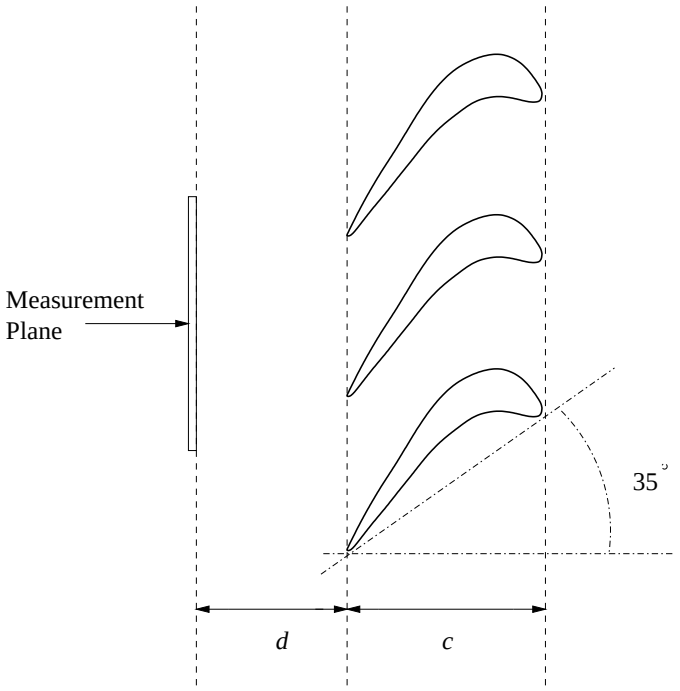

Fig. 2.18. Measurement plane for five-hole and Kulite probes

2.3.4 Data Acquisition

The rotating five hole probe data was acquired using a Labtech software using the MetraByte DAS-20 A/D card. The motor traverse was done using MSTEP software developed at Techcore Inc. and Metrabyte MSTEP3 motion control board. The Kulite based measurements were done entirely with Labview software from National Instruments. Data was acquired using National Instruments E Series multi-purpose data acquisition board.

2.3.5 Instrumentation for Heat Transfer Studies

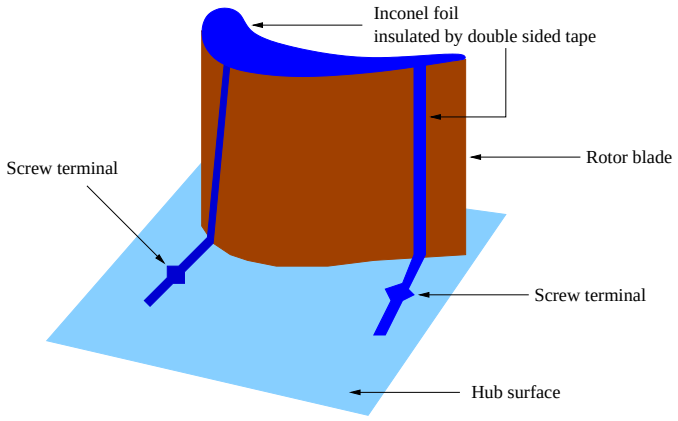

Fig. 2.19. Heater foil connections to screw terminals

Figure 2.19 shows the general scheme in which the heater foil on the blade tip is connected to the screw terminals on the hub endwall, shown in Figure 2.13. It is important to insulate the heater foil from the metal surface underneath both electrically and thermally. Hence

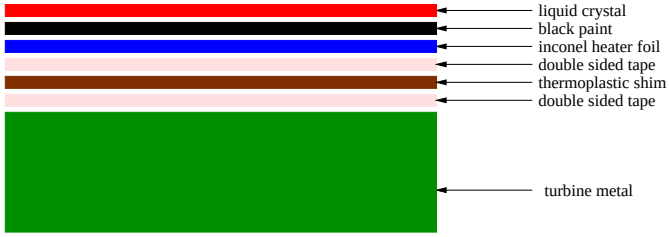

Fig. 2.20. The layering scheme used to install heater foil

a layered arrangement is made, as shown in Figure 2.20. This scheme is followed on the blade tip, where thermal insulation is of utmost importance. The thickness of each of these layers is less then 100 μm, except for the thermoplastic shim, which has a thickness of 250 μm. The thermoplastic shim layer and the liquid crystal layer are not used in regions other than the blade tip, for this study focuses solely on the temperatures measurements of the blade tip.

inlet total temperature T_0	289 K
inlet total pressure p_0	101.36 kPa
mass flow $\dot{m}$	11.05 kg/s
specific work output $\delta h/W$	5.49 kJ/kg
flow coefficient $\dot{m}\sqrt{T}/p$	1.85 $kg\sqrt{K}m^3/kNs$
speed coefficient $N/\sqrt{T}$	77.69 $rpm/\sqrt{K}$
rotational speed Ω,N	22 Hz, 1320 RPM
Total pressure ratio p_{01}/p_{03}	1.0778
Total temperature ratio T_{01}/T_{03}	0.981
total pressure drop $p_{03} - p_{01}$	7.471 kPa
hub reaction	0.181
pitch-line reaction	0.382
hub loading coefficient	5.27
pitch-line loading coefficient	3.76
stator zweifel coefficient	0.7347
rotor zweifel coefficient	0.9759
power output	60.6 kW
midspan blade speed U_m	54.89 m/s

Table 2.1. Turbine performance parameters

rotor	
number of blades	29
chord length (c)	128.7 mm
maximum thickness	22 mm
spacing or pitch	102.8 mm
tip turning angle	95 degrees
hub turning angle	126 degrees
nominal tip clearance	0.76 mm (0.030 in)
tip clearance of test blade	1.65 mm (0.065 in)
tip radius	458.2 mm
blade height (h)	123 mm
leading edge diameter	7.62 mm
trailing edge diameter	2.54 mm
nozzle	
number of blades	23
chord length	176.8 mm
maximum thickness	38.8 mm
turning angle	70 degrees
nozzle to rotor spacing	25.6 mm

Table 2.2. Turbine performance parameters

$(t/h) * 100$	1.14	0.93	0.83	0.72
PS-narrow	$\surd$	$\surd$		$\surd$
PS-wide			$\surd$	$\surd$
SS-1	$\surd$			
SS-2	$\surd$			

Table 2.3. Test matrix for winglet configurations

$(t/h) * 100$	1.03	0.72
SSSq-A	$\surd$	$\surd$
SSSq-B	$\surd$	$\surd$
SSSq-C	$\surd$	$\surd$
SqCh-A		$\surd$
SqCh-B		$\surd$

Table 2.4. Test matrix for squealer configurations

Chapter 3

Baseline Flowfield

3.1 Velocity and Total Pressure Measurements in the Rotating Frame

A five hole probe measures all three components of the velocity as well as the total and the static pressures. Flow angles (pitch and yaw) could be derived from the velocity components. From five hole probe measurements it is possible to plot the secondary velocity vectors superimposed on top of the total pressure contours. This gives a clear picture of the process by which the velocity field is related to the loss field. This method also enables one to pinpoint the losses associated with the leakage vortex and the losses associated with the passage vortex, as the two structures have different origins and have different loss characteristics.

As mentioned earlier, data was taken at two downstream axial locations, $d = 0.38c$ and $d = 0.46c$ (Figure 2.18). The idea behind this was to examine how the leakage and the passage vortices evolve over axial distance. Measurements at different axial locations downstream of a cascade could be found in literature ([43]), where the authors have taken data at the trailing edge and twice the chord downstream. Measurements were taken at two different tip clearances, $t/c = 0.6\%$ and $t/c = 1.4\%$. The data seems to indicate that the total pressure coefficient recovers half its value from the trailing edge to $d = c$.

Figure 3.1 shows the measured secondary velocity vectors superimposed on the total pressure loss contours. This represents the measurements taken in a plane $d = 0.38c$ downstream of the rotor exit plane. Pressure loss is indicated simply by the total pressure referenced to the

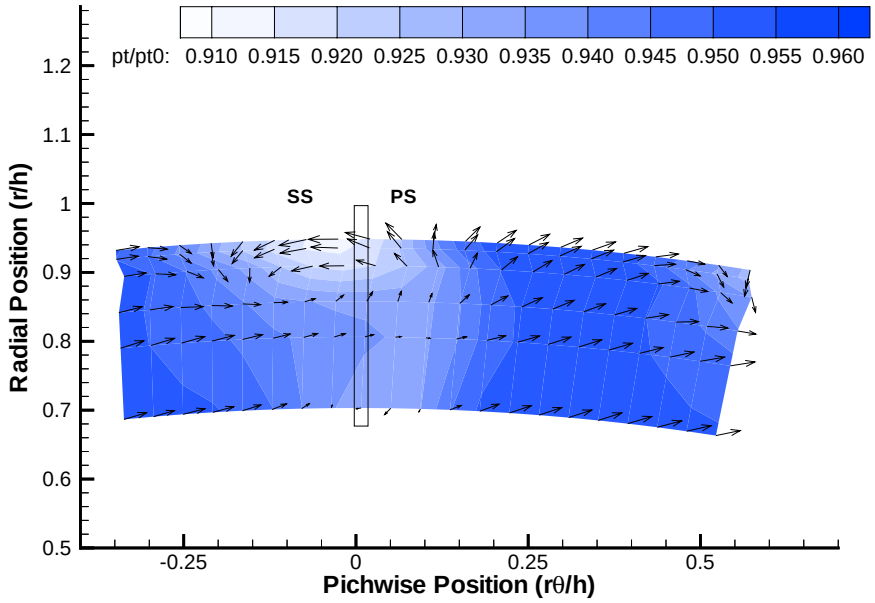

Fig. 3.1. Loss Contours and velocity vectors in the rotating frame, $d = 0.38c$, $t/h = 1.4\%$

ambient pressure, p_0/p_{in}. The vertical axis in this, as well as all subsequent contour plots, represents the non-dimensional radial location, referenced to blade height h. Hence the casing is along an arc at 1.0 in these units, and the hub is at 0.0. The horizontal axis represents non-dimensional pitch, again referenced to the rotor span. About 120% of the passage is visible. The location of the blade trailing edge is shown. There are two well defined vortical structures. The more prominent tip leakage vortex is centered around 88% span. This vortex is highly elongated, and appears as an ellipse rather than a circle. This elongation is possibly due to the large stresses in this part of the flow that stretches the vortex in the pitch-wise directions. A smaller elongation is experienced by the less prominent passage vortex, which is centered around 70% span. The passage vortex is weaker, but is spread out over a much greater area compared to the leakage vortex. Only the top half of the passage vortex is visible in this figure.

It is also possible that the leakage vortex pushes the passage vortex away from the outer endwall, although this cannot be inferred from this data. The issue could be settled only if sufficiently large number of axial locations are mapped in a rotating rig.

The two counter-rotating vortices are clearly interacting, and this interaction leads to stresses, turbulence generation and entropy generation, which leads to significant losses in mean kinetic energy of the passage flow. When two masses of fluid with opposite signs of vorticity are mixed, the sign of the vorticity in the resulting mass will depend on the relative quantities of mass and strength of the vortices. Thus fluid from the passage vortex, which mixes with the leakage vortex, could end up with vorticity of either sign. The extant of entrainment of the fluid from the passage vortex to the leakage vortex could be expected to increase as one goes downstream from the trailing edge. Hence it would be difficult to separate the losses due to passage vortex

and that due to the leakage vortex. However, there could be no doubt that the leakage vortex is stronger and more concentrated than the passage vortex in this rig.

The passage vortex originates due to the curvature of the blade passage and due to the blade inlet boundary layer. It follows that a larger turning will produce a stronger passage vortex. The blades have a very high turning angle of 95.5° near the tip and 105.3° near the hub. Hence the passage vortex that is observed here is expected to be strong. This is important to remember when comparing the results from AFTRF to results from cascade studies reported in literature, since many of these cascades ([7]) have shallow turning angles.

The peak of the loss contour do not coincide with the center of the leakage vortex. The loss peak occurs at a higher span, closer to the end-wall. This may be due to the fact that the leakage vortex interacts strongly with the outer casing of the turbine.

Figure 3.1 also shows the wake from the blade in addition to the two vortices. The losses in the vortices are larger than those in the wake.

Figure 3.2 is the traverse made at 46% of the chord from the trailing edge. The pattern in loss contour as well as the velocity vectors are similar to that of Figure 3.1. The whole pattern has shifted towards right, which indicates that the vortices, while being convected by the main flow, retains their structure. This is not surprising, given the close proximity of the two measuring locations. The leakage and wake related losses are distinctly visible. The center of the leakage vortex has shifted to about 85% span, so it is moving away from the outer casing. The leakage vortex core is away from the loss core. The loss is clearly spreading: same color contour lines encircle larger areas.

No measurements could be made beyond $d = 0.46c$ from the trailing edge due to mechanical constraints.

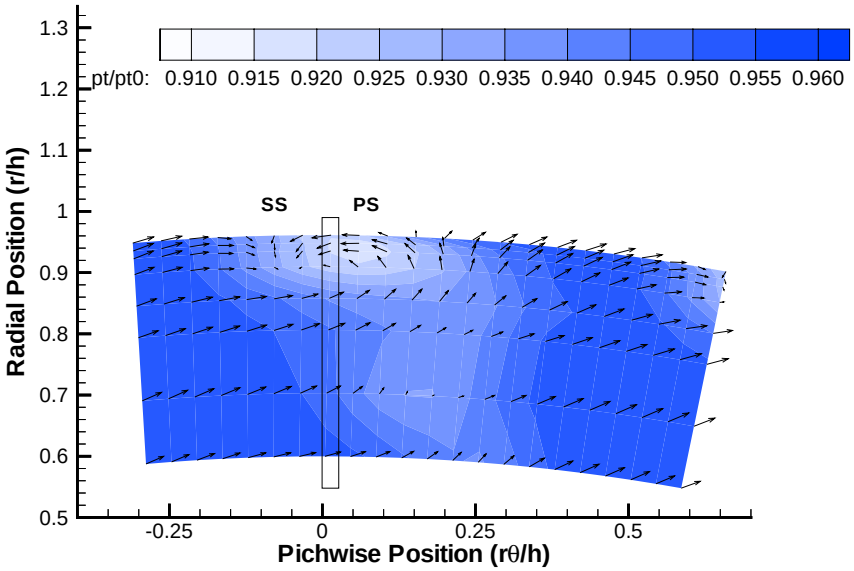

Fig. 3.2. Loss Contours and velocity vectors in the rotating frame, $d = 0.46c$, $t/h = 1.4\%$

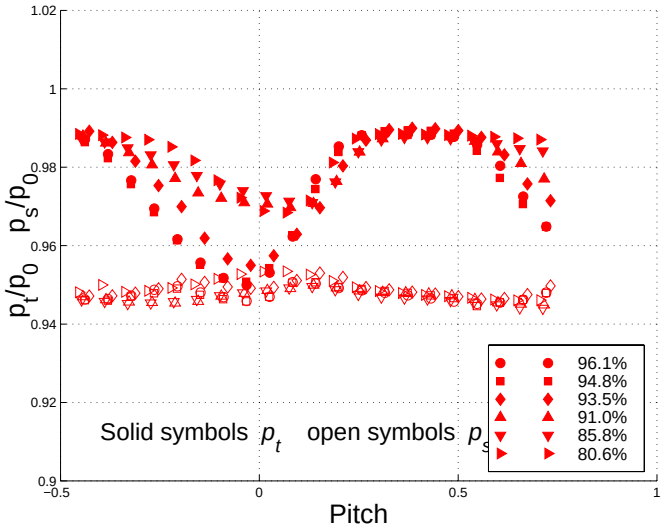

Fig. 3.3. Total and static pressure distributions at $d = 0.38c$

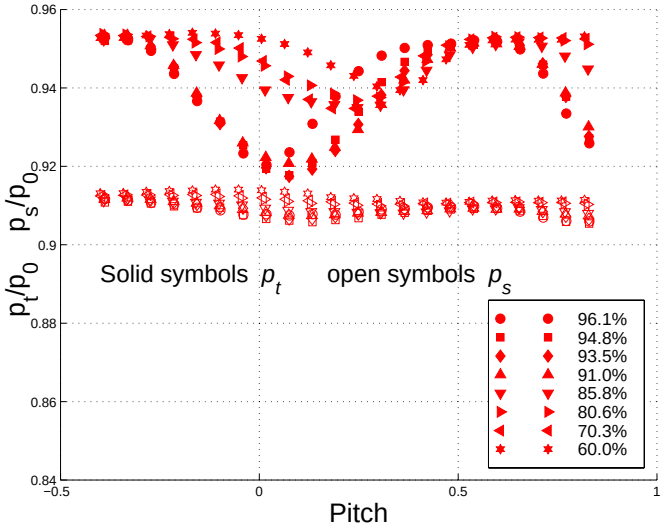

Fig. 3.4. Total and static pressure distributions at $d = 0.46c$

Figure 3.3 and Figure 3.4 show the pitch-wise distribution of total and static pressures at $0.38c$ and $0.46c$ locations respectively. Pressures at various radial locations are plotted together. The reluctance of the static pressure to change across the passage is obvious. The difference between the two pressures, especially near the tip, points to the very low kinetic energy of the flow near the leakage vortex core.

The total pressures at $0.46c$ are lower than total pressures at $0.38c$, due to mixing losses as the vortices travel downstream. The total velocity did not change significantly, so the average static pressure fell along with p_t, from $p_s/p_0 = 0.945$ to $p_s/p_0 = 0.91$ in this short axial distance. The two total pressure curves are almost identical.

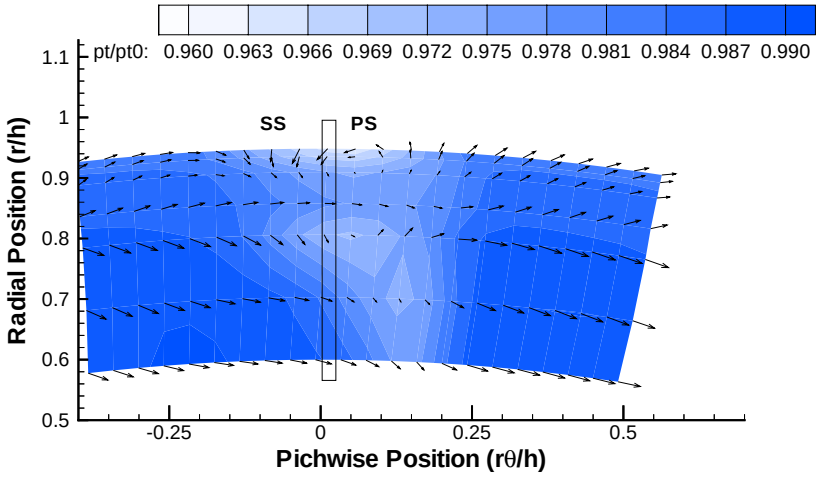

Fig. 3.5. Loss Contours and velocity vectors in the rotating frame, $d = 0.38c$, $t/h = 0.6\%$

Figure 3.5 shows the flow-field at the upstream location with a tip gap reduced to $t/h = 0.6\%$ (as opposed to the $t/h = 1.4\%$ in all the tests discussed above). It leakage vortex appears to be weaker for the reduced tip gap. The loss core is closer to the end-wall compared to the $t/h = 1.4\%$ case. The loss core may also be a somewhat shallower compared to above.

Figure 3.6 shows the velocity vectors at the $d = 0.38c$ traverse plane. The high turning that the flow experiences near the leakage vortex is evident.

3.2 High Frequency Total Pressure Measurement in the Stationary Frame

A Kulite probe with a frequency response of 150 kHz was used in the stationary frame to record the changing total pressure downstream of the rotor. The probe head was located $d = 0.3c$ behind the rotor trailing edge (Figure 2.18). Total pressures for all the 29 passages were recorded. Time accurate data was ensemble averaged over 200 ensembles to establish the average total pressure distribution in the rotor wake. However, results for two and a half passages are being presented here. The wake from the "test" blade and its neighboring "normal" blade to the right are discussed.

3.2.1 Test Blade at Normal Height

Figure 3.7 shows the "test" blade with its nominal tip gap of $t/h = 1.34\%$. The core flow in the passage is visible as the green high kinetic energy region extending from $0.30h$ to $0.75h$. The core flow that is seen here is not like a large region of uniform flow, as is usually assumed in two dimensional analysis, but is more like a jet, which centers around $0.55h$. The two wakes originating from the "test" blade and the neighboring "normal" blade are visible as purple zones of high loss. These wakes are slightly curved, unlike the relatively straight wakes

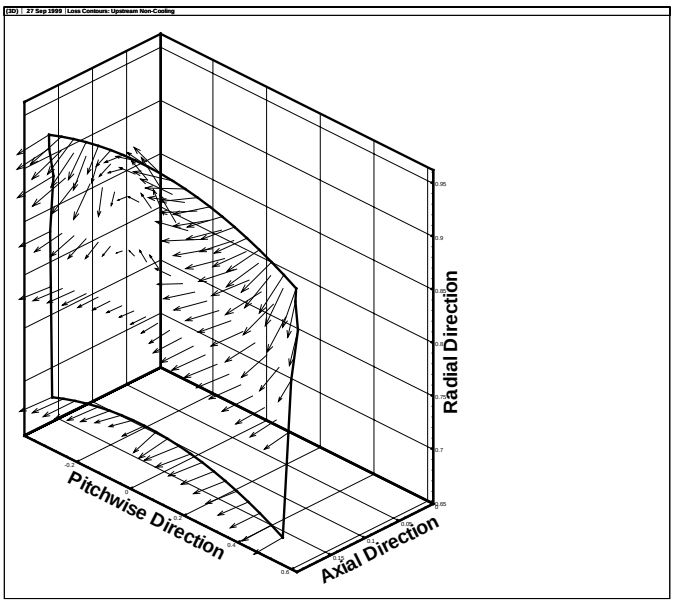

Fig. 3.6. Three dimensional velocity vectors at $d = 0.38c$, $t/h = 1.4\%$

that are recorded in stationary linear cascade studies. Slightly curved wakes form because of the more three dimensional and annular character of the present turbine stage. The wakes are not narrow, they occupy a significant portion of the passage. Data below $0.3h$ might be affected by the rotation of the inner endwall, since the probe is in the stationary frame.

The leakage vortex **T** is seen as a region of deep purple near the outer endwall. The leakage vortex is the location of minimum total pressure recorded in the rotor exit flow. The loss core is around $0.9h$ at this axial location, which matches with what was observed with five hole probe at $0.38c$ and $0.46c$ behind the trailing edge. The leakage vortex is elongated into an elliptic shape, exactly like that seen in the rotating frame. The width of the leakage vortex from the test blade is almost half the width of the passage. The leakage vortex from the neighboring blade, which has a smaller clearance, occupies a smaller region.

Both the inner and outer passage vortices **P** could be seen. The center of the outer passage vortex is about $0.8h$ while that of the inner passage vortex is about $0.4h$. In other words, the inner passage vortex is further away from the inner endwall than the outer passage vortex is from the outer endwall. This is possibly a consequence of the radial flow, which displaces all vortices in a radially outward direction. Also, the loss core of the outer passage vortex is somewhat higher than that found with five hole probe. Hence, one might assume that the outer passage vortex tends to move radially inwards at it convects downstream.

Although not seen in the contouring of Figure 3.7, it could be seen in the subsequent contour plots (Figures 3.9, 3.10) that there is horizontal strip of low p_0 extending across the passage from $0.75h$ to $0.85h$. Total pressure are higher both above and below this horizontal strip. This strip, which occurs in almost every p_0 map done with the Kulite probe, does not show up in the five hole probe maps. Also, no similar strip could be seen near the inner endwall,

although that could be due to the inaccuracy of the data near the inner endwall. As noted in the introduction, the passage vortex crosses the passage from the suction to the pressure side. This strip might be a trail left by the vortex crossing. It is puzzling to note that this trail does not show up in the rotating frame.

Figure 3.8 shows yet another schematic of the leakage flow. This figure shows how an "auxiliary" leakage vortex might be formed, based entirely on the flow topology. The size of this auxiliary leakage vortex could be expected to depend on the size of the leakage vortex. It would be, in general, much smaller than the leakage vortex. So, for tight clearances, when the leakage vortex is weak, the auxiliary vortex might be very hard to detect. Careful examination of the contour plots for larger tip clearances seem to show that this is indeed the case, and the low total pressure zone associated with the leakage vortex is a combination of losses from the leakage vortex as well as the auxiliary vortex.

3.2.2 Dependence of p_0 on Tip Gap Height

The variation of the basic flow features with change in the clearance height is of considerable importance. Tip gap height could easily be varied in the AFTRF by attaching thermoplastic shims of various thicknesses to the blade tip. A total of 5 thicknesses are tested, as shown in Table 3.1. It must be remembered that the error in tip gap measurement is 0.1 mm.

These five cases are shown in Figures 3.9, 3.10 and 3.11. It appears that the tip vortex occupies progressively smaller areas as the gap closes. The difference in the two extreme cases, as shown in Figures 3.7 and 3.11 are marked. There is little difference in the features shown by the pairs in Figures 3.9 and 3.10.

shim size(mm)	**gap(mm)**	**gap(in)**	$(t/h) * 100$
0.000	1.651	0.065	1.34
0.254	1.397	0.055	1.14
0.381	1.270	0.050	1.03
0.508	1.143	0.045	0.93
0.635	1.016	0.040	0.83
0.762	0.889	0.035	0.72

Table 3.1. List of tested tip gap heights

The outer passage vortex seems to gain prominence as the tip vortex becomes smaller. However, even for the tightest clearance, the tip vortex is still much larger than the passage vortex.

The comparison of the leakage vortex from the test blade and that from the neighboring blade shows that the two vortices are similar when the gaps are comparable (Figure 3.10). The leakage vortex from the test blade is smaller than that from the normal blade for the smallest case (Figure 3.11). All of these tends to strengthen the premise that larger clearance gaps produces stronger leakage vortex. It must be noted that a larger clearance gap not only allows larger masses to leak, it also allows larger momentum to be transported towards the suction side, as shown in Figure 3.12. It could be argued that a larger momentum fluid ends up rolling into a larger sized vortex, with a larger amount of kinetic energy trapped inside the vortex. Eventually the large kinetic energy dissipates by turbulent action which leads to large pressure losses.

The outer passage vortices form at exactly the same radial position irrespective of the gap size. This proves an important point that a larger leakage vortex does not “push” the passage vortex radially downwards, as has been claimed in some studies.

Figures 3.13, 3.14 and 3.15 show the influence of tip gap height on exit total pressure measured at six radial positions. Three gap heights are compared, 1.34%, 1.14% and 0.93%. The

first four charts show data above $0.8h$, that is, above the core of the passage vortex. Figure 3.13 plots the total pressure in the leakage vortex region. The two subplots are almost identical, and show how the minimum pressure point inside the leakage vortex varies with the gap height. The variation in a gap height difference of $t/h = 0.4$ is $p_0/p_{in} = 0.002$. The minimum point seems to shift towards the pressure side as the gap is closed. This is an important point, for it would indicate that the smaller leakage vortices form closer to the suction surface than larger ones. It might also mean that the higher momentum that characterizes the leakage vortex coming out the larger gap penetrated deeper into the passage flow before it rolls into a vortex. It should also be noted that changing the tip gap also changes the shape of the pressure curve between $\theta/\theta_{pass} = 0.5$ and 1.5. This part corresponds to the passage flow on the suction side of the test blade. These plots also show the repeatability of the data on the neighboring blades.

Figure 3.14 shows the pressure plots in the interaction zone: this is where the passage and the leakage vortices interact. Figure 3.14-(a) is in the top portion of this interaction zone and is quite similar to the plots in Figure 3.13. The wakes in Figure 3.14-(b) are shallower, for both the test blade and the neighboring blades. The bottom of the wake in this plot corresponds to the passage vortex, not the leakage vortex, and as it has been noted earlier, the passage vortex is shallower than the leakage vortex. It is puzzling to see that minimum loss point in the passage vortex from the test blade changes with gap height. One would normally assume that the passage vortex loss characteristics would be quite independent of the leakage vortex. Possible, here is an evidence of the interaction of the two vortices. Two scenarios are possible. The passage vortex might entrain some of the low energy fluid from the leakage vortex and thus show up as a lower total pressure zone. Alternately, one might assume that the larger amount of unsteadiness in the larger leakage vortex introduces more losses inside the passage vortex.

While changes in gap height certainly modify the passage flow on the suction side of the test blade, the flow on the pressure side passage is largely unaffected.

Figure 3.15 shows the stage exit total pressure profiles obtained at an approximate mid-span position (57.41% span) for three different tip clearances of the test blade. The wake of the test blade and normal blades are almost identical. Any flow modification that the leakage vortex brings about is localized in the outer part of the passage flow. Passage flow at the mid-span location is not influenced by the leakage vortex.

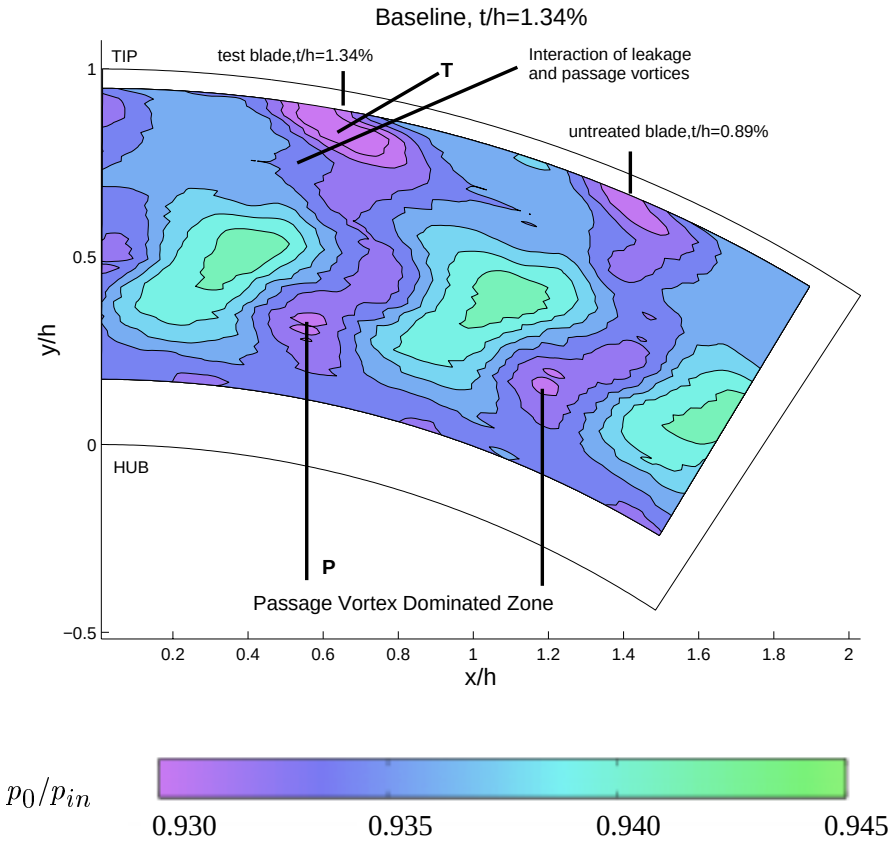

Fig. 3.7. Contours of p_0/p_{in} for baseline case, t/h=1.34%

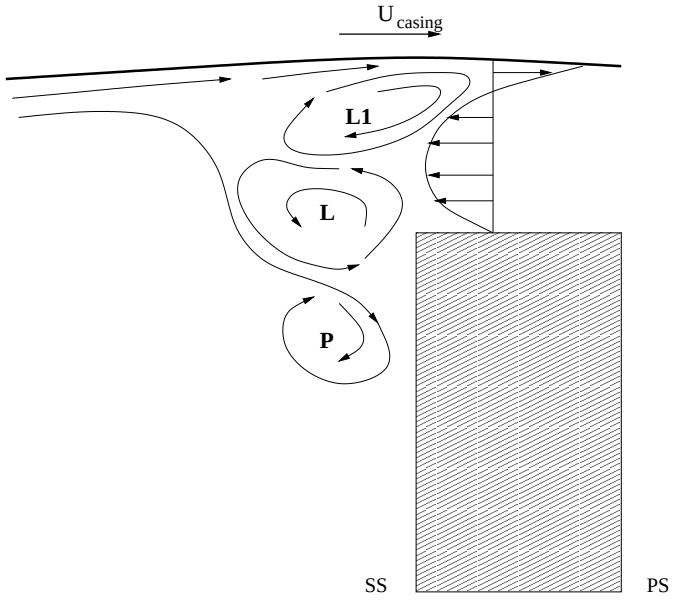

Fig. 3.8. Formation of a auxiliary leakage vortex

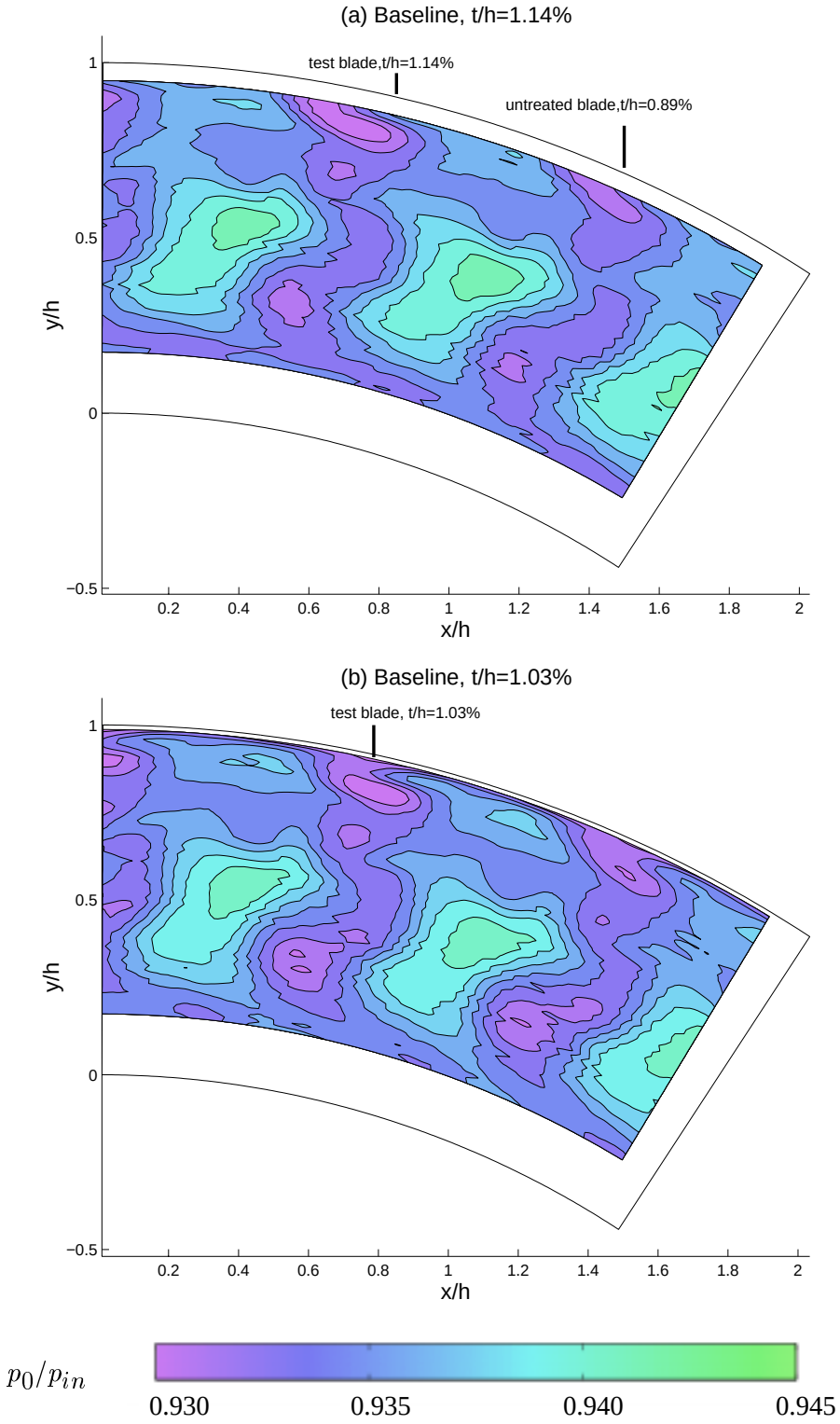

Fig. 3.9. Contours of p_0/p_{in} for baseline case, t/h=1.14% and 1.03%

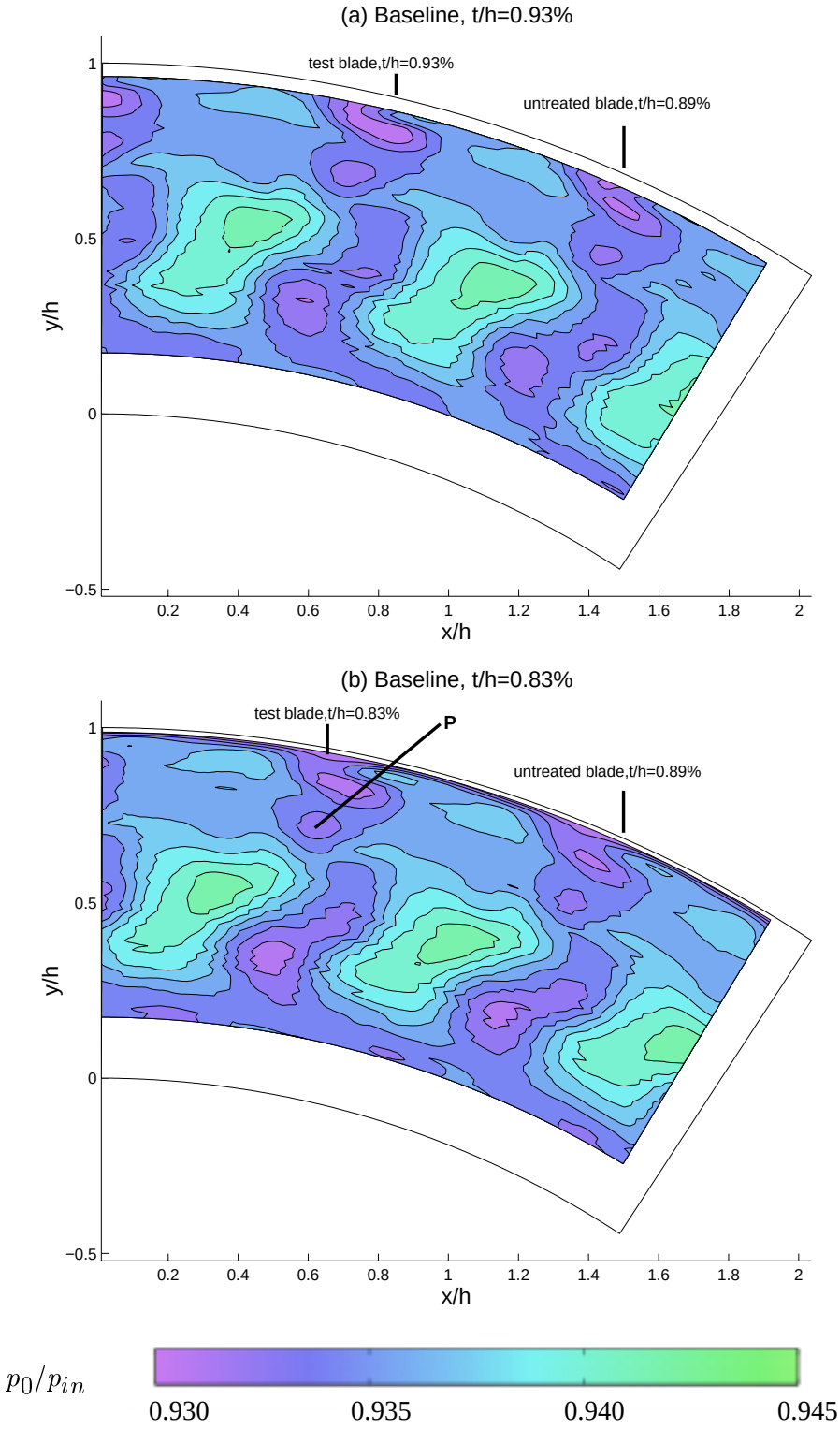

Fig. 3.10. Contours of p_0/p_{in} for baseline case, t/h=0.93% and 0.83%

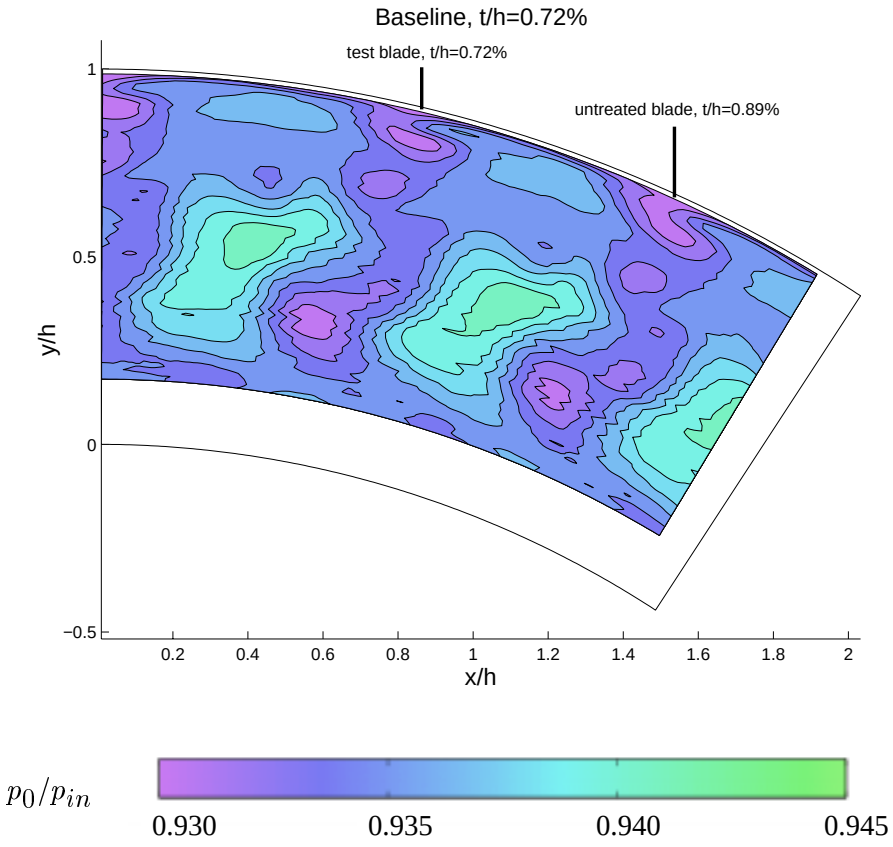

Fig. 3.11. Contours of p_0/p_{in} for baseline case, t/h=0.72%

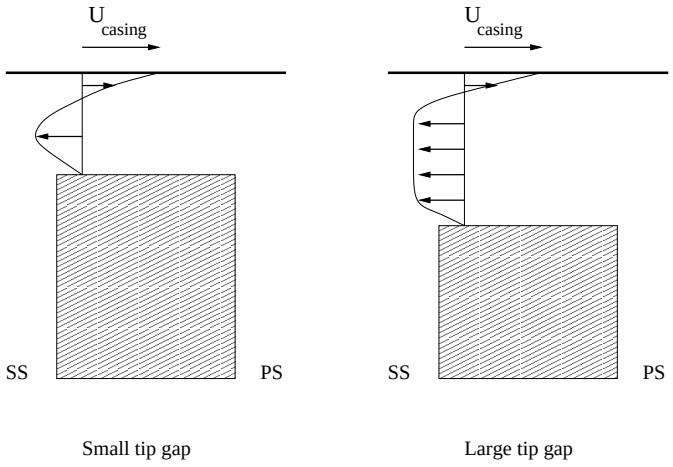

Fig. 3.12. Comparison of small and large tip gap flows

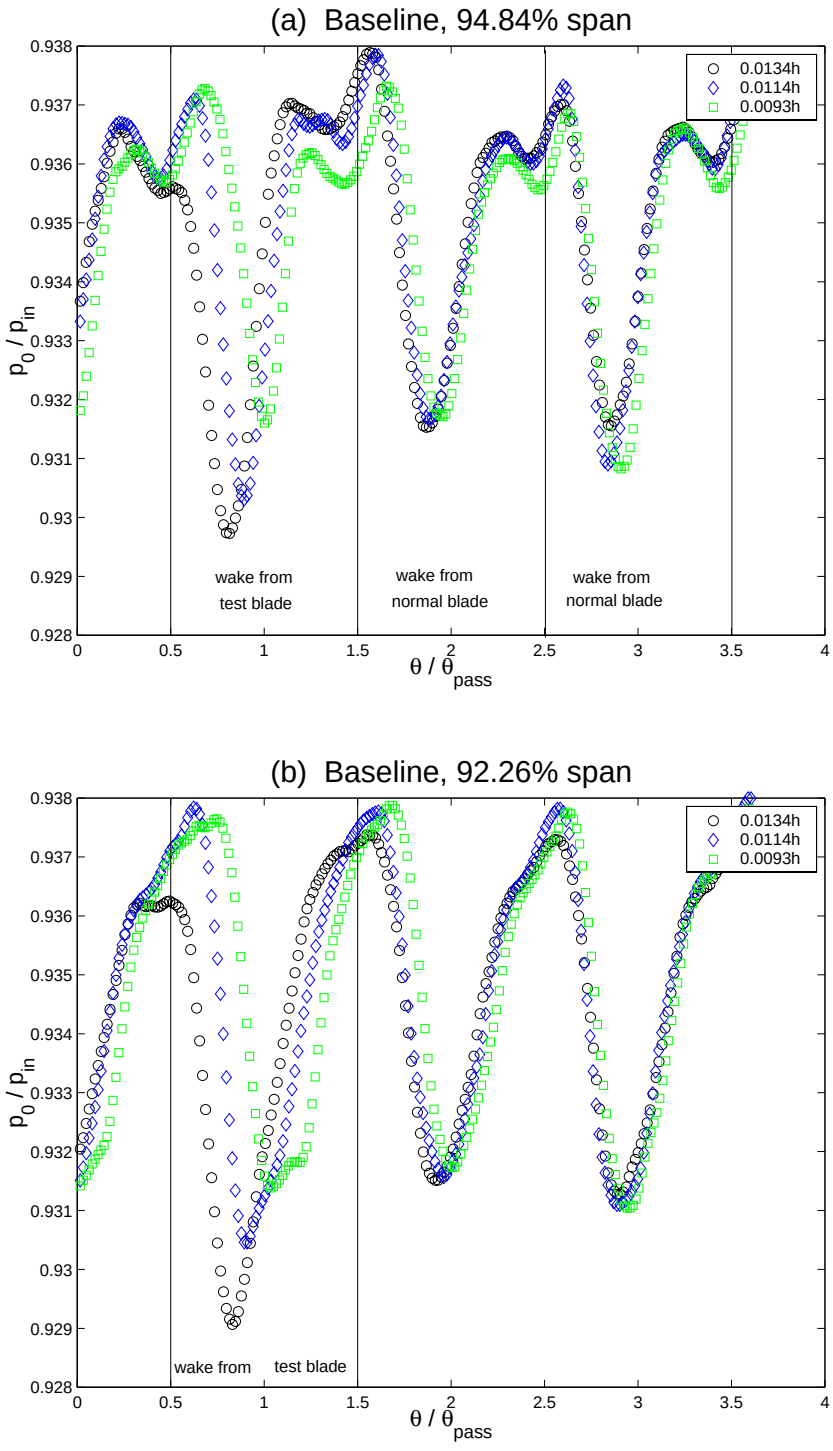

Fig. 3.13. Total pressure deficits due to vortical structures in the blade passage

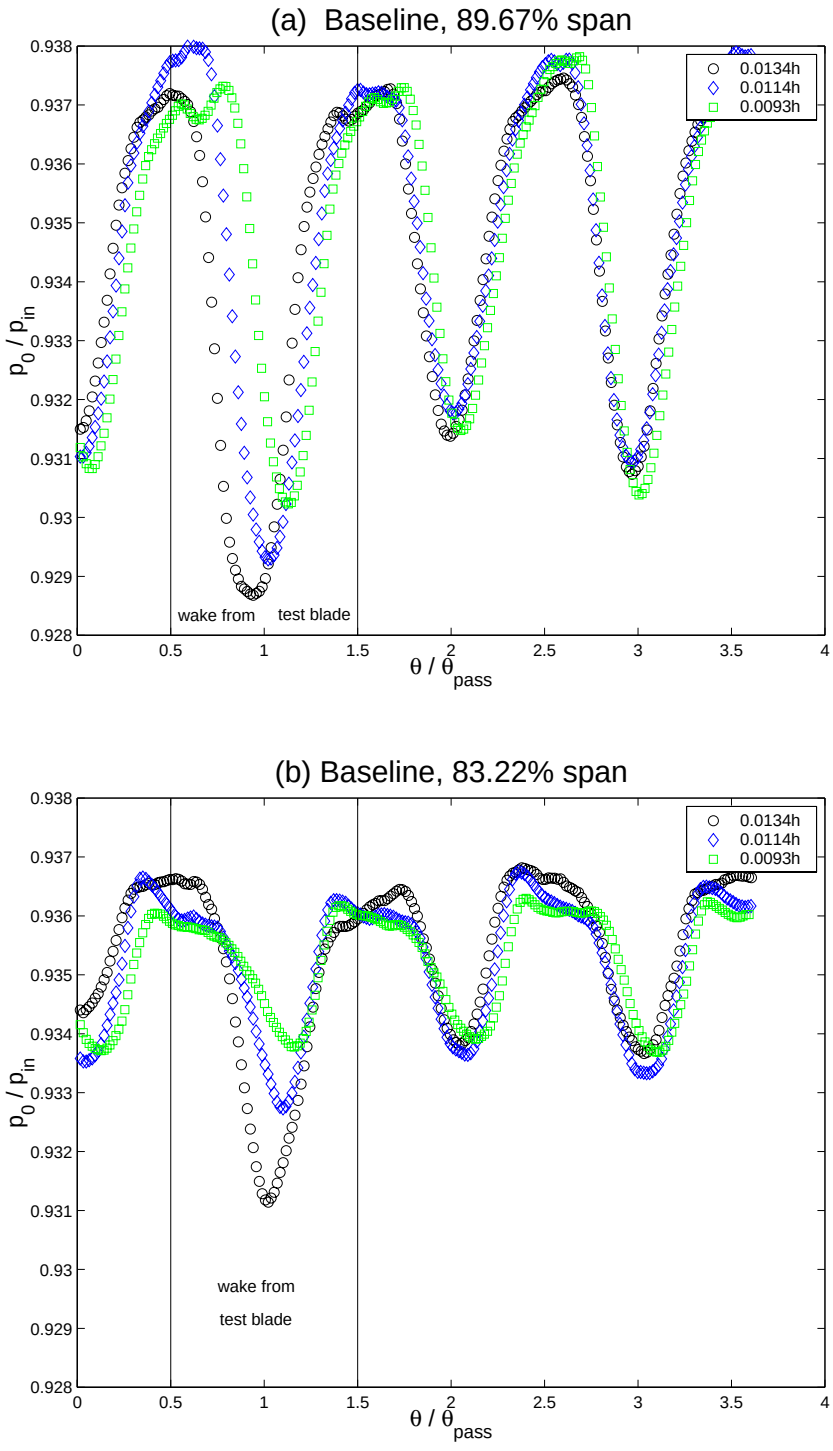

Fig. 3.14. Total pressure deficits due to vortical structures in the blade passage

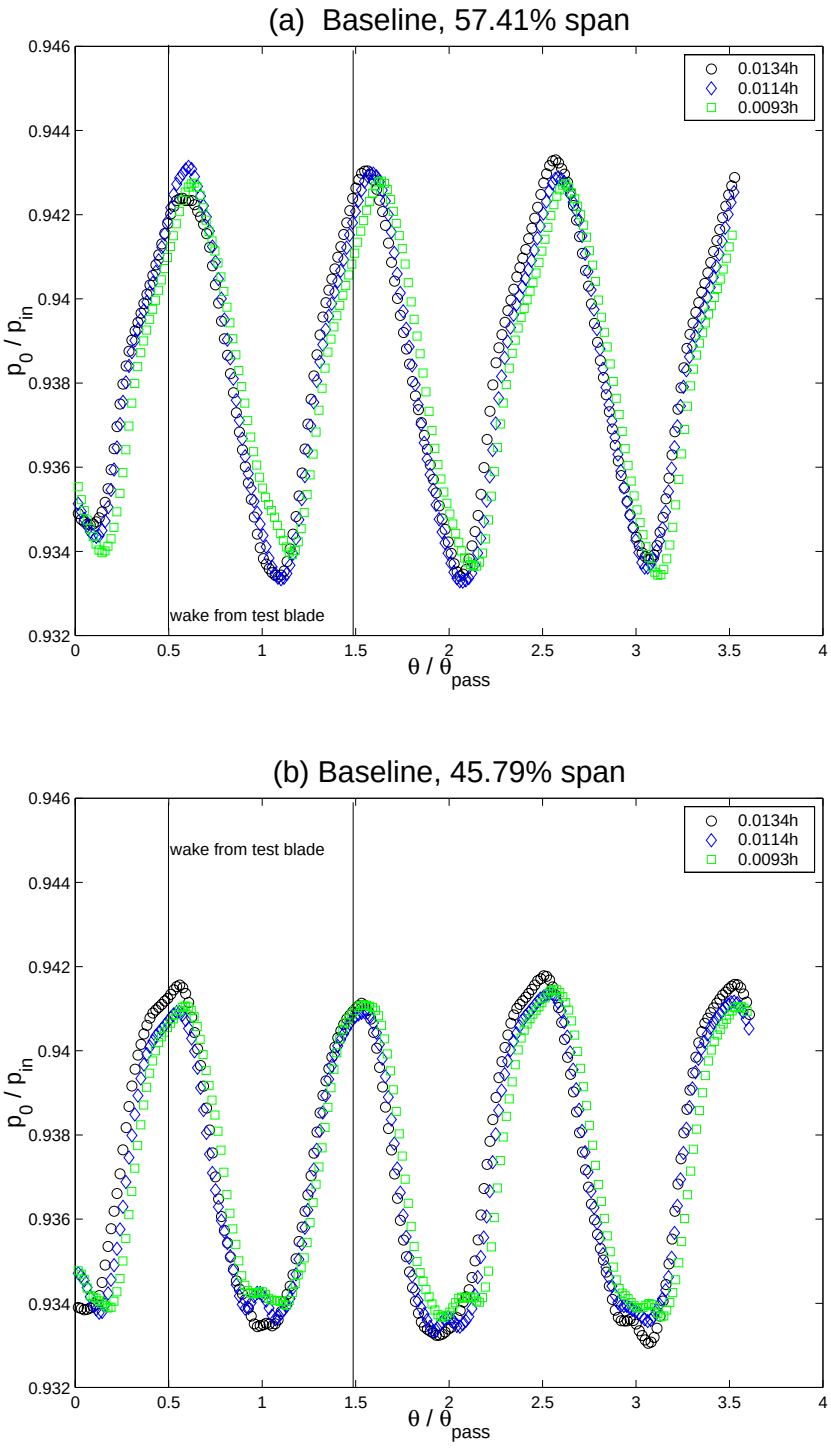

Fig. 3.15. Total pressure deficits due to vortical structures in the blade passage

3.3 Baseline Heat Transfer Measurements

A brief description of the heat transfer efforts made during the study is given in this section. The main purpose of the present effort is to establish a method of measuring heat transfer coefficient on the rotating blade tip. Once the capability of measuring heat transfer is demonstrated, the method could be refined in future to provide valuable information about heat transfer in baseline as well as desensitized rotor blade tips.

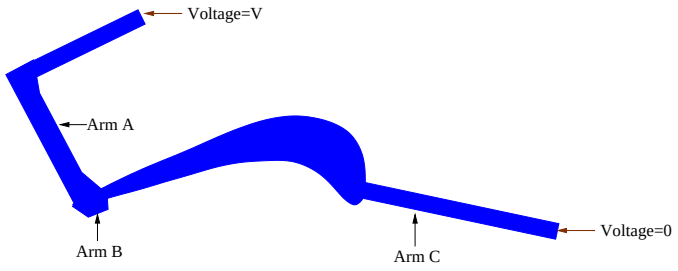

Fig. 3.16. Shape of the Inconel foil used

Figure 3.16 shows how the airfoil surface is heated electrically. The area shown in blue, which includes the airfoil as well as the appendages that carry electrical current in and out of the airfoil, is cut from an Inconel (75% Ni, 15% Cr, 10% Fe) foil. The current carrying Inconel is insulated from the metallic blade surface by double sided tape. Additionally, there is a layer of thermoplastic shim (0.25 mm thick) below the Inconel in the airfoil area, to provide additional insulation in the area of measurement. Only the airfoil is sprayed with liquid crystal, as described in the previous chapter. There were three arms extending the airfoil shape. The arm A near the

trailing edge is connected to the positive terminal on the hub surface by a copper foil conductor. Arm C is connected to the negative terminal, again with a copper foil. Both arms A and C are lying against the suction surface of the rotor blade. In contrast, arm B is not connected to any electrical terminal. It is lying against the pressure surface, providing additional heating area to the thin trailing edge. It was seen that without arm B, the trailing edge got overheated and the Inconel and the underlying insulation in the trailing edge portion of the airfoil got damaged. The resistance of this Inconel strip is 2.0 Ω. The internal electrical connections are wired through the slip ring to a patch panel located outside the rig, from which electrical power is provided with a 20 V, 50 A Hewlett Packard 6261B DC power supply. The additional resistance provided by the electrical path to the Inconel was 1.48 Ω, so the power supply drove current through a total resistance of 3.48Ω. The slip ring was rated for a maximum current of 5 A, so it was possible to apply approximately 17 V potential difference under these conditions. During the tests, the voltage was varied between 12 and 19 V, and hence the current varied between 3.4 to 5.5 A. Hallcrest 42° crystals with 1° bandwidth was used.

Sony DCR VX-2000 3-CCD camera is used to image the heat transfer phenomena. About 2 s of image data was taken and stored in DV format for each of the 8 potential differences applied to the Inconel foil. The IEEE 1394 connection of the camera was used to transfer the images to a PC, where they were converted to 640×480 pixel sized JPEG format images for analysis. The rotor motion was "frozen" with a high power stroboscope actuated by the turbine RPM counter. The position of the stroboscope with respect to the rig was found to be critical in determining the quality of the image.

Figure 3.17 shows the raw image acquired when a 19 V potential is applied. The true colors near the trailing edge of the airfoil are distinctly visible. Eight such images, corresponding to

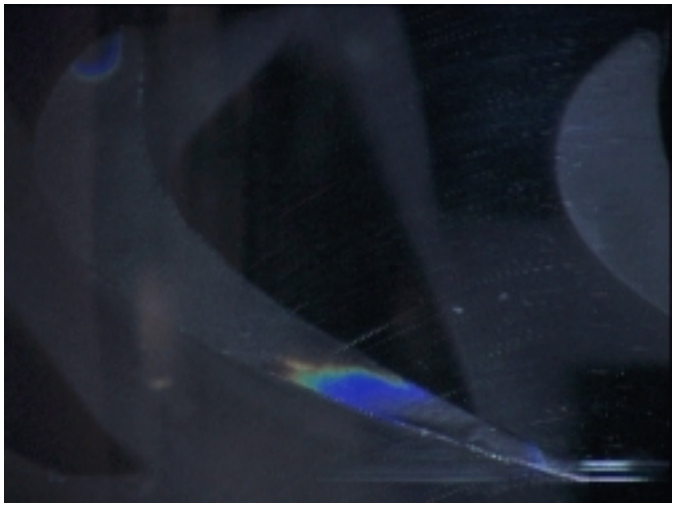

Fig. 3.17. Raw image corresponding to 19 V potential

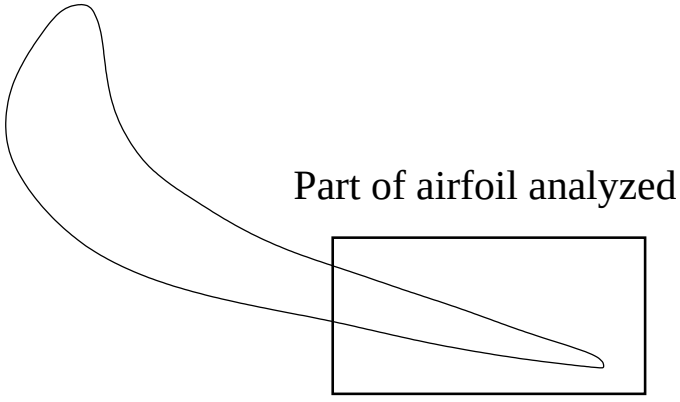

Fig. 3.18. Part of the airfoil analyzed

Fig. 3.19. Color bands for composite image

voltages between 12 V and 19 V, were collected for analysis. The color band seen in Figure 3.17 moves from the trailing edge towards the leading edge as higher and higher potential differences are applied. Potential difference higher than 19 V was not applied due to the 5 A current limitation of the slip ring. Hence, only a portion of the airfoil could be analyzed presently. Figure 3.18 highlights the portion of the airfoil which is examined in this study. Figure 3.19 shows a false color rendering of the combined set of 8 images in the area highlighted by Figure 3.18. Figure 3.19 was produced by the following technique. The MATLAB image processing toolbox was used. Images were read and cropped to the area under analysis. This was an area of 300×170 pixels. The RGB image matrix was converted to HSV matrix to ease calculations. A minimum intensity value $I_{min} = 0.3$ was selected. Pixels whose intensity was less than I_{min} were replaced by black colored pixels. This provided the basic level of filtering, and helped to reduce some of the noise in the original image. The green hue range of $H_g = 170^\circ - 200^\circ$ was chosen as the brightest hue zone (hue values are cited with reference to 360°). This hue zone also provided the sharpest images. Pixels with hue values outside H_g were colored black. Thus only pixels in the H_g hue zone were left colored in the image. This pixels correspond to the 42° C isobar for the applied potential difference across the Inconel strip. To produce the false color image Figure 3.19, the pixels corresponding to each potential were colored with a different hue. Hence a combined set of isobars were produced.

Extensive details about liquid crystal thermography could be found in [6]. The following summarizes the method to calculate heat flux on the Inconel heater foil.

For a two dimensional, linear, isotropic, homogeneous conducting medium with no free charge, the electric potential must satisfy

$$\nabla^2 V(x,y) = 0$$

for all points (x, y) on the heater surface. An electric field vector **E** can be defined as the gradient of the scalar potential field $V(x, y)$ and so

$$\mathbf{E} = -\nabla V(x,y)$$

The current density is then given by

$$\mathbf{J} = \sigma \mathbf{E}$$

where σ is the electric conductivity of the material. For Inconel, $\sigma = 970902(\Omega\text{m})^{-1}$. Finally, the heat generated is given by the dot product

$$\dot{q}_{gen} = \delta \mathbf{E}.\mathbf{J}$$

$\dot{q}_{gen}$ has units of W/m^2, and δ is the thickness of the heater foil, which is 25 μm in the present case. So,

$$\dot{q}_{gen} = \delta\sigma[\nabla V(x,y)]^2$$

Since the gradient operator is a linear operator,

$$\nabla V(x,y) = V'\nabla V_0(x,y)$$

where $\nabla V_0(x, y)$ is the potential distribution when a potential difference of unity is applied, and V' scales it to any voltage desirable. So, one only needs to calculate

$$\dot{q}_{gen0} = \delta\sigma(\nabla V_0(x, y))^2$$

and for any arbitrary potential difference V', $\dot{q}_{gen} = V'\dot{q}_{gen0}$ holds. Hence the problem of finding the generated heat flux reduces to the problem of finding the solution to the Laplace equation $\nabla^2 V(x, y) = 0$ which boundary conditions of $V = 1$ at current entrance terminal and $V = 0$ at current exit.

As explained in the previous chapter, the idea is to obtain the heat transfer coefficient using the equation

$$\dot{q}_{gen} = h(T_s - T_{ref})$$

For each value of the applied potential difference V, one needs to obtain the corresponding $\dot{q}_{gen}$. T_{ref} in the present set of measurements is T_{in}, while $T_s = 42\circ$ C isotherms could be obtained as described above. Now $\dot{q}_{gen} = V\dot{q}_{gen0}$, so the above equation becomes

$$V\dot{q}_{gen0} = h(T_s - T_{ref})$$

or,

$$h = \frac{\dot{q}_{gen0}}{(T_s - T_{ref})}V$$

Now, for the small area analyzed near the trailing edge, $\dot{q}_{gen0}$ could be considered uniform. This means that the isotherms shown in Figure 3.19 are also the contours of h, with a factor of proportionality.

Chapter 4

Flowfield Near a Desensitized Tip

4.1 Coolant Injection into a Tip Trench

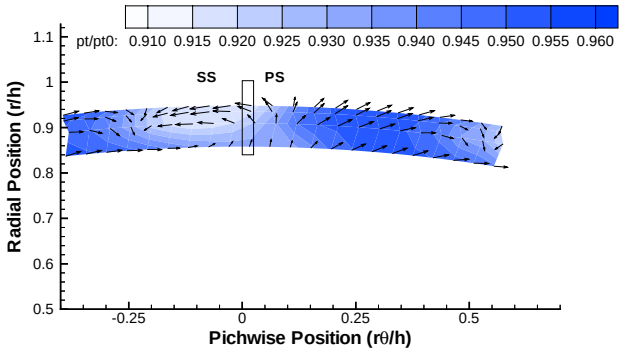

Fig. 4.1. Flowfield at $d = 0.38c$ with cooling, $t/h = 1.4\%$

Coolant injection studies used five hole probe in the rotating frame of reference, as described in the previous chapter. Figure 4.1 shows the area traverse at the $d = 0.38c$ location with cooling turned on. The coolant flow is not expected to have much effect away from the tip, and the velocity vectors from 90% span downwards seem to be identical to the no-cooling case, as shown in Figure 3.1. It could be assumed that the passage vortex is unaffected by the cooling flow. The recirculation seen in Figure 4.1 is somewhat less severe compared to the baseline case.

The leakage vortex seems to be slightly elongated in the pitch-wise direction. The loss contour seems to be a shallower by 0.5%. It is possible that a shallower loss core is occupying a larger area, and the area averaged total loss may still be the same as the uncooled case.

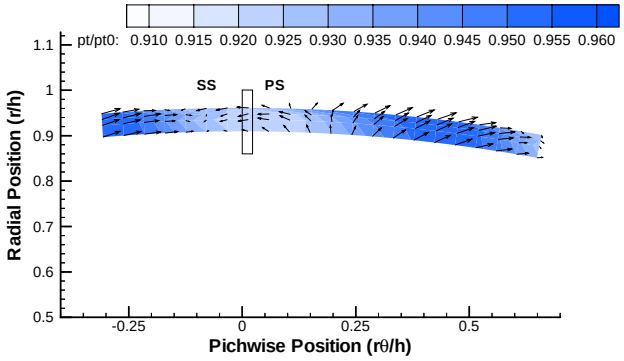

Fig. 4.2. Flowfield at $d = 0.46c$ with cooling, $t/h = 1.4\%$

Figure 4.2 shows the flow-field at $d = 0.46c$ with cooling on. The flowfield is similar to the one at $d = 0.38c$.

Figure 4.3 and 4.4 show the pitch averaged yaw angles at various radial locations. The findings support the above observation that the cooling flow does not alter the overall characteristics of the three dimensional mean flow measured downstream of the rotor.

So, coolant injection at low mass flow rate (equivalent mass flow rate is 0.3% of the turbine mass flow) makes only slight changes to the flowfield, and does not contribute to desensitization. Aggressive coolant injection from the blade tip may be effective in performing better aerodynamic desensitization.

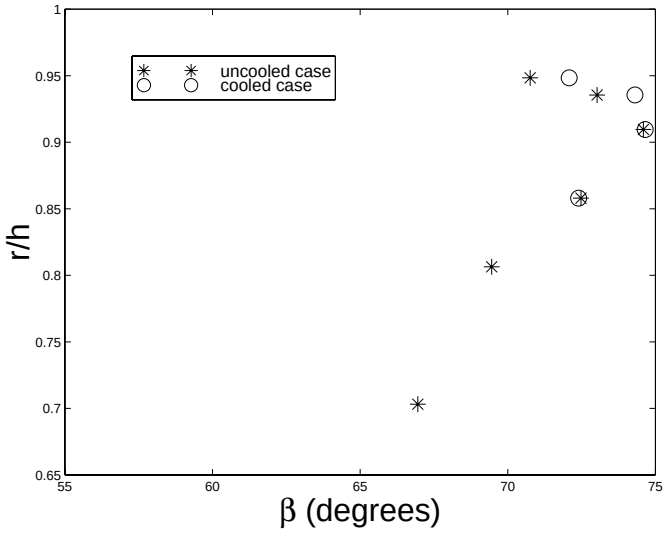

Fig. 4.3. Yaw Angle β distribution in radial direction at $d = 0.38c$

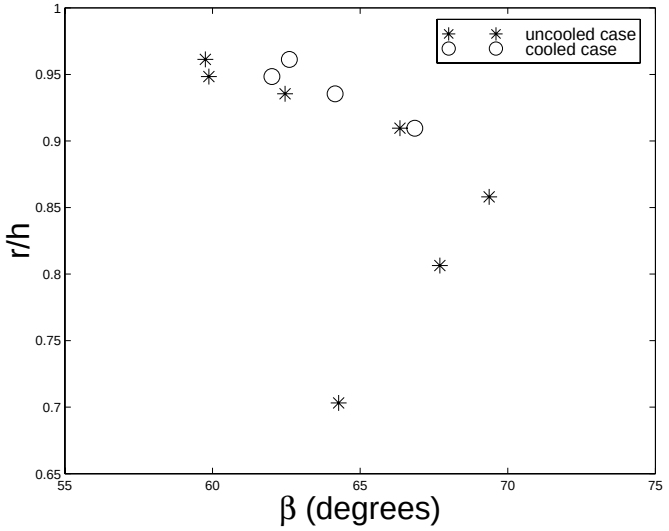

Fig. 4.4. Yaw Angle β distribution in radial direction at $d = 0.46c$

4.2 Tip Platform Extension Method

4.2.1 Suction Side Tip Platform Extensions

Two different suction side extensions are tested, as shown in Figure 2.10. These configurations are referred to as SS-1 and SS-2. Figure 4.5 shows the contour plots of stage exit total pressure from each of the two. The tip gap height is kept at t/h=1.14% for the test blade. The configuration SS-1 has a suction side extension preserving the wedge angle of the original tip trailing edge profile. SS-2 has a tip platform extending all the way to the trailing edge point. In other words, SS-2 has a wider trailing edge than SS-1. The idea behind these two designs was to investigate the effects of the trailing edge platform thickness on the rotor exit pressure losses.

Figures 4.5 needs to be compared with Figures 3.9-(a), since both of them have a clearance of t/h=1.14%. It would appear the suction side extensions manage to displace the leakage vortices to the left, or towards the pressure side of the adjacent blade. The suction side platform guides the leakage jet in such a way that the tip leakage fluid rolls into a tip vortex at a location slightly away from the corner formed by the tip and outer endwall. Other than that, there is very little difference between the normal and the desensitized cases. Also, there is little difference between SS-1 and SS-2, or, in other words, the trailing edge platform thickness does not seem to affect the total pressure field at this axial location. One might explain the findings in observing that tip platform extensions on the suction side does not provide any modification to the entrance conditions of the leakage flow starting from the pressure side corner, that is, the same amount of mass enters the tip gap.

This set of tests suggest that interfering with tip leakage fluid after it is already entered the tip gap region is not an effective desensitization strategy. It is essential to reduce the mass

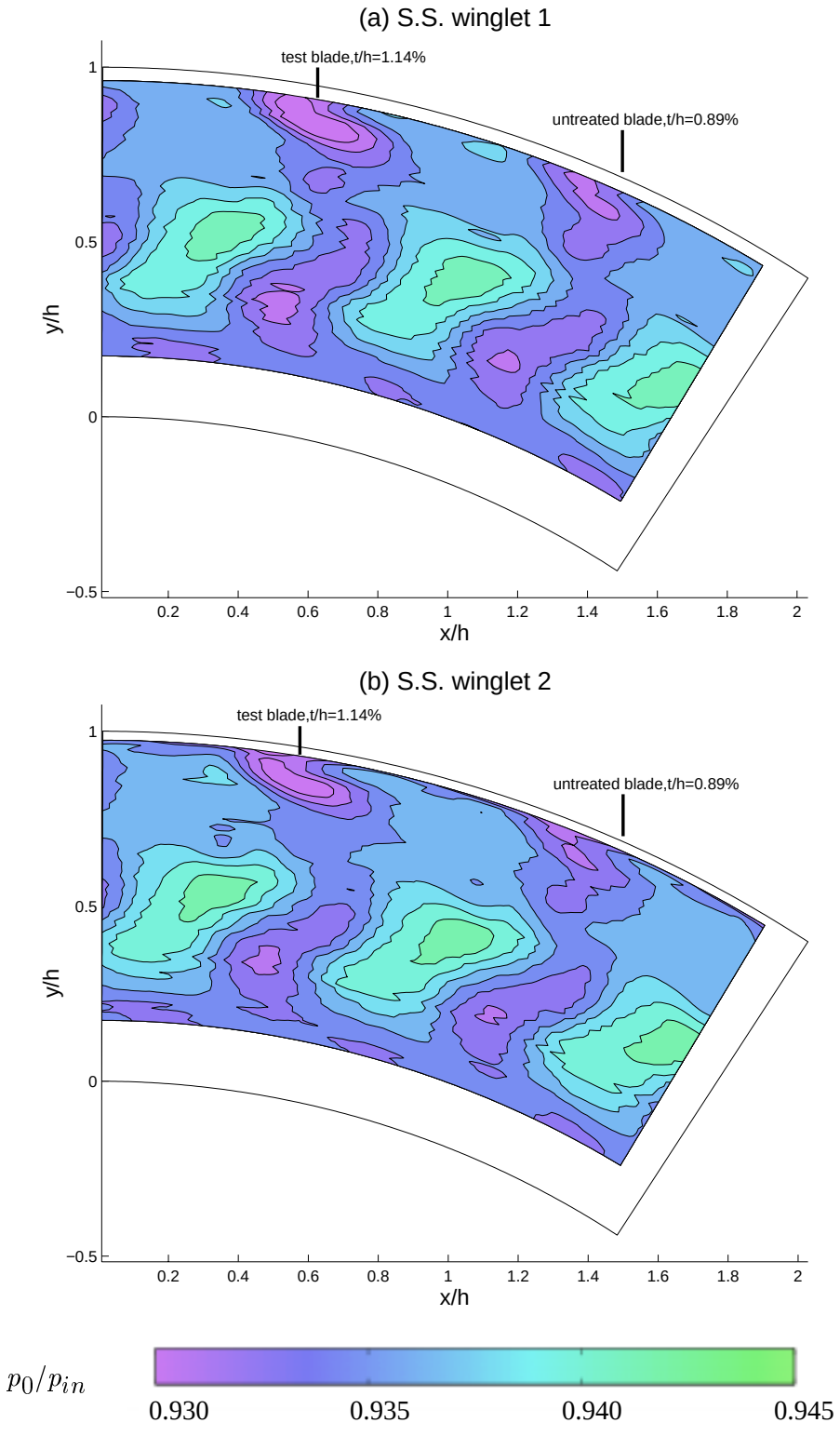

Fig. 4.5. Contours of p_0/p_{in} for the suction-side tip platform extensions, t/h = 1.14%

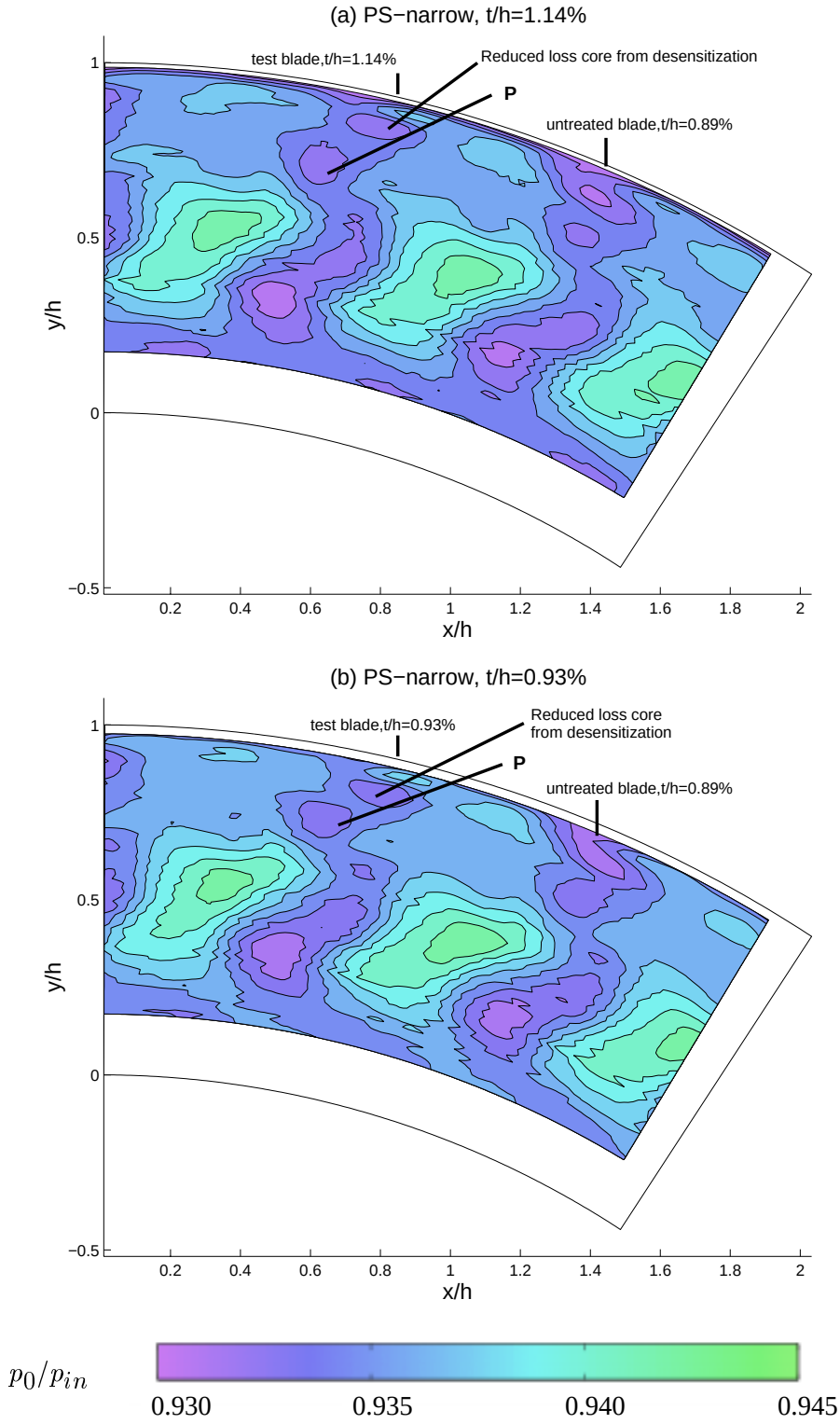

Fig. 4.6. Contours of p_0/p_{in} for the PS-narrow cases, t/h = 1.14% and 0.93%

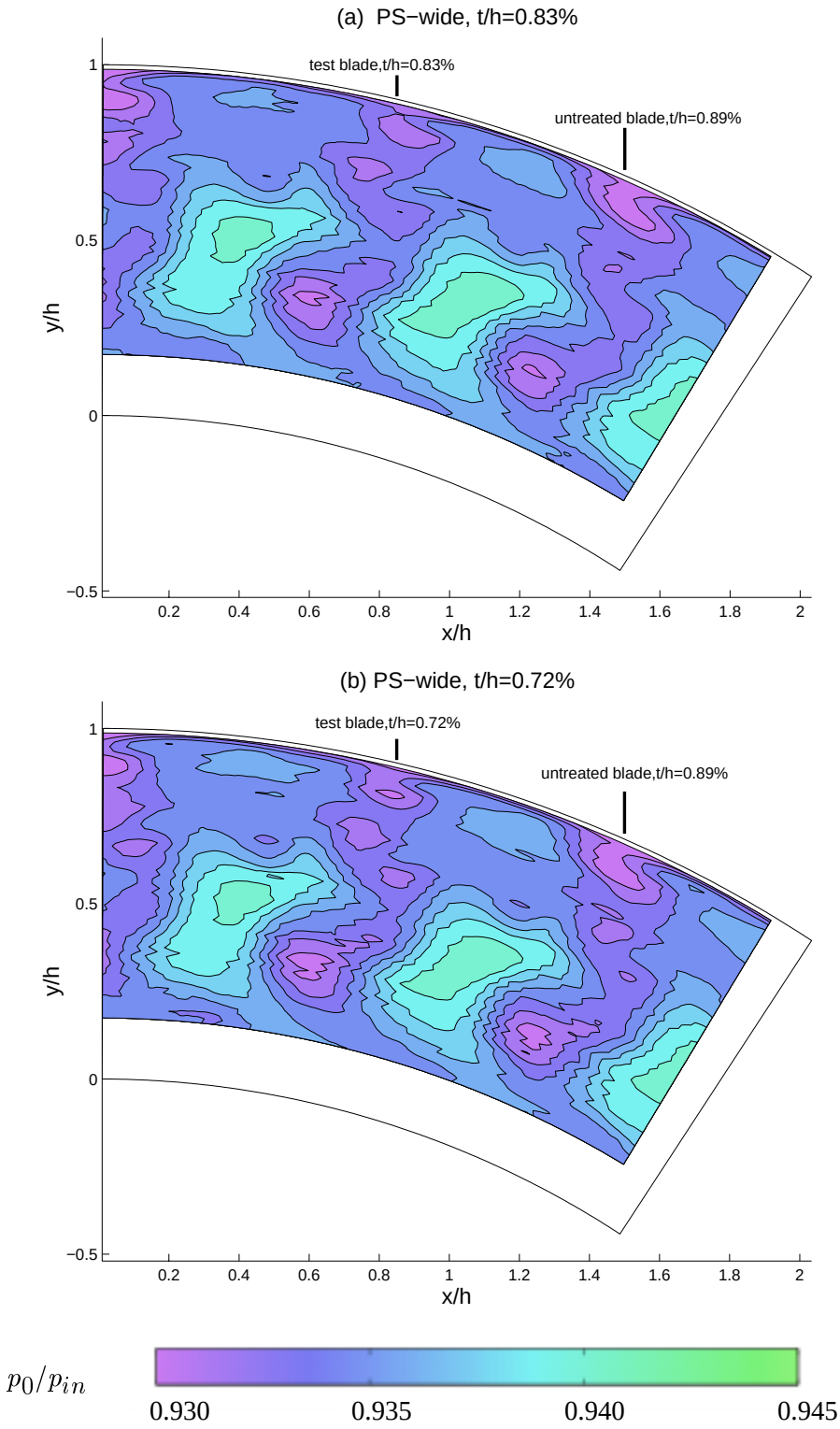

Fig. 4.7. Contours of p_0/p_{in} for the PS-wide cases, t/h = 0.83% and 0.72%

flow rate of mainstream air entering into the tip gap near the pressure side corner of the tip. It should be remembered, though, that the amount of mass entering the gap is mainly determined by the pressure difference across the blade. A desensitization strategy on the suction side that reduces the pressure difference at the tip would possibly be quite effective. However, the specific geometry that was tested at AFTFR certainly did not make any difference.

4.2.2 Pressure Side Tip Platform Extensions

A narrow and a wide tip platform extension on the pressure side is evaluated as a possible tip desensitization configuration. The geometrical details of the specific tip platforms are described in Figure 2.9. A few different tip gap sizes were tested. The idea of extending the tip platform near the pressure side corner of the tip is related to that of reducing the tip leakage mass flow rate by adversely affecting the entrance flow conditions into the gap region from the pressure side of the rotating blade tip. This method of weakening the tip vortex structure is attractive because there is a possibility of reducing the mass flow that could enter the clearance gap.

The results from the narrow pressure side extension with two different tip gap heights (t/h=1.14% and 0.93%) are shown in Figure 4.6. These figures are to be compared to Figures 3.9-(a) and 3.10-(a) in order to note differences from a non-desensitized case. It is obvious that the strength of the tip vortex is greatly reduced by using a narrow pressure side tip platform extension. The vortex core documented for the baseline case, shown in the last chapter, is clearly smaller for both t/h=1.14% and 0.93%. The region marked as **P** in Figure 4.6 shows the outer passage vortex dominated zones. The passage vortices seem to remain unchanged as the tip gap closes. Changes could be noticed in the leakage vortex dominated areas in between Figure 4.6-(a) and Figure 4.6-(b). The vortex weakens as the tip gap closes, as might be expected.

Figure 4.11 shows the combined effect of pressure side tip platform extension and a narrow tip gap of t/h = 0.72%. The leakage vortex is hard to distinguish. This is possible because the little mass flow that this tip gap would have admitted is mostly blocked off by the tip platform extension. Consequently, the passage vortex seems to be the dominating loss region in this figure. The leakage vortex surely forms, but the magnitude of the pressure loss it contributes to is vastly reduced.

Figure 4.6 shows that the minimum total pressure measured at the exit of the turbine stage is still located at the core of the tip leakage vortex, in spite of the desensitization treatment. This observation was confirmed experimentally in each of the 29 rotor passages mapped. Figure 4.12 presents the minimum total pressure value as a function of the tip gap height for the case of the baseline tip, pressure side narrow tip extension and the first suction side tip extension (SS-1). The minimum value of local total pressure at the rotor exit varies linearly with tip gap height with no tip desensitization (open squares). The curve defining the minimum total pressure value with a narrow pressure side extension (diamond symbols) shows a significant improvement in terms of exit local pressure. The minimum total pressure generated by the suction side tip extension SS-1 at a tip gap of t/h=1.14% shows slightly less exit total pressure compared to the baseline tip with no treatment.

Figure 4.7 shows the contour plots from the two PS-wide extensions. The pressure side extensions for this case use a w dimension of 6.35 mm as described in Figure 2.9. The second figure in the set shows the tightest clearance tested, $t/h = 0.72\%$. The small clearance, along with the tip treatment, made the tip vortex difficult to distinguish. A more quantitative comparison is shown in Figure 4.10 when measured total pressure distributions are compared at selected radial positions. This figure compares the “wide pressure side extension” against the

"baseline" tip that has no desensitization. From this figure, and from Figure 4.7, it would appear that the wider pressure side extension when combined with the tighter clearance of t/h=0.72% has the ability to weaken the tip vortex structure significantly. Overall, the performance of the narrow and the wide tip platform extensions that were tested are very similar. This probably means that increasing the parameter w in Figure 2.9 slightly does not block mass flow into the tip gap any further. Further extension of the pressure side platform may result in additional aerodynamic benefit. The platform could not be extended any further in AFTFR due to mechanical limitations.

4.2.3 Comparison of Pressure and Suction Side Extensions

Figure 4.8 and 4.9 show the stage exit total pressure distributions for three different desensitization schemes in addition to the baseline case without any tip desensitization. The tip clearance value of t/h=1.14% is the same for all four tip configurations. It is noted that no pressure side wide extension is included in these set of figures as the wider extensions were not tested with the tip clearance value of t/h=1.14%. The total pressure distributions in the wake of the test blade and two neighboring blades at four radial positions near the tip are presented (r/h=94.84%, 92.26%, 89.67% and 83.22%). The baseline case shown in Figure 4.8 by open circular symbols serves as reference in deciding the most effective tip desensitization scheme. With any successful tip desensitization effort, the recovered local total pressure at the exit of the stage needs to be elevated in the region containing the fluid coming from near the suction side corner of the blade tip. A desensitization scheme that is not providing an aerodynamic gain is supposed to result in local total pressure values that are less than the baseline measurement, as shown by open circular symbols in Figure 4.8. The flow modifications achieved by the two

suction side desensitizations (SS-1 and SS-2) are shown by green square and red triangular symbols, respectively. It is clear that the suction side extensions do not provide any aerodynamic gain over the baseline case. The narrow pressure side tip extension appears to be the most effective desensitization scheme.

4.2.4 Flow mechanisms Near Tip Platforms

Figure 4.13 attempts to present possible flow mechanism that makes the pressure side extension an effective tip desensitization scheme. The extended platform interacts with the passage flow in the rotor tip region where the driving pressure differential is significant. It is likely that the viscous losses in the gap itself is increased with the platform extension present. The separated flow zone $b1$ is now located on the entrance section of the tip platform. It is also likely that some of the passage flow moving in a radially outward direction at the pressure side corner meets the fluid particles that are trying to enter into the tip gap zone. This flow, when combined with the shearing effect of the outer casing may create unfavorable conditions in terms of the mass flow rate of the leakage flow entering into the tip gap channel. Hence, the existence of a pressure side extension tends to lower the mass flow of the leakage system near the tip of the blade. Due to a significant reduction in the tip leakage mass flow rate, the tip vortex formation occurring on the suction side of the blade is weakened. Inside the leakage vortex, the mean secondary kinetic energy is less when the leakage mass flow is reduced. The dissipation of mean kinetic energy into heat is also reduced. This leads to less entropy generation, which shows up a reduced vortex cores in total pressure maps.

To what extent the extended platform modifies the static pressure distribution is not known. The loading at the tip region is most likely changed from the loading of a blade with

untreated tip. Most of the static pressure changes are expected to be confined to the pressure side as no modifications are made on the suction side. It is possible at the extension reduces the pressure difference across the blade. This has two effects. The total blade loading is now obviously lower with the extension present. However, the mass that exits on the suction side carries less momentum in it, due to the reduced pressure difference, and this is bound to reduce the level of vorticity in the leakage vortex, which in turn ultimately leads to lower pressure losses. The effects of desensitization on the overall efficiency would be dealt with in a later section.

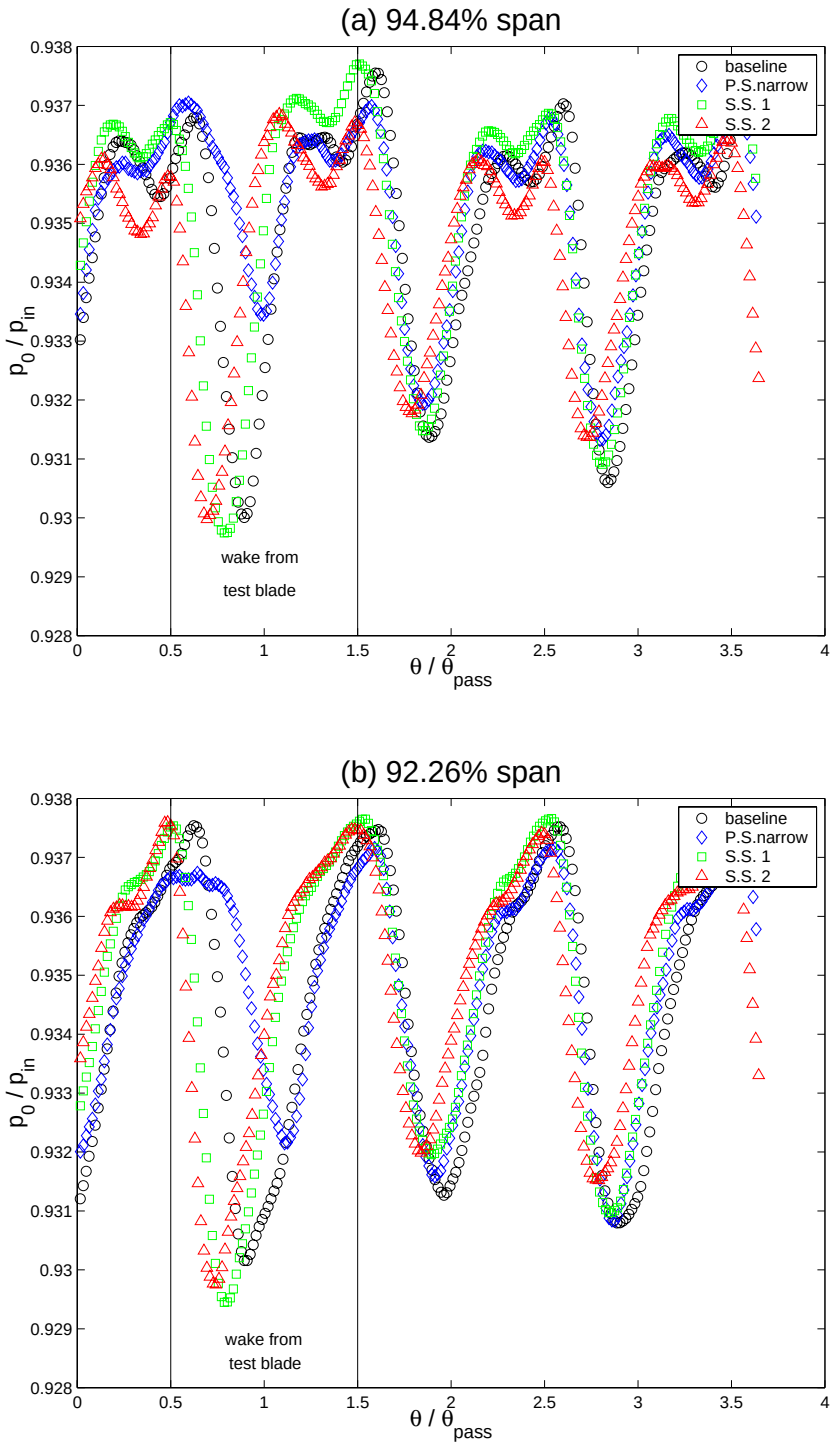

Fig. 4.8. Aerodynamic comparison of PS-narrow and SS tip platform extensions against the baseline configuration, t/h=1.14%

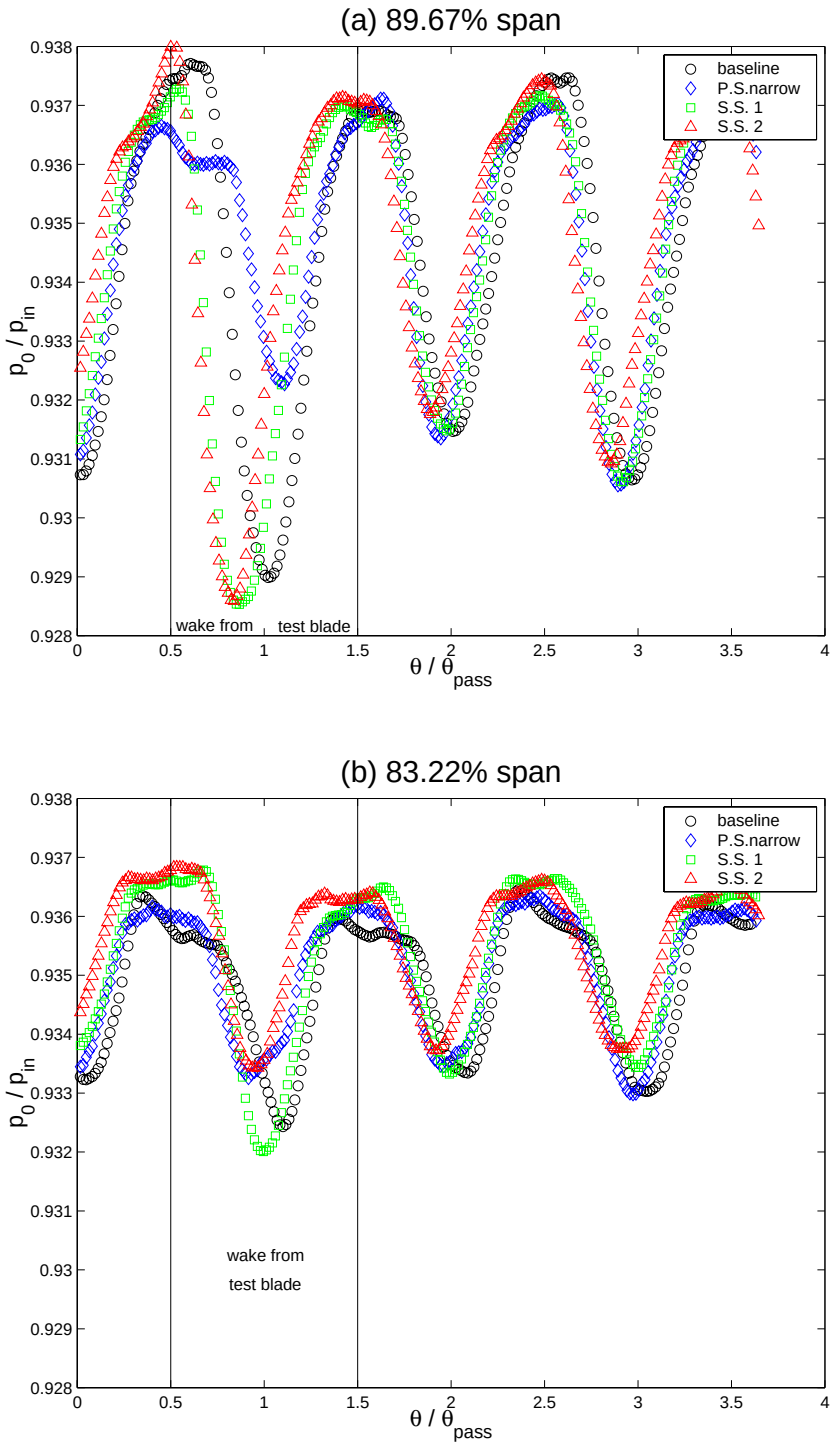

Fig. 4.9. Aerodynamic comparison of PS-narrow and SS tip platform extensions against the baseline configuration, t/h=1.14%

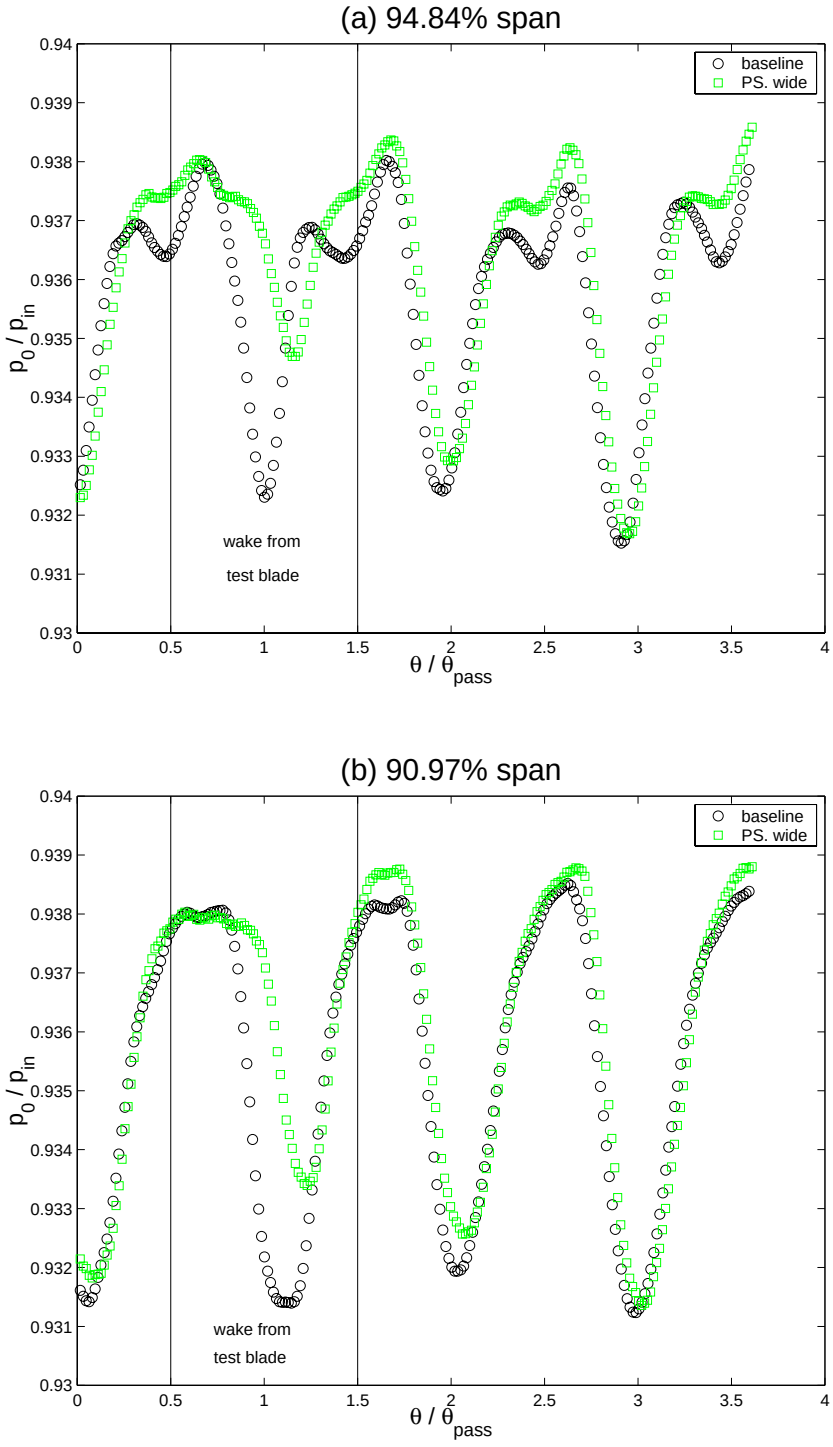

Fig. 4.10. Wake plots of p_0/p_{in} for baseline and PS-wide cases, t/h = 0.83%

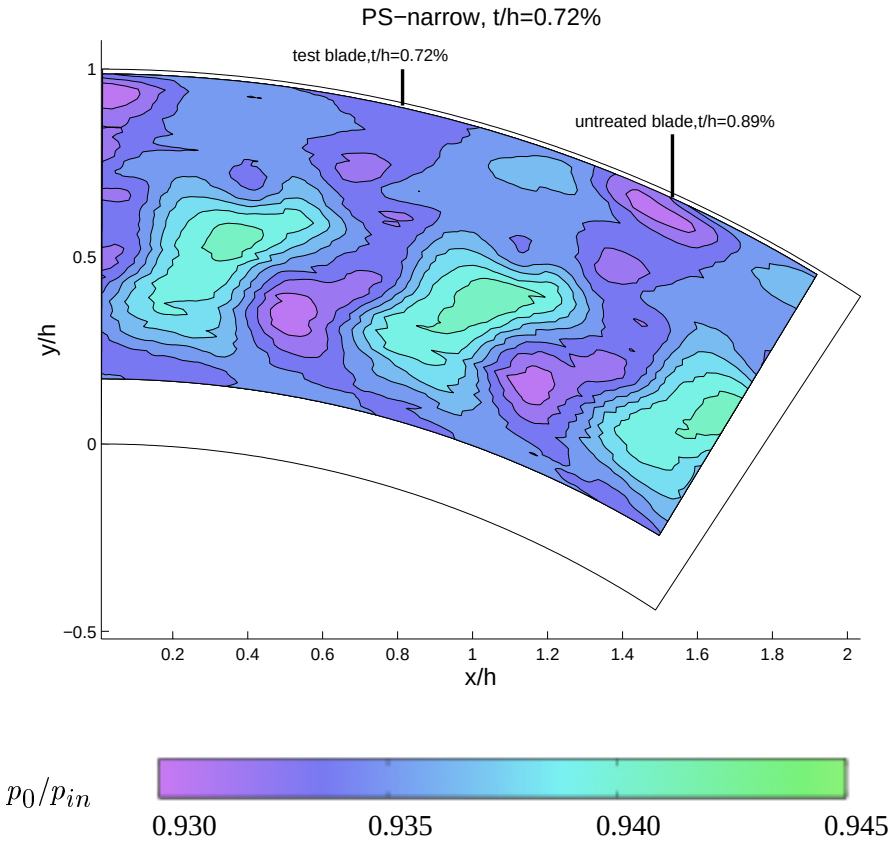

Fig. 4.11. Contours of p_0/p_{in} for the PS-narrow case, t/h = 0.72%

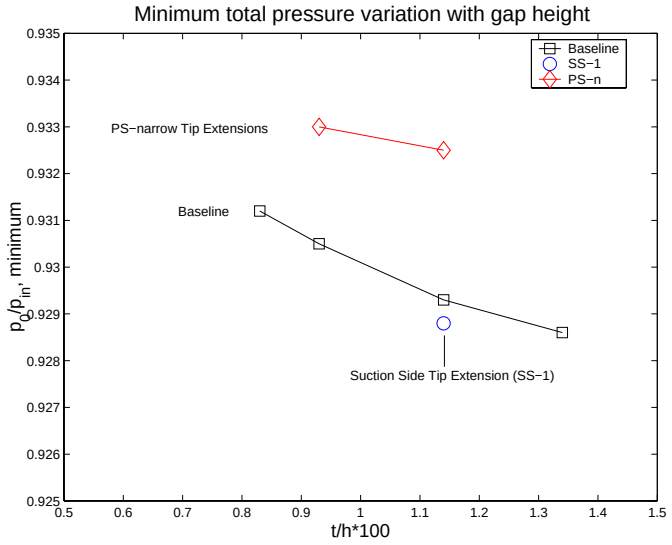

Fig. 4.12. Minimum total pressure versus tip gap height (PS-narrow, Baseline and SS-1)

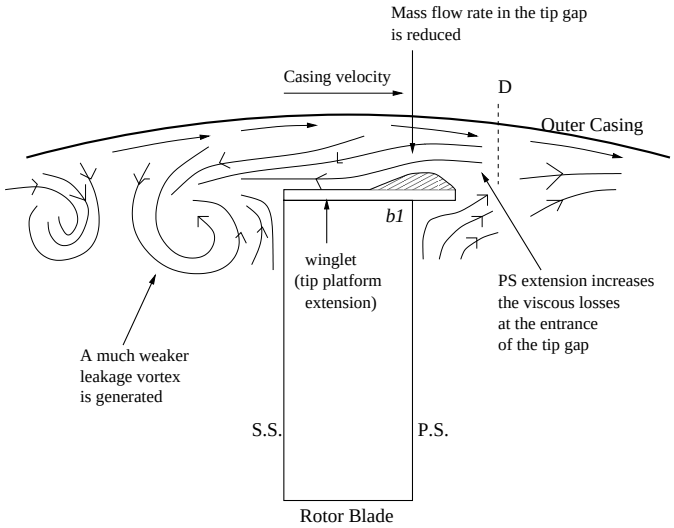

Fig. 4.13. Possible flow mechanisms for pressure side extensions

4.3 Partial Squealer

4.3.1 Suction-side Partial Squealer

Figures 4.14, 4.15 and 4.16 show results from the partial squealer experiments with the squealer rim on the suction side (configurations SSSqA,B,C). The geometry of these squealer configurations are shown in Figure 2.11. These total pressure (p_0/p_{in}) maps are made at $d = 0.3c$ downstream of the rotor trailing edge, and shows, as before, the wake from the test blade and the neighboring normal blade. The geometry and the contouring scheme in this set is identical to the contours plotted for the tip platform extension configurations to facilitate comparison. The top sub-plot in each figure of this set shows the total pressure map from a partial squealer rim that rises $s = 0.38$ mm from the tip surface, while the lower sub-plot features a rim that is twice as thick ($s = 0.76$ mm). The part of the blade surface that is not covered by the partial squealer has the normal tip clearance of 1.65 mm ($t/h = 1.34\%$). So the clearance gap on top of the squealer rim in the top sub-plots is 1.27 mm ($t/h = 1.03\%$) and it is 0.89 mm ($t/h = 0.72\%$) for the lower sub-plots.

From the contour plots, there seem to be little difference between the three configurations for the same gap clearance height. There is, however, significant differences between the two clearance heights. The 0.38 mm rim hardly does any desensitization at all, while the 0.76 mm rim is quite effective in reducing both the size and the depth of the loss core due to the leakage vortex. If 0.38 mm rim case is compared with the baseline case shown in Figure 3.9-(a), which shows at baseline tip surface with a clearance of ($t/h = 1.03\%$), little difference could be noticed. So, there is little difference between a rim with a clearance of ($t/h = 1.03\%$) and a tip surface with a clearance of ($t/h = 1.03\%$). This is, however, not the case with the 0.76 mm rim. Comparing

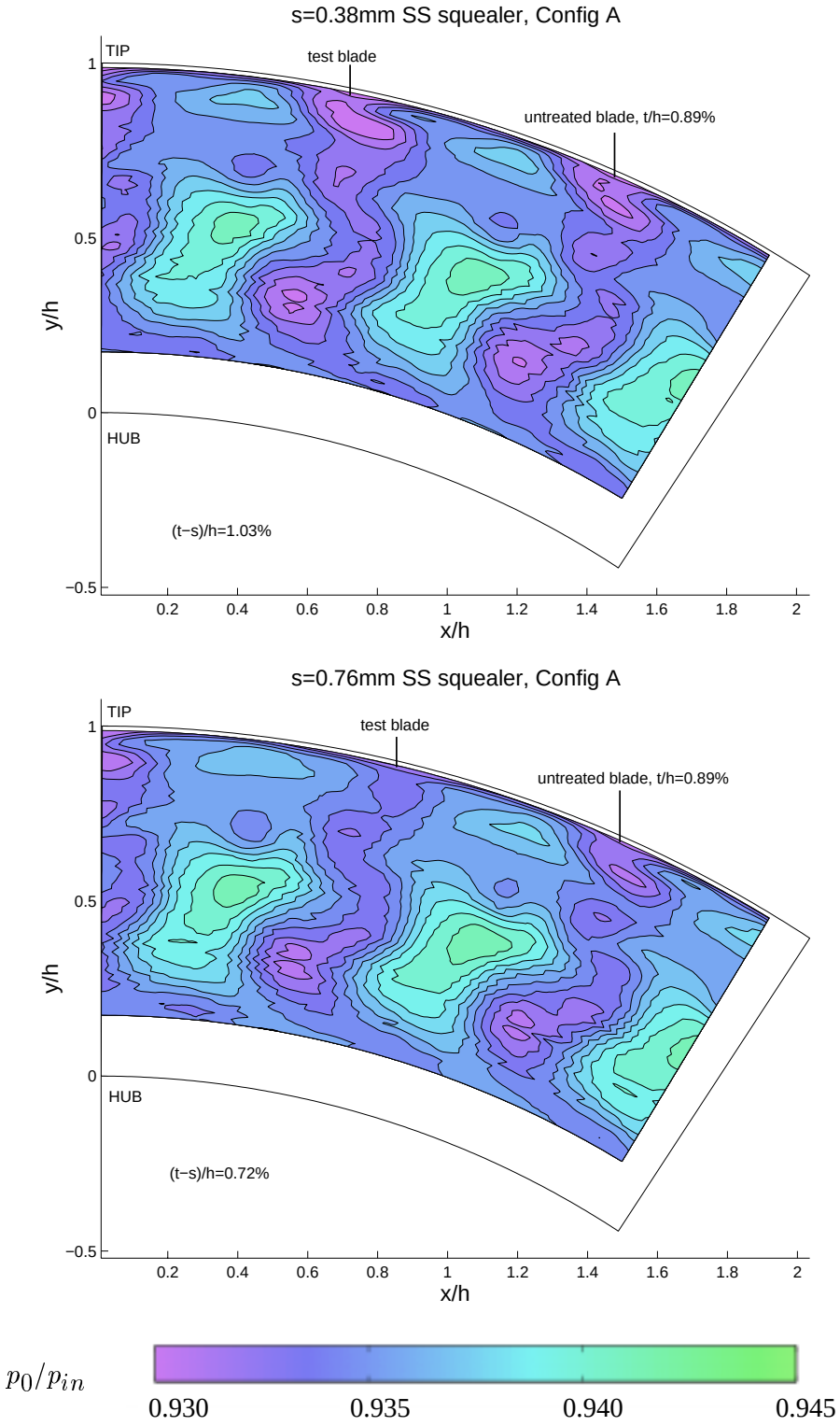

Fig. 4.14. Contours of p_0/p_{in} for SSSq-A, $t/h = 1.03\%$ and 0.72%

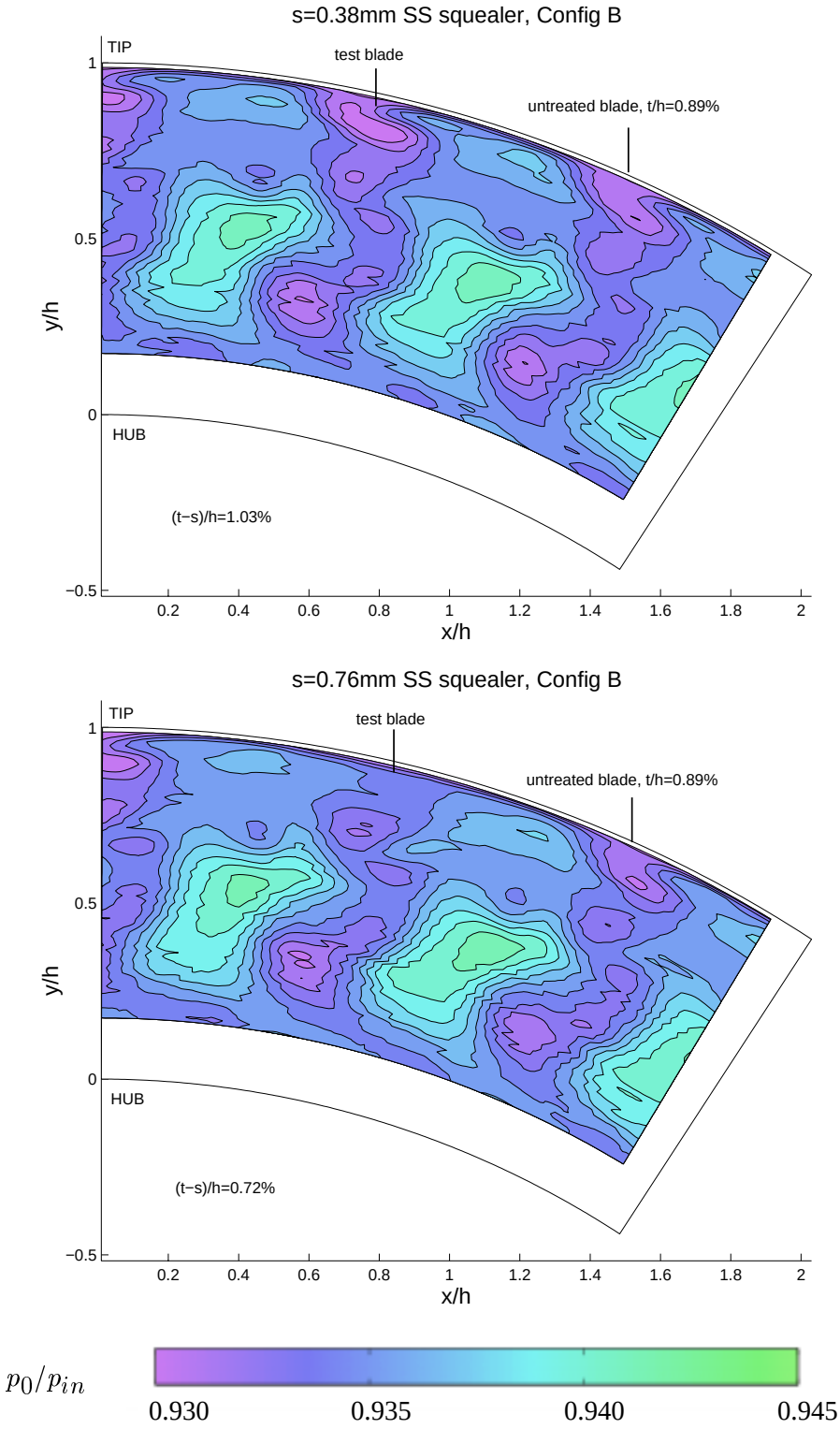

Fig. 4.15. Contours of p_0/p_{in} for SSSq-B, $t/h = 1.03\%$ and 0.72%

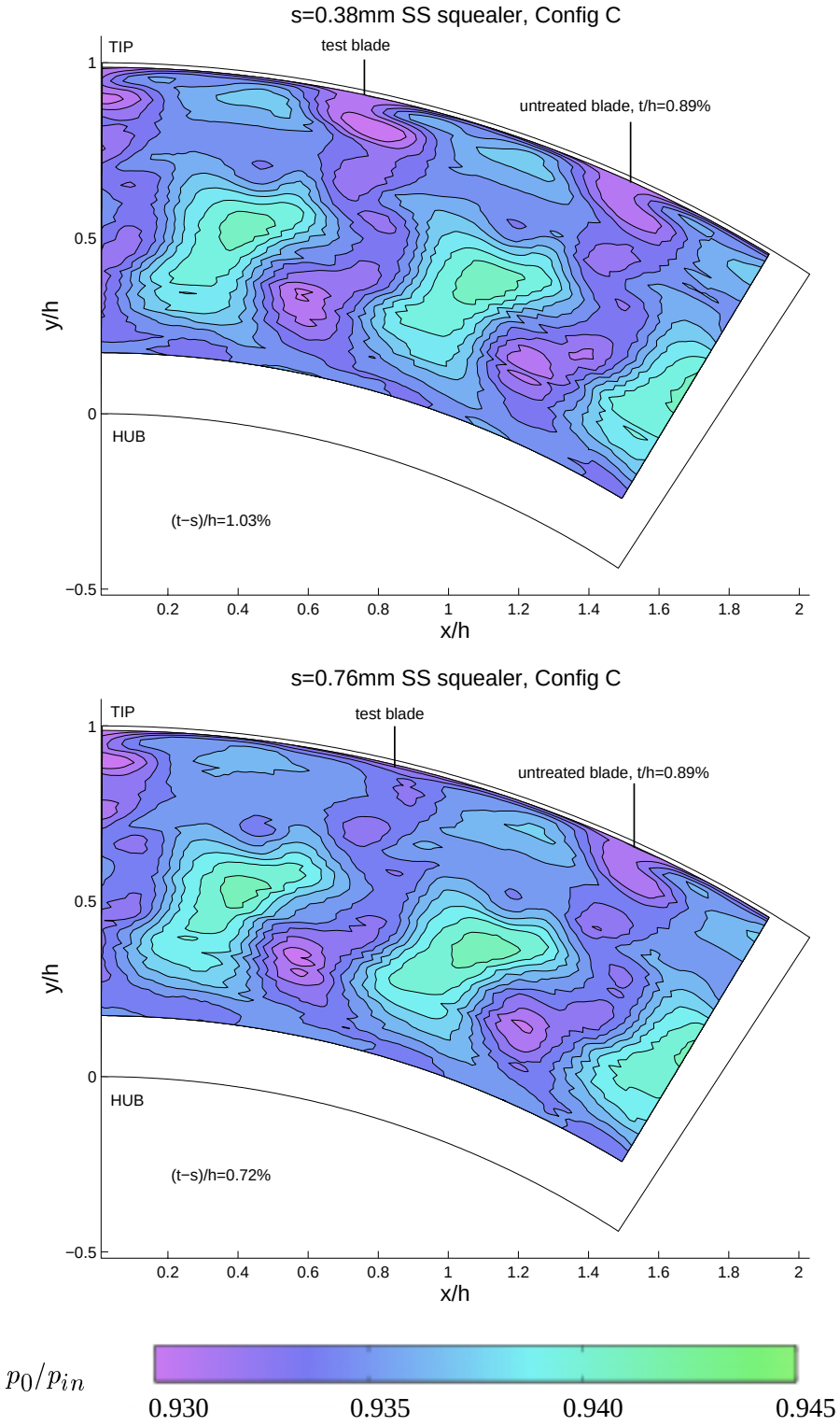

Fig. 4.16. Contours of p_0/p_{in} for SSSq-C, $t/h = 1.03\%$ and 0.72%

this with Figure 3.9, which shows the baseline with a clearance of ($t/h = 0.72\%$), one notices a smaller loss core when the rim is present. This means that the taller rim works ever better than a flat tip surface of the same height.

The same inference could be drawn from Figure 4.17. Here SSSq-B with 0.38 mm rim is compared with a flat (non-desensitized) tip with the same clearance, called "full cover" in the legend. Two plots are presented, at $r/h = 89.7\%$ and $r/h = 79.3\%$. The first one corresponds roughly to the core of the leakage vortex and the second one corresponds to the core of the passage vortex. It is clear that the 0.38 mm SSSq-B performance is identical to the full cover near both the leakage and the passage vortices. Figure 4.17 should be compared to Figure 4.18, which shows the same facts with 0.76 mm SSSq-B. It is clear that the SSSq-B performs significantly better than the flat cover with the same clearance in the leakage vortex zone ($r/h = 92.2\%$). The performance is roughly similar at $r/h = 81.9\%$, which is at the core of the passage vortex. This shows that the SSSq configuration is effective only when the rim is relatively high, hence the 0.76 mm rim performs better than the 0.38 mm rim.

Figure 4.19 makes an attempt to explain why this might be the case. In this figure, a cross section of the rotor blade is shown. The rotor blade is shown stationary, while the casing moves on top of it with a velocity U_{casing}. Flow from the pressure side is seen to enter the clearance gap. At the pressure side corner, a separation bubble $A5$ forms. A little upstream, the flow encounters a forward facing step as it meets the squealer rim of height h_s. A second separation bubble $A4$ forms at this corner. The flow then moves radially upwards as it tries to negotiate the squealer rim. However, right next to the moving wall, a velocity equal to U_{casing} is induced, that points from the suction side towards the pressure side. Some of the radially upward flow might roll up in a vortex $A3$ as it encounters the "backward" flow near the moving

wall. The rest of the radially outward flow does manage to climb on top of the squealer rim and escape to the suction side of the rotor, and there, upon meeting the passage flow, it rolls up into the leakage vortex $A6$. Saddle points $A1$ and $A2$ are also expected to form. Of key importance in this scenario is the formation of the vortex $A3$ which tends to sit on the blade tip surface and form a barrier to the mass flow trying to leak through the clearance gap. The leakage mass that manages to form the leakage vortex at $A6$ is the relatively small fluid mass that escaped below the vortex $A3$. Not only is this mass small, but the momentum associated with it as it escapes to the suction side is small too, hence the leakage vortex at $A6$ is weakened. This is the reason why a squealer tip is more effective than a full cover. In a full cover case, the amount of mass leaking to the suction side is probably very similar to the squealer case, but the leakage flow escapes to the suction side as a high speed jet, and this momentum and energy is dissipated inside the leakage vortex.

One might guess how the squealer rim height h_s changes the scenario. The discussion above is relevant for relatively large values of h_s/τ_{max}, where τ_{max} is the maximum blade thickness. One suspects the vortex $A3$ forms only when h_s/τ_{max} is large. For lower h_s, the leakage mass does not have a significantly large radially outward momentum near the separation bubble $A4$, and the vortex $A3$ may not form. The leakage jet possible goes straight through the tip gap, and emerges as a relatively strong jet on the suction side, leading to the formation of a relatively strong leakage vortex. Thus the flow behaves quite like a flat tip, which is what the results show.

Figure 4.20 compares the three SSSq configurations. Again, the top and the bottom plots correspond to the core of the leakage and the passage vortices respectively. It is obvious that all three configurations perform similarly, and this is also, as shown earlier, the performance

of a flat tip with the same clearance. Figure 4.20 needs to be compared to Figures 4.21 and 4.22, which shows the performance of the three 0.78 mm rim SSSq configurations at four radial locations, $r/h = 94.8\%, 92.2\%, 89.7\%, 79.3\%$. The first three corresponds to approximately the leakage vortex core while the last one corresponds to the passage vortex core. All four plots seem to show that configuration SSSq-B performs better than SSSq-A or SSSq-C. The superior performance is evident near the leakage vortex core, but it is also felt near the passage vortex. This means that the length of the squealer rim is important for the purpose of desensitization. The squealer tip configuration performs better as its length is increased from that of SSSq-A to that of SSSq-B, however, a further increase in length does not perform any better. Thus the rim does not need to extend all the way to the leading edge for best performance.

Figure 4.23 tries to explain why this is so. This figure shows the tip airfoil with the squealer scheme, along with possible flow paths from the pressure side to the suction side. The light blue area marks the part where the SSSq-A is attached. As explained in the previously, part of the mass flow that tries to escape through the clearance gap is blocked by the squealer rim, and all the streamlines originating from region marked **B** gets blocked, for the most part, before it could escape to the suction side. However, it has been shown in various cascade studies ([34]) that streamlines that form the leakage vortex usually originates near region **A**, instead of region **B**. It is also known that most streamlines turn very sharply as they enter the clearance gap, and thus the mass originating near region **A**, that is, near the leading edge of the airfoil leaks through the front part of the airfoil to form the leakage vortex. Any obstruction near the leading edge side of the airfoil would increase the desensitization effects, and as shown by SSSq-B. The streamlines from both region **A** and **B** are blocked by SSSq-B, which is why SSSq-B performs better than SSSq-A. However, SSSq-C does not perform as well as SSSq-B. This is possibly

because in SSSq-C, the rim is erected right in front of the streamlines from region **A** which goes directly to the suction side of the blade without touching the blade tip surface. So some of the blocking effects that the squealer rim could provide is not available to the streamlines from region **A**, and the overall performance is worse than the case of SSSq-B.

4.3.2 Squealer Channel Configurations

Figure 4.24 shows the squealer channel arrangement, the geometry of which was shown in Figure 2.12. Two configurations were tested. Result from SqCh-A, with shorter pressure side squealer rim, is shown in the top sub-plot, while SqCh-B, with the longer pressure side rim, is shown in the bottom sub-plot of Figure 4.24. All the rims were 0.76 mm high. The two figures are almost identical, meaning that the length of the pressure side squealer rim does not seem to affect the desensitization process.

Further light is shed in the flowfield of channel configurations in Figure 4.25. Here three 0.76 mm high squealer configurations are compared, SSSq-B, SqCh-A and SqCh-B. It could be seen that the performance of the SSSq and SqCh configurations are almost identical. Thus the pressure side squealer rims are hardly contributing to the desensitization process. This is an important find, considering most production squealer designs employ a design quite similar to SqCh-B configuration, in the sense that there are rims on both pressure and suction sides. It appears that the pressure side leg of the squealer rim is redundant, and does not block any more mass ejecting from the suction side of the blade. The explanation for this might be found in Figure 4.23. It appears that most of the fluid mass that goes to form the leakage vortex originate in region **X**. The suction side squealer blocks most of this flow, especially in configuration SSSq-B, which seems to provide most of the blockage. Passage flow that originates in region **Y** tend

to move towards the blade wake. Very little fluid from region **Y** cross over to the suction side of the blade and contribute to aerodynamic losses. It appears that the pressure side rim of the SqCh configuration interfere with the fluid from region **Y**. Since fluid from region **Y** plays an insignificant role in the leakage vortex, pressure side rim does not contribute to the desensitization process.

4.4 Desensitization and Efficiency

The stage total to total efficiency of a single stage axial flow turbine is given by

$$\eta_{tt} = \frac{1 - (T_{03}/T_{01})}{1 - (p_{03}/p_{01})^{(\gamma-1)/\gamma}}$$

where subscripts 01 and 03 designate locations upstream of the nozzle and downstream of the rotor respectively. The core flow in the rotor passage that was measured in AFTRF from a stationary frame has a total pressure ratio (p_{03}/p_{01}) of 0.945 and a total temperature ratio (T_{03}/T_{01}) of 0.986. These values could be considered nominal and the corresponding total to total efficiency turns out to be 87.3%, which is about the same as the design value at the midspan of AFTFR. The sensitivity of the stage efficiency to (p_{03}/p_{01}) and (T_{03}/T_{01}) could be examined by differentiating the equation with respect to (p_{03}/p_{01}) and (T_{03}/T_{01}),

$$p_r = \frac{p_{03}}{p_{01}} \qquad T_r = \frac{T_{03}}{T_{01}}$$

$$\delta\eta_{tt} = \left(\frac{\partial\eta}{\partial p_r}\right)_0 \delta p_r + \left(\frac{\partial\eta}{\partial T_r}\right)_0 \delta T_r$$

where the subscript "0" designates nominal conditions. Hence

$$\delta\eta_{tt} = -\frac{[1-(T_{03}/T_{01})][(\gamma-1)/\gamma](p_{03}/p_{01})^{-(1/\gamma)}}{[1-(p_{03}/p_{01})^{(\gamma-1)/\gamma}]^2}\,\delta(p_{03}/p_{01})$$

$$-\frac{1}{1-(p_{03}/p_{01})^{(\gamma-1)/\gamma}}\,\delta(T_{03}/T_{01})$$

and so the variation of the total to total efficiency can be predicted for small changes in (p_{03}/p_{01}) provided that the change in T_{03}/T_{01} is small. Quite obviously, $\delta\eta_{tt}$ depends more strongly on (T_{03}/T_{01}) than on (p_{03}/p_{01}). No temperature measurements downstream of the rotor was performed in any of the experiments reported. Aerodynamic influence of specific tip treatments in the current study are explained solely by measuring the total pressure field at the exit of the stage.

An alternative view of the desensitization process could be described on an enthalpy-entropy diagram. Figure 4.26 explains the aerothermal processes that makes desensitization possible. The rotor entrance flowfield is given by the points 01 and 02 which corresponds to the nozzle entrance and the nozzle exit states. No work is done in the stationary nozzles, hence the path 01 to 02 is roughly a constant enthalpy line. The rotor exit state, 03, is broken into three different constant pressure lines in this diagram. The core flow total pressure is represented by $p_{03,midspan}$ or p_{03MS}, which represents the design rotor exit total pressure of the stage. This corresponds roughly to the maximum value of total pressure shown in the contours plots of this previous chapter. The total pressure near the tip is shown by the line labeled $p_{03,tip}$ or p_{03T}. Obviously, $p_{03MS} > p_{03T}$ holds. When a tip is desensitized, its total pressure "improves", although it never reaches the level of p_{03MS}. This is shown by the line labeled $p_{03,DStip}$,

or p_{03DS}, which corresponds to the average total pressure in the outer endwall area near a desensitized tip. So, $p_{03MS} > p_{03DS} > p_{03T}$ is true for any desensitization scheme. It could be argued that a good desensitization scheme pushes p_{03DS} closer to p_{03MS}. As explained earlier, this by itself does not guarantee higher efficiency, and total temperatures must be taken into account.

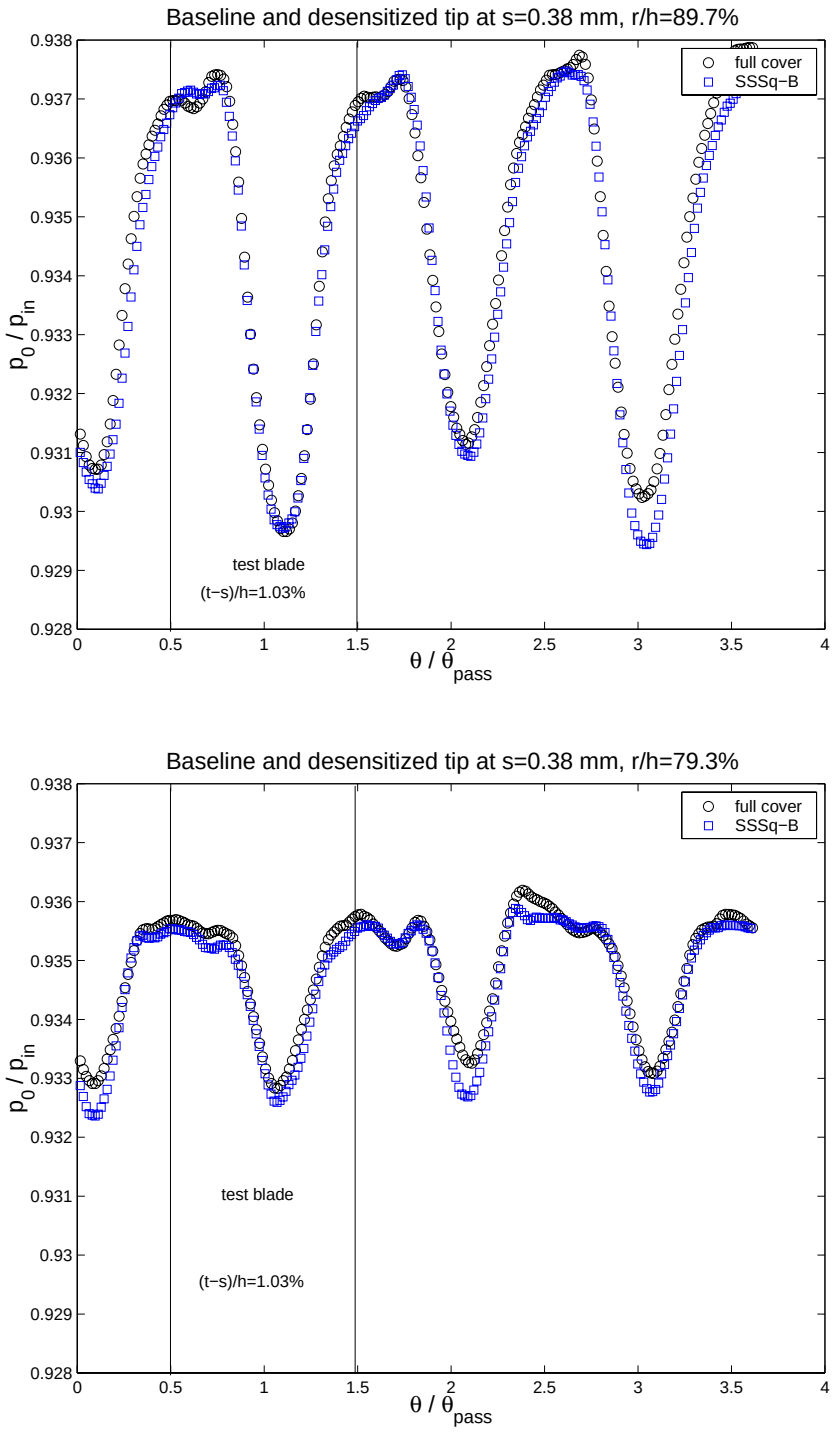

Fig. 4.17. Total pressure deficits due to vortical structures in the blade passage

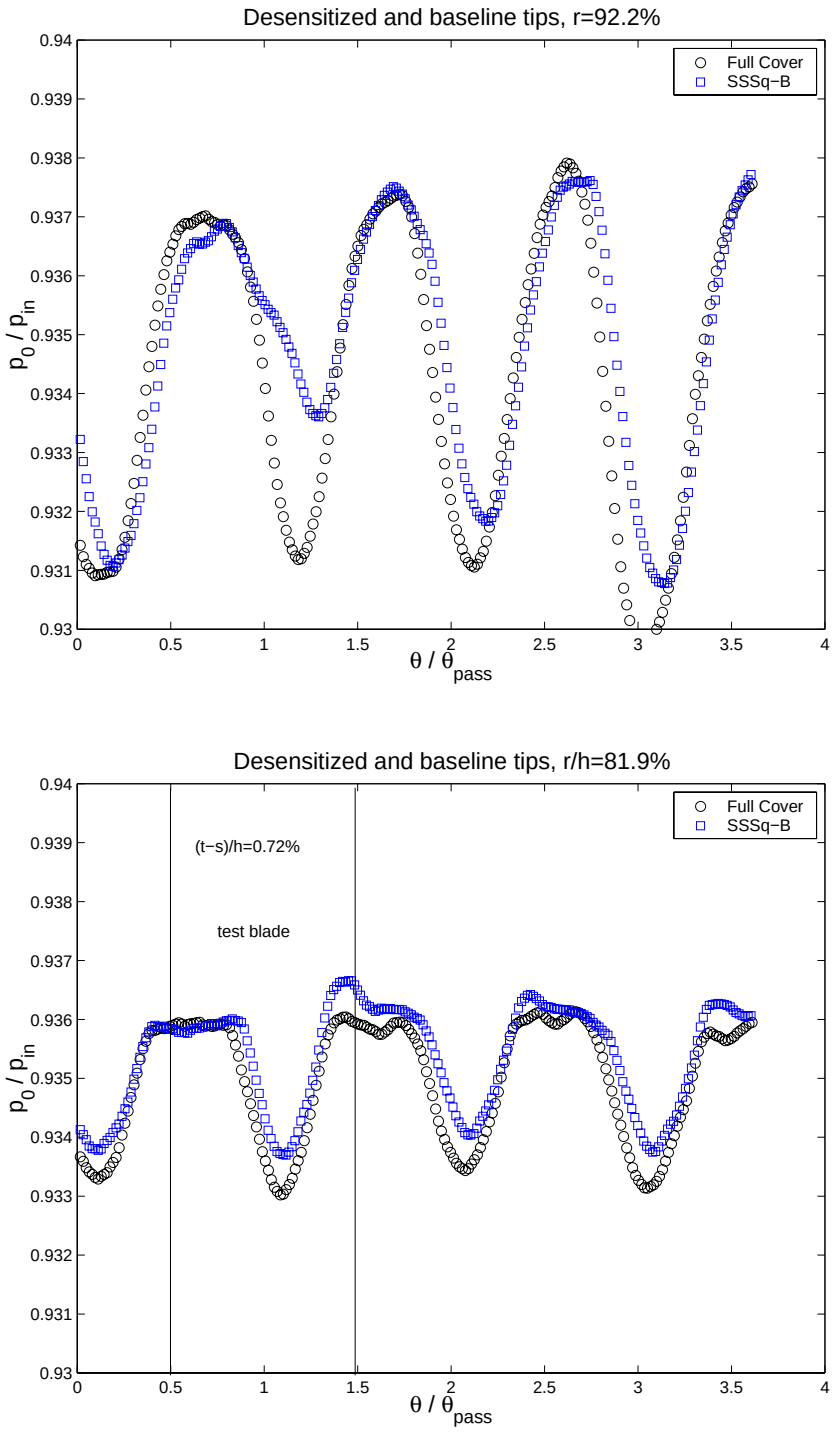

Fig. 4.18. Total pressure deficits due to vortical structures in the blade passage

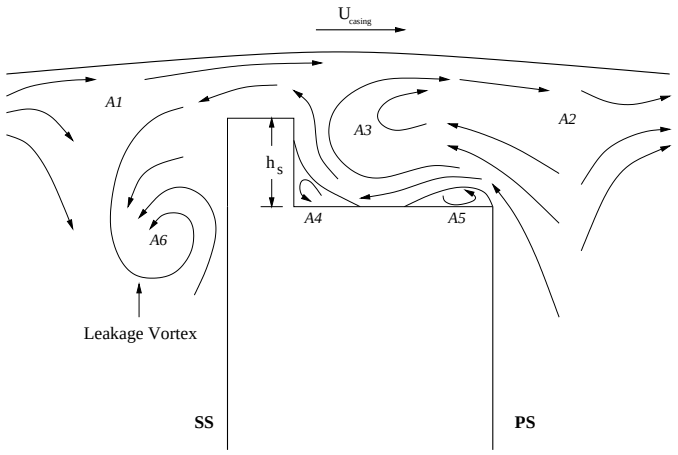

Fig. 4.19. A schematic of possible flowfield near a squealer tip

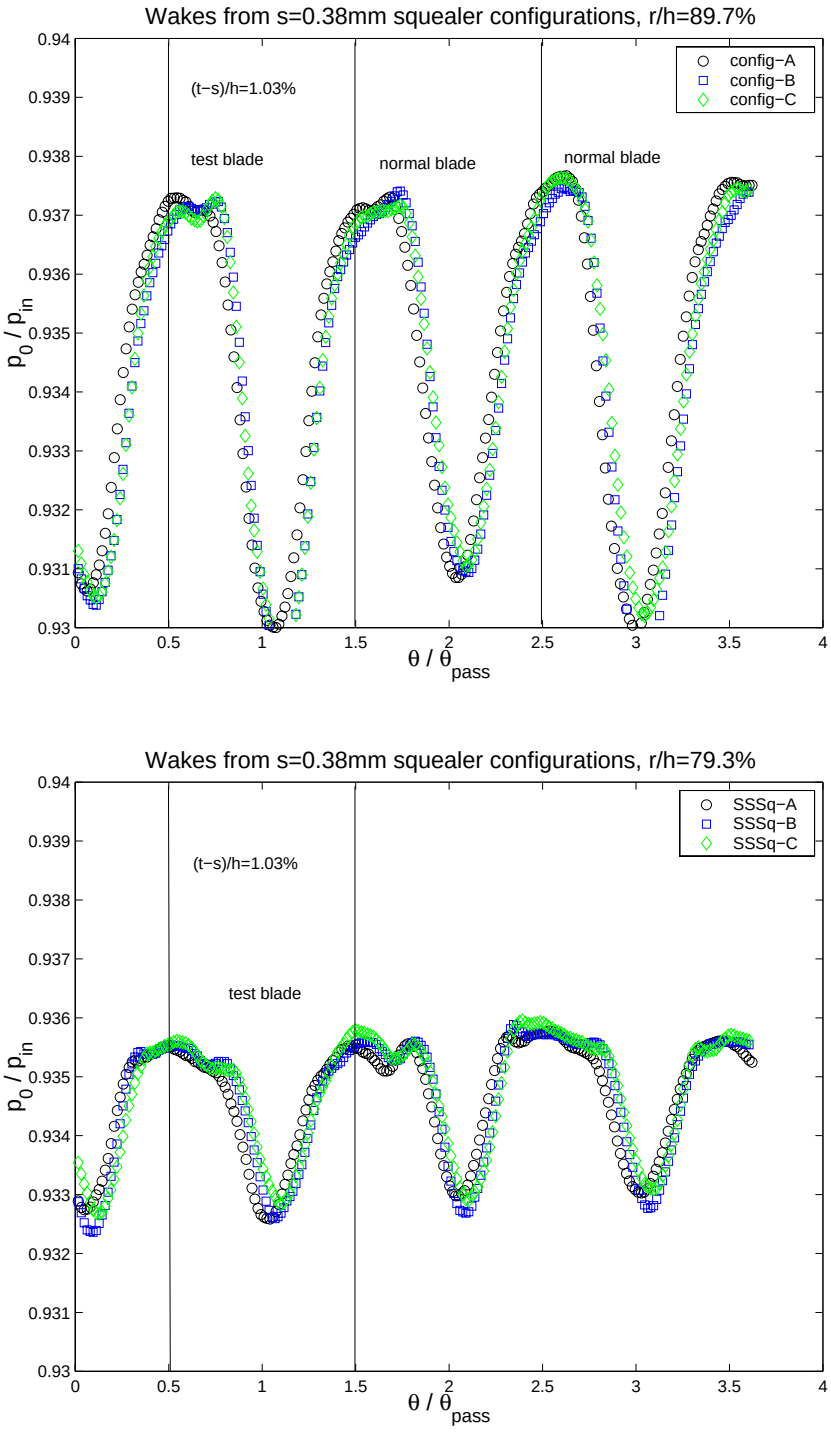

Fig. 4.20. Comparison of three SSSq configurations, $t/h = 1.03\%$

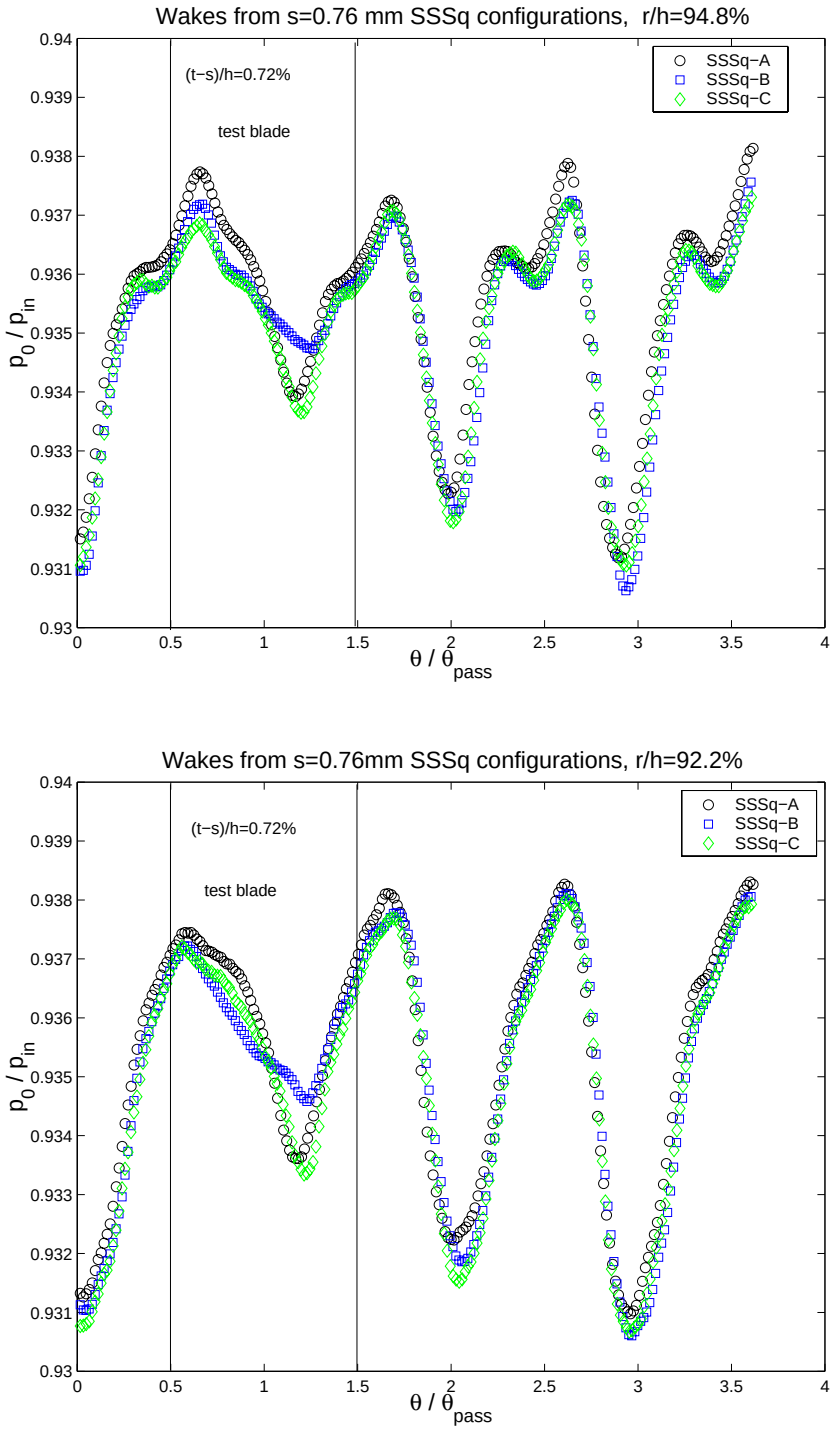

Fig. 4.21. Comparison of three SSSq configurations, $t/h = 0.72\%$

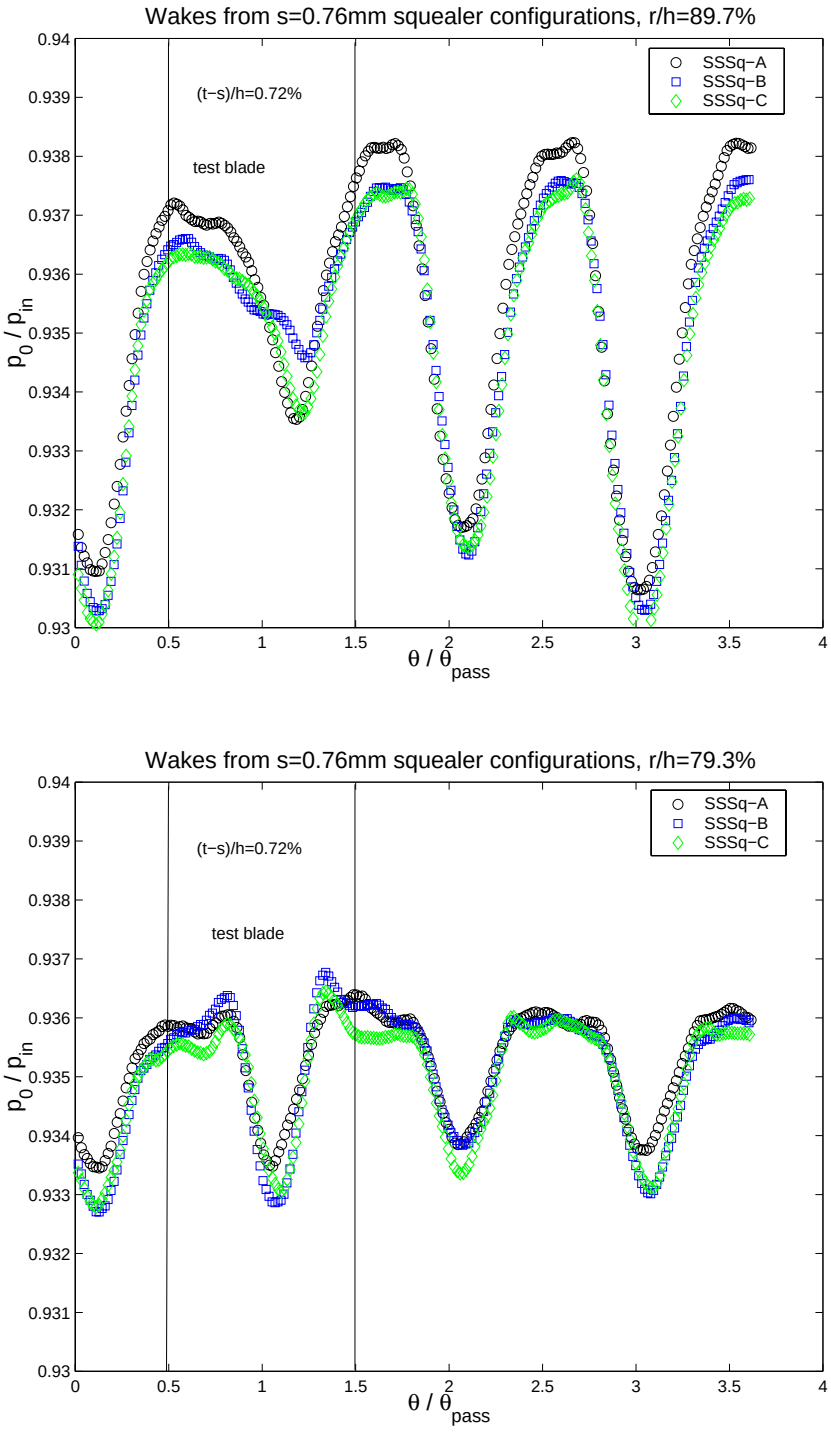

Fig. 4.22. Comparison of three SSSq configurations, $t/h = 0.72\%$

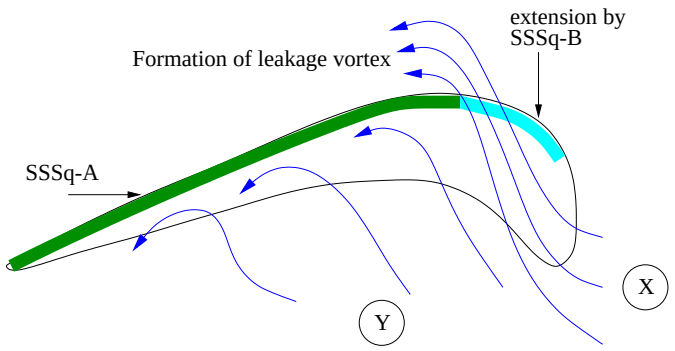

Fig. 4.23. Streamlines near a squealer tip

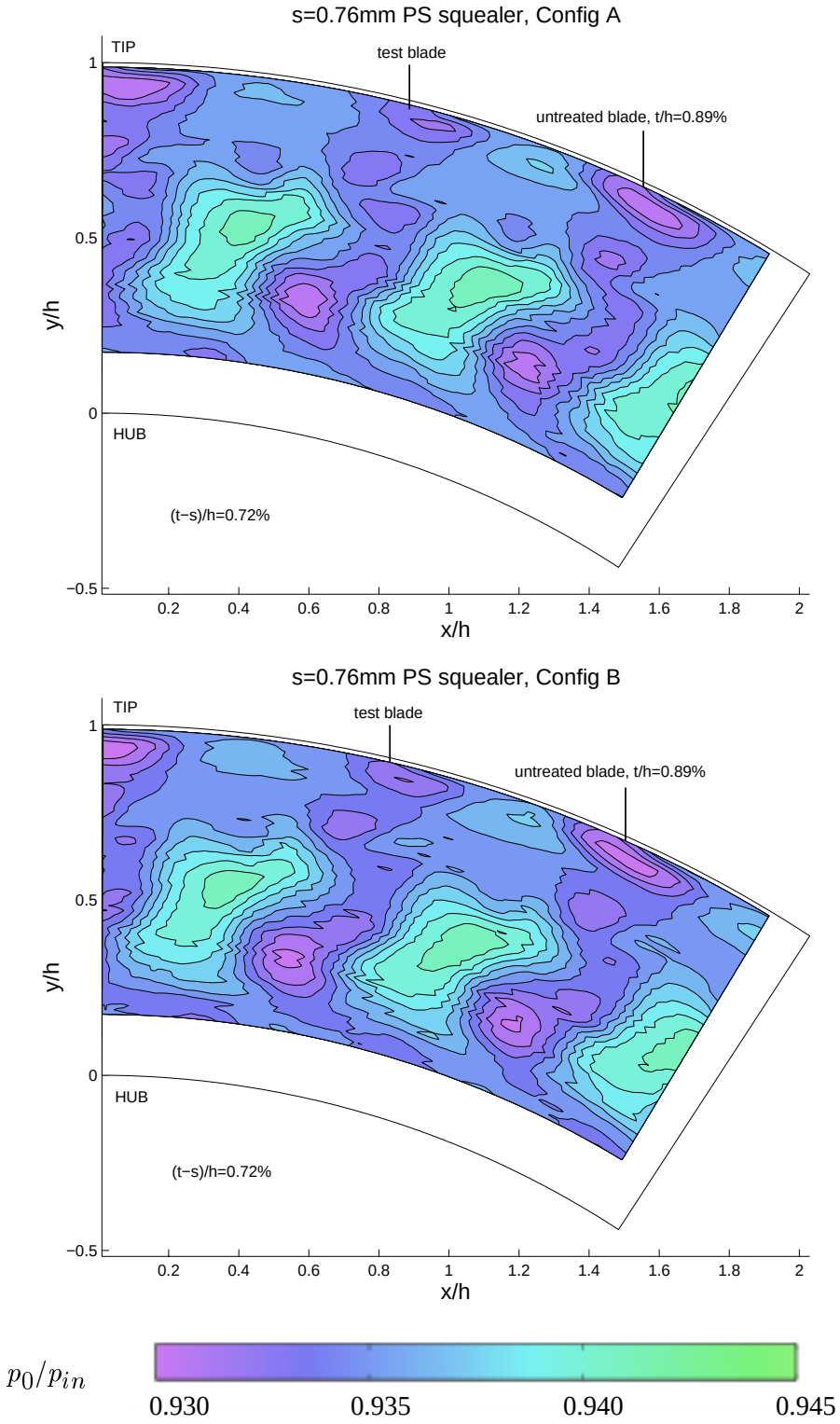

Fig. 4.24. Contours of p_0/p_{in} for SqCh-A and SqCh-B

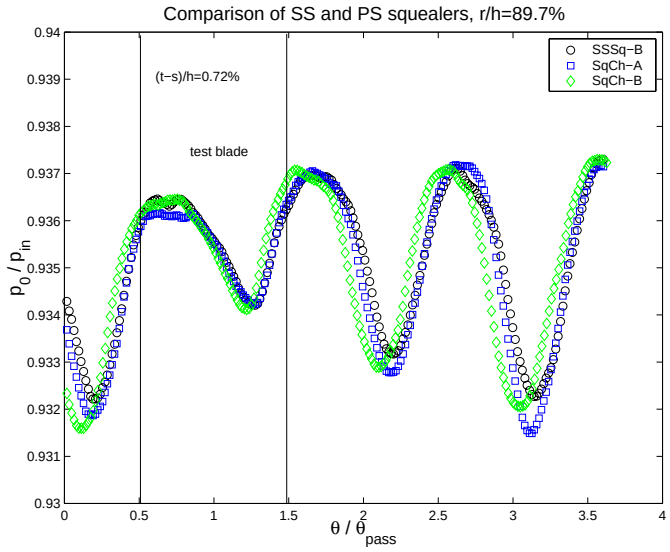

Fig. 4.25. Comparison of the SSSq and SqCh configurations

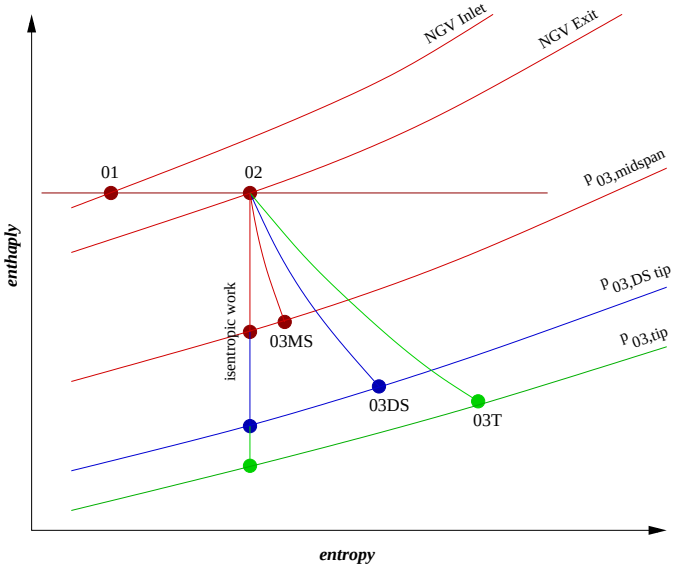

Fig. 4.26. Aerothermodynamics of tip desensitization process

Chapter 5

Conclusions

Tip leakage is an outstanding problem in gas turbines that utilize unshrouded rotors. There are too many problems, and only a few known solutions. Hence tip desensitization is a major area of turbomachinery research, and it is likely to remain so in the near future, since details of the leakage flow are so poorly understood. The present work proposes three desensitization ideas that seem to hold promise:

1. Coolant injection from a tip trench
2. Tip platform extensions
3. Squealer tip

In addition, effect of simply closing the tip gap on the leakage flow is also studied. Lastly, a method of measuring the heat transfer coefficient on the blade tip is demonstrated. The major findings about all these techniques are summarized below.

Gap height variation A series of baseline tips without desensitization are first studied by varying the tip gap height of a selected blade defined as a "test blade". This set of data forms a reference data set for the experiments performed with a desensitized tip. The influence of the tip gap height on the total pressure downstream of the test blade is clearly documented. The results show that the leakage vortex reduces in strength as the gap is closed from $t/h = 1.34\%$ to $t/h = 0.72\%$. The passage vortex also appear to grow weaker with

a weakening leakage vortex. The passage vortex occurs at roughly the same location for all the tip gaps studied. That the leakage vortex is weakened by closing the tip gap has been well established in literature. This set of data clearly shows the total pressure fields from a strong and a weak leakage vortex. This proves to be valuable in evaluating the performance of various desensitization schemes.

Coolant injection Coolant injection is indispensable in high pressure turbine stages. The present study tries to use coolant injection to seal the leakage at the rotor tip by injecting small amount of coolant towards the pressure surface. The idea is to block the way of flow entering the tip gap, thus reducing the leakage mass flow, thereby reducing the adverse effects of the leakage vortex. A mechanism to transfer coolant air from a stationary plenum to a rotating blade is implemented, and an equivalent of 0.3% of the total turbine mass flow is injected from the test blade. Measurements are taken by a five hole probe in a relative frame at two axial locations ($d = 0.38c$ and $d = 0.46c$) downstream of the rotor. Results show that the concept might prove beneficial, but a relatively large amount of coolant is necessary to make significant improvement.

Winglets Tip platform extensions, as scaled down forms of winglets used in aircraft wings, are implemented in one rotor blade defined as a “test blade”. Time accurate total pressure measurements at $d = 0.3c$ are recorded from a stationary probe that has a 150 kHz response time. The data for all 29 blades is averaged over 200 ensembles. The aerodynamic data from the desensitized “test blade” are compared to an untreated baseline case at a similar tip clearance value. Comparisons are also made between the “test blade” and

the “untreated” blade of the neighboring passage from the same experiment. The current experiments show that the suction side extensions are not effective tip desensitization schemes. The suction side tip extension merely pushes the core of leakage vortex further away from the suction side. Although the position of the leakage vortex core is altered, the pressure loss in this configuration is not reduced with respect to the baseline case. The experiments also show that the pressure side extensions tested are highly effective tip desensitization schemes. The entry flow conditions into the tip gap are altered in such a way that the mass flow rate and momentum of the jet leaking into the suction side are reduced.

Squealer tips Squealer tips are made by extending the pressure and the suction surfaces of the rotor blade in a radially outward direction. Thus a thin rim of material encloses a cavity on top of the blade tip surface. The present study investigates the effect of “partial” squealers. Different sized squealer rims are attached to the pressure side and to the suction side of the blade tip surface. Squealer configurations are compared to the baseline configurations with the same clearance height. Results show that the squealers perform better than their equivalent baseline cases only when the clearance is very small. High suction side squealers perform best. The performance of suction side squealers is not improved when a squealer rim is also attached on the pressure side, thereby forming a channel. The suction side squealer is by itself capable of significant aerodynamic tip desensitization. It is also noted that the suction side squealer need not extend all the way up to the leading edge of the blade. Squealers extending to about 4% chord seem to perform best amongst suction side squealers of different lengths. When suction side squealers and winglets with the same clearance are compared, the winglets perform better aerodynamically. It must

be noted that, unlike the squealer, the winglets do not offer protection against accidental rubbing.

Tip heat transfer A method of measuring rotor tip heat transfer is demonstrated. The blade tip, covered by an Inconel heater strip, is sprayed with liquid crystals. The Inconel foil is insulated from the blade material by a thermoplastic shim. On passing electric current through the Inconel, the liquid crystal exhibits narrow isotherms. The motion of the rotor is frozen with a powerful strobe light and images are acquired with a video camera. A filtering technique is developed to combine the still images corresponding to various potentials into a single image, from which the heat transfer coefficient for the blade tip could be obtained.

Appendix

Experimental Uncertainties

A comprehensive assessment of the issues involved in experimental uncertainties is given in [23]. To summarize,

1. There are two kinds of error, bias error and precision error. The bias error is the shift in the measurement average from the true value. The precision error reflects the scatter in the measurement data.

2. Since the true value is not known, bias errors could only be estimated. Precision errors are easily calculated from the data.

3. For the kinds of measurements taken in this project, precision errors are small compared to the bias errors.

4. non-repeatability of data from two or more identical experiments is ascribed to bias error.

Precision errors are mainly estimated from calibrations. Bias errors are estimated from a variety of sources, including manufacturer's quotation, repeatability between experiments and comparisons with a second sensor.

The instruments used in this study are five hole probe and total pressure probe. The uncertainties associated with each of these must be considered. Then there are uncertainties associated with the operation of the rig. Total uncertainties must include all of these.

In what follows, errors are quoted as a percentage of the primary measured quantity. Any error less than 0.1% of the measured value is termed negligible.

Five hole probe

Following are the sources of uncertainty in the five hole probe measurements.

Turbulence effects The five hole probe is used to measure mean pressures in a highly turbulent pressure field. The turbulence is averaged out and the probe measures an increased flow velocity. The five hole probe was calibrated in a jet with 2% turbulent intensity. It was then used downstream of the rotor, where the turbulence intensities from 8% to 18% are seen. The following relation holds between the actual and apparent mean velocities:

$$\bar{v}^2_{FHP} = \bar{v}^2_{actual}\sqrt{1 + 3Tu}$$

Accordingly, the bias error due to turbulence could be between 0.33% to 1.5%.

Reynolds number effects This is a minor effect which becomes predominant at large incidence angles. The separation zone formed at large incidences depend on Reynolds number. If the calibration is done at a Reynolds number significantly different from the test Reynolds number, errors are introduced. For the present study, these errors are negligible.

Mach number effects Errors could be introduced if the test Mach number is different from the calibration Mach number. The probe was calibrated at a Mach number of 0.17 and tested in the rig with maximum Mach number of 0.23. So, Mach numbers are low and of the same order, and the errors are expected to the negligible.

Gradient effects The probe was calibrated in an uniform gradient field and tested in the rig where gradients in pressure and velocity existed. This introduces errors which are proportional to the gradients of total pressure divided by the total pressure. The radial and

circumferential total pressure gradients are significant at some measurement location, but the axial total pressure gradient is negligible. Either way the ratio is negligible.

Wall vicinity effects When a five hole probe approaches a solid wall, local accelerations occur. It is suggested a five hole probe should never be used within two probe diameters from a solid wall. In the present study, the probe was in a rotating frame, and the outer endwall, which was in relative motion to the probe, was the closest solid surface. The probe was never less than 6.5 mm (4 probe diameters) from the wall. So, this effect is negligible.

Probe stem effects and blockage effects This is the effect of the probe stem disturbing the flow field. This effect is usually taken care of during calibration. However, blockage errors are related to the probe area compared to the total area, and is estimated to be 0.2%.

Probe misalignment effects This is the initial misalignment error of the probe in the flow. This human error occurs both in calibration and test. In the current study, the uncertainty in angles is estimated to be 0.5°, which leads to an error of 0.5% in the worst case (for large incidence angles).

Linear interpolation error The five hole probe was calibrated over a pitch and yaw range of $\pm 30^{\circ}$, in intervals of 10°. The calibration was used by a linear interpolation, which is reasonable for data between $\pm 20^{\circ}$, but is prone to error beyond 20°. Errors in pitch and yaw are estimated to be 3.25% beyond $\pm 20^{\circ}$ range. However, the maximum angle that the probe saw during the tests was $\pm 15^{\circ}$, and the error in this range is 1.5%.

Calibration jet error The velocity of the calibration jet is accurate to 0.75%, based on the transducer used to measure the jet velocity.

Data acquisition errors This refers mainly to errors in amplifier drifts and analog-to-digital conversion round-off. The performance of conditioning and acquisition systems are excellent in terms of linearity. Also, the same system is used for calibration and test, to minimize errors even further.

The percentage numbers reported here is associated with the measurement of pressures. Derived quantities like velocities and angles have roughly similar error magnitudes.

Kulite probe

Following are the sources of uncertainty in the unsteady total pressure measurements by Kulite transducer and probe. The transducer was calibrated in the same range of pressures as it was expected to measure in the AFTRF, to minimize nonlinear effects.

Turbulence effects The probe measures unsteady total pressures, which is eventually ensemble averaged. So there are no errors due to turbulence. However, the frequency response of the probe is 150 kHz, and fluctuations above that frequency are not recorded. At the speeds found in AFTRF, there is extremely small amount of signal over 150 kHz, so this effect does not contribute to errors.

Wall vicinity effects The probe was no less than $2d$ away from the outer casing (where d is the probe diameter). So, this error is negligible.

Blockage error This probe was relatively large compared to the five hole probe, leading to blockage error of 0.5%.

Large incidence errors A test was conducted verifying that the probe is sensitive to incidence angle change of $\pm 10^{\circ}$ by 0.1%. The mean exit angle downstream of the rotor in AFTRF

varies by 25° from hub to tip. The variation is well within 20° in the top half of the passage. The probe was aligned with the rotor exit flow near the tip, as the data near the tip was considered most important in these experiments. So the data in the top half of the passage was accurate within 0.1%. It should be remembered that the instantaneous change in exit angle could by much more than $\pm 20^{\circ}$ even in the top half of the passage, and hence the error in instantaneous pressure could by large in principle. It is expected that the ensemble averaging process minimizes these instantaneous errors.

Misalignment errors As mentioned earlier, the probe was aligned to the design rotor exit flow near the tip. The angle was measured to an accuracy of 1°, which leads to negligible error in total pressure.

Temperature compensation errors The Kulite probe is temperature compensated. The compensation bridge is located some distance away from the sensing bridge, and is enclosed in a metallic cylinder. During test runs, the sensing bridge was inside the flow while the compensation bridge was outside in the ambient temperature. The difference in temperature was typically 5 K. This small difference leads to negligible errors.

Operational uncertainties

Following are the sources of uncertainty in the operation of AFTRF.

Temperature variations The ambient temperature varies during the run, which could last anywhere between half an hour to three hours. The AFTRF is inside a building with limited airflow between the interior and the atmosphere, and as the turbine runs, the ambient temperature often rises, especially during the summer months. The ambient temperature could

rise by 10 K during a three hour run. Also, the atmospheric temperature might vary by a few degrees during a long operation. Changes in ambient temperature changes the density of the fluid that enters the rig. Since the turbine is designed to run at corrected mass flow, the RPM is set at the start of the run. The RPM is not intentionally varied during the run (however, see below). This means that the mass flow in the turbine changes during a long run. This means that during a long run, the turbine often operates in slightly off design conditions. It is very hard to quantify this effect, especially since the flow field itself changes during an off-design operation. Hence during a long run that attempts to map the entire rotor exit plane, the part of the data taken during the initial part of the run could be more accurate than the data taken later in time.

RPM variations The RPM of the rig is held constant during the operation by an eddy current brake which is attached to the main shaft with a rubber belt. For reasons that are nor entirely clear, the rig RPM tends to vary during a run. This variation could be ± 2 RPM during a short run or ± 5 during a long run. Changes in RPM alters the mass flow and complicates the scenario described above.

None of these effects could be quantified with any degree of certainty. However, as far as the pressure data is concerned, variations in mass flow could be corrected by measuring the inlet velocity and reducing pressures to pressure coefficients. Of course, that would still not correct the fact that the flowfield itself is changed in off-design conditions.

Finally, it must be remembered that this project involves aerodynamic desensitization, which is characterized by changes from a non-desensitized flowfield. Desensitization performance is evaluated by comparing the modified flowfield to the baseline flowfield. Both the

baseline and modified flowfields are measured using the same techniques, while suffering similar unavoidable errors described in this section. Hence, evaluation of a desensitization strategy is believed to be reliable.

Liquid Crystal Technique for Heat Transfer Measurement

Thermo-chromic liquid crystals respond to a local temperature change by changing color. Thus, liquid crystals could be used to indicate temperatures. Typically, liquid crystals are sprayed over a surface and the temperature distribution on the surface could be obtained from the colors displayed by the crystal. The technique is attractive because it is non-intrusive and it has very good spatial resolution.

Liquid crystals are derived from esters of cholesterol. They have two distinct melting points. At the first melting point the solid crystal turns into cloudy liquid and at the second melting point the cloudy liquid becomes clear. The cloudy phase is a condition between solid phase and the liquid phase. In this phase, the substance acts like a liquid but still retains many of the optical properties of a crystal. The lattice of the crystal gets oriented in various directions depending on the temperature. Hence light of different wavelengths reflect more or less strongly in different directions. This selective light reflection gives rise to different colors depending on the surface temperature.

It is customary to spray liquid crystals on a blackened surface. This reduces reflections from the underlying surface, and ensures maximum brilliance in the colors.

Certain types of liquid crystals (called cholesteric and chiral-nematic) are relatively insensitive to normal and shear stresses. They exhibit all the hues of the visible spectrum as they are heated through their characteristic temperature ranges. This phenomena is reversible and

repeatable. The hues could be calibrated with temperature. The response time could be of the order of milliseconds. The characteristic temperature span characteristic of a particular crystal could be anywhere between 1 K and 50 K. The crystals used in the present study had a bandwidth of 1 K around 315 K (42° C).

The liquid crystal colors are calibrated with respect to temperature. Yellow color provides the narrowest band, while green provides the region with maximum intensity.

A large amount of effort associated with this technique concerns the digital processing of the acquired image. The acquired image is usually stored as red-green-blue data. This data needs to be changed to hue-saturation-intensity data. Usually the green hue is filtered out as it has the highest intensity. This gives an isotherm. The heat transfer coefficient could be related to the isotherm for steady state cases, while in transient experiments the time measured from the start of the experiment is recorded.

A much more detailed account of liquid crystal thermography could be found in [6].

References

[1] A. Ameri and E. Steinthorsson. Analysis of gas turbine rotor blade tip and shroud heat transfer. *ASME Paper 96-GT-189*, 1996.

[2] J. P. Bindon and G. Morphis. The development of axial turbine leakage loss for two profiled tip geometries using linear cascade data. *ASME Paper 90-GT-152*, 1990.

[3] M. Blair. An experimental study of heat transfer in a large-scale turbine rotor passage. *ASME J. Turbomachinery*, 116:1–13, 1994.

[4] T. C. Booth, P. R. Dodge, and H. K. Hepworth. Rotor tip leakage, part-i, basic methodology. *ASME Paper 81-GT-71*, 1981.

[5] D. Butts, J. G. Nourse, and R. C. Simmons. Tip cooled blade. *U. S. Patent 5,261,789*, 1993.

[6] C. Camci. Liquid crystal thermography. *VKI Lecture Series: Temperature Measurements*, 1996.

[7] J. K. K. Chan, M. I. Yaras, and S. A. Sjolander. Interaction between inlet boundary layer, tip leakage and secondary flows in a low speed turbine cascade. *ASME Paper 94-GT-250*, 1994.

[8] J. D. Denton. Loss mechanisms in turbomachines. *ASME J. Turbomachinery*, 115:621–656, 1993.

[9] J. A. H. Graham. Investigation of tip clearance cascade in a water analogy rig. *ASME Paper 1985-IGT-65*, 1985.

[10] R. Graziani, M. Blair, J. Taylor, and R. Mayle. An experimental study of endwall and airfoil surface heat transfer in a large scale turbine blade cascade. *ASME J. for Propulsion and Power*, 102:257–267, 1980.

[11] D. G. Gregory-Smith. Physics of secondary flows. *VKI Lecture Series 1997-01*, 1997.

[12] D. G. Gregory-Smith and J. G. E. Cleak. Secondary flow measurement in a turbine cascade with high inlet turbulence. *ASME J. Turbomachinery*, 114:173–183, 1992.

[13] S. Harrison. Secondary loss generation in a linear cascade of high turning turbine blades. *ASME Paper 89-GT-47*, 1989.

[14] N. W. Harvey and K. Ramsden. A computational study of a novel turbine rotor partial shroud. *ASME Paper 2000-GT-668*, 2000.

[15] F. J. G. Heyes and H. P. Hodson. Measurement and prediction of tip clearance flow in linear turbine cascades. *ASME J. Turbomachinery*, 115:376–382, 1993.

[16] Philip Hill and Carl Peterson. *Mechanics and Thermodynamics of Propulsion, 2nd Edition*. Addison-Wesley, 1992.

[17] B. Lakshminarayana, C. Camci, Ian Halliwell, and M. Zaccaria. Design and development of a turbine research facility to study rotor-stator interaction. *International Journal of Turbo and Jet Engines*, 13:155–172, 1996.

[18] L. S. Langston. Secondary flow in axial turbines - a review. *Presented at ICHMT Turbine Symposium 2000, Cesme, Turkey, 13-18 August*, 2000.

[19] C. P. Lee, H. P. Rieck, N. C. Palmer, and D. G. W. Fargher. Turbine blade squealer tip having air cooling holes contiguous with tip interior wall surface. *U. S. Patent 5,183,385*, 1993.

[20] C. P. Lee, E. T. Vaughn, and N. C. Palmer. Diffusion cooled blade tip cap. *U. S. Patent 4,893,987*, 1990.

[21] R. Mayle and D. Metzger. Heat transfer at the tip of an unshrouded turbine blade. *Proc. of the 7th Int. Heat Transfer Conference, Munich, Vol. 3, pp. 87-92*, 1982.

[22] Andrew A. McCarter. Investigation of tip clearance flow fields in turbine rotor passage. Master's thesis, The Pennsylvania State University, 2000.

[23] C. E. McLean. *The Aerodynamic Effects of Wheelspace Coolant Injection into the Mainstream Flow of a High Pressure Gas Turbine*. PhD thesis, The Pennsylvania State University, 2000.

[24] D. Metzger and R. Bunker. Cavity heat transfer on a transverse grooved wall in a narrow flow channel. *ASME Paper 85-HT-57*, 1985.

[25] D. Metzger and K. Rued. The influence of turbine clearance gap leakage on passage velocity and heat transfer near blade tips: Part i - sink flow effects on blade pressure side. *ASME J. Turbomachinery*, 111:285–292, 1989.

[26] H. Moore and D. G. Gregory-Smith. Transition effects on secondary flows in a turbine cascade. *ASME Paper 96-GT-100*, 1996.

[27] G. Morphis and J. P. Bindon. The effects of relative motion, blade edge radius and gap size on blade tip pressure distribution in an annular cascade with clearance. *ASME 88-GT-256*, 1988.

[28] G. Morphis and J. P. Bindon. The performance of a low speed one and half stage axial turbine with varying rotor tip clearance and tip gap geometry. *ASME Paper 94-GT-481*, 1994.

[29] W. E. North and K. C. McClay. Tip structure for cooled turbine rotor blade. *U. S. Patent 4,424,001*, 1984.

[30] Dimitrije Vojislav Ristic. *Three Dimensional Viscous Flowfield in an Axial Flow Turbine Nozzle Passage*. PhD thesis, The Pennsylvania State University, 1995.

[31] K. Rued and D. Metzger. The influence of turbine clearance gap leakage on passage velocity and heat transfer near blade tips: Part if - source flow effects on blade pressure side. *ASME J. Turbomachinery*, 111:293–300, 1989.

[32] C. H. Sieverding, W. Van Hove, and E. Boletis. Experimental study of the 3d flowfield in an annular turbine nozzle guide vane. *ASME J. Engg. for Gas Turbine and Power*, 106:437–444, 1984.

[33] S. A. Sjolander. Physics of tip-clearance flows, part i. *VKI Lecture Series 1997-01*, 1997.

[34] S. A. Sjolander and K. K. Amrud. Efffects of tip clearance on blade loading in a palner cascade cascade of turbine blades. *ASME J. Turbomachinery*, 109:237–244, 1987.

[35] A. L. Treaster and A. M. Yocum. The calibration and application of five-hole probes. *ISA Transactions*, 18:23–34, 1979.

[36] B. Wiedner. *Passage Flow Structure and its Influence on Endwall Heat Transfer in a Ninety Degree Turning Duct*. PhD thesis, The Pennsylvania State University, 1994.

[37] X. Xiao, A. A. McCarter, and B. Lakshminarayana. Tip clearance effects in a turbine rotor, part i: Pressure field and loss. *ASME Paper 2000-GT-0476*, 2000.

[38] Xinwen Xiao. *Investigation of Tip Clearance Flow Physics in Axial Flow Turbine Rotors*. PhD thesis, The Pennsylvania State University, 2001.

[39] A. Yamamoto. Interaction mechanism between tip leakage vortex flow and passage vortex in a linear turbine rotor cascade. *ASME J. Turbomachinery*, 110:329–338, 1988.

[40] A. Yamamoto. Endwall flow loss mechanismin a linear cascade with blade tip clearance. *ASME J. Turbomachinery*, 111:264–275, 1989.

[41] A. Yamamoto, T. Matsunama, and K. Ikeuchi. Unsteady endwall and tip clearance flows and losses due to turbine rotor stator interaction. *ASME Paper 94-GT-461*, 1994.

[42] A. Yamamoto, J. Tominaga, and T. Matsunama. Detailed measurements of three dimensional flows and losses inside an axial flow turbine rotor. *ASME Paper 94-GT-348*, 1994.

[43] M. I. Yaras and S. A. Sjolander. Development of tip leakage flow downstream of a planar cascade of turbine blades. *ASME J. Turbomachinery*, 112:609–617, 1990.

[44] M. I. Yaras and S. A. Sjolander. Effects of simulated rotation on tip leakage flow in a plane cascade of turbine blades. *ASME J. Turbomachinery*, 114:652–659, 1992.

[45] M. A. Zaccaria. *An Experimental Investigation into the Steady and Unsteady Flowfield in an Axial Flow Turbine*. PhD thesis, The Pennsylvania State University, 1994.

Vita

Debashis Dey was born in Calcutta, India, where he studied till high school. He received his Bachelor of Technology in Aerospace Engineering from Indian Institute of Technology, Kanpur in 1991. Then he received Master of Science in Aerospace Engineering from Indian Institute of Science, Bangalore in 1993. He worked at the Indian Space Research Organization from 1993 till 1996. He began his doctoral studies at The Pennsylvania State University in fall, 1996.

Publications

1. D. Dey and C. Camci, ”Development of Tip Clearance Flow Downstream of a Rotor Blade with Coolant Injection from a Tip Trench”, Proceedings of ISROMAC-2000, 2000

2. D. Dey and C. Camci, ”Aerodynamic Tip Desensitization of an Axial Turbine Rotor Using Tip Platform Extensions”, ASME Paper 2001-GT-484, 2001